To: *Margie*

Joanne and René.

ANGULAR MOMENTUM DISTRIBUTIONS OF FUSION DEDUCED FROM HEAVY-ION REACTIONS

BY

Josephus Johannes Maria Bokhorst

A THESIS SUBMITTED FOR THE DEGREE OF DOCTOR OF PHILISOPHY

AT THE AUSTRALIAN NATIONAL UNIVERSITY

CANBERRA, DECEMBER 1986

PREFACE

This thesis describes an investigation into the shapes of the compound nucleus and related angular momentum distributions by means of heavy-ion reactions.

All experiments were performed at the Department of Nuclear Physics, at The Australian National University, using the 14UD pelletron accelerator.

The project followed from a study of heavy-ion induced fission reactions. The bulk of the experimental work was carried out by Dr. J.R. Leigh, Dr. D.J. Hinde and myself. Professor J.O. Newton, Dr. S. Ogaza and Dr. A. Chatterjee contributed at various stages of the experimental programme.

Existing experimental techniques, used in the detection of evaporation residues and fission fragments were further developed to measure very low cross-sections. The detector used in these measurements was designed by me. The reduction of elastic scattering, fission and most of the evaporation residue data was carried out by myself. The zero-point motion fusion model computer program was written by me and suggested by Dr. J.R. Leigh. The "elastic" fusion model-calculations were carried out with the help of Dr. Y. Kondo and Dr. B.A. Robson. All optical model, fusion and fission cross-section calculations were performed by myself except for the ECIS coupled-channels calculations, which were performed by Dr. J. Nurzynski and fusion/fission calculations for the $^{124}Sn+^{58}Ni$ system, which were performed by Drs. Y. Kondo, B.A. Robson and J.R. Leigh. The gamma-ray multiplicity analysis was performed by professor Newton.

I was helped in the interpretation of the data by many discussions with Dr. J.R. Leigh and professor J.O. Newton.

No part of this thesis has been submitted for a degree at any other University.

J.J.M. Bokhorst

Canberra, December 1986

ACKNOWLEDGEMENTS

I would like to express my sincere gratitude to Professor J.O. Newton and Dr. J.R. Leigh for their expert guidance during the course of this work. Especially I would like to thank Jack Leigh for his continuous support in both work and personal matters. I am grateful to Prof. J.O. Newton, Drs. Jack Leigh and David Hinde for the many discussions and their critical reading of this thesis.

Thanks are also due to Drs. Y. Kondo and B.A. Robson for help on some theoretical aspects of this work and for modifying their optical model program to calculate "elastic" fusion cross-sections and to Dr. J. Nurzinsky for performing some coupled-channels calculations.

I am also indebted to Drs. S. Ogaza and A. Chatterjee for their assistance in the running of the experiments and to Bert Muggleton for preparing the targets, Gerald Clarkson for advice on drawing matters and Gavin Gilmore for his excellent service with photographic work.

Finally I would like to thank Dr. T.R. Ophel for his supervision during the one year study-leave of Prof. J.O. Newton.

ABSTRACT

Experiments have been performed to measure elastic scattering, evaporation residue and fission fragment cross-sections for several projectile-target systems. Also average gamma-ray multiplicities have been measured for the reaction $^{159}Tb+^{19}F$ at various bombarding energies.

Elastic scattering data have been used in optical model analyses to obtain the partial reaction cross-section distributions for the systems : $^{139}La + ^{19}F$; $^{150}Sm + ^{18}O$; $^{159}Tb + ^{19}F$; $^{169}Tm + ^{19}F$ and $^{181}Ta + ^{19}F$ at various bombarding energies.

Evaporation residue cross-sections at energies near and below the fusion-barrier are used in fusion model calculations (zero-point motion model and elastic fusion model) to extract the partial fusion cross-section distributions predicted by these models. These distributions are then compared with the results from the optical model analysis.

The average gamma-ray multiplicities are used to deduce the average angular momentum and the width of the spin distribution for various xn-channels. These are then compared with the results of statistical model calculations using different compound nucleus angular momentum distributions.

Compound nucleus angular momentum distributions, predicted by the zero-point motion and "elastic" fusion models are also used in fission cross-section calculations, the results of which are compared with experimental cross sections. From the comparison between different methods information is obtained about the role of nuclear surface effects and particle transfer reactions in the sub-barrier fusion processes.

The effects of hexadecapole deformation on sub-barrier fusion for some of the tungsten and hafnium isotopes have been investigated. No substantial difference between the isotopes were evident.

CONTENTS

CHAPTER 5 DATA ANALYSIS AND DISCUSSION

CHAPTER 1
INTRODUCTION

When an experimental target is bombarded with a beam of accelerated heavy-ions, some of the beam-particles may come close enough to a target-nucleus to fuse with it. In the fusion process the kinetic energy of the beam-particle is transferred to the fused system, which gets highly excited. The excitation energy, initially localized near the region of impact, is subsequently shared among the other nucleons of the fused system. The fully equilibrated system is called the compound nucleus (CN).

In finite impact-distance collisions, which lead to fusion, apart from the kinetic energy also the total relative angular momentum is transferred to the fused system. If the nuclei are considered to be spheres with sharply defined boundaries, it can be shown with simple geometry that the fusion cross-section increases linearly as a function of angular momentum (L) up to a maximum value L_{max}, which corresponds to the sum of the nuclear radii, and then drops sharply to zero. However, the nuclear boundaries are in general neither spherical nor and sharply defined and further, fusion may proceed via nuclear excitation or particle rearrangement processes. Since these processes are dependent on the detailed structure of the nuclei, the fusion process is very complicated and the compound-nucleus angular-momentum distribution deviates from the sharp cut-off form.

The (CN) angular momentum distribution plays a very important role in the decay of compound nuclei, formed in heavy-ion induced fusion reactions. In particular the competition between fission and particle evaporation is strongly influenced by the angular momentum of the compound system.

Also in the particle evaporation mode of decay the angular momentum affects the neutron multiplicity distribution i.e. the number of emitted x-neutrons. For some of the rare-earth nuclei (e.g. ^{154,156,160}Er [Küh83],[Haa85]) the statistical model of compound nuclear decay underpredicts the cross-sections for the lowest xn-channels by orders of magnitude. This has been ascribed to a super-deformation of the decaying system, which would reduce its temperature and therefore reduce the probability of neutron evaporation.

The observed difference may however, also be explained with a diffuse CN angular momentum distribution, which extends to high L-values. In this case a large fraction of the excitation energy is in the form of rotational energy, which also reduces the temperature of the system. This illustrates the importance of the angular momentum distribution.

Apart from its significance in the description of the compound nuclear decay, the CN angular-momentum distribution is of considerable interest in the study of the fusion

process itself. Over the last decade a number of fusion models have been proposed to explain the sub-barrier fusion cross-section enhancement, observed for many projectile-target combinations. Many of these models reproduce the fusion cross-sections well over a large energy region, but they often predict different partial fusion cross-section distributions.

Experimentally deduced information about the CN angular momentum distribution may therefore provide a means to test theoretical models of CN formation and CN decay.

Presently there are no experimental techniques with which the CN angular momentum distribution can be measured directly. However, a number of methods exist to deduce information about the distribution indirectly by measuring related quantities.

1) Gamma-ray multiplicity measurements. In the decay of a CN by particle evaporation a number of particles are emitted followed by a cascade of gamma-rays. Since most of the CN angular momentum is removed by the gamma-rays a measurement of their average multiplicity and multipolarity provides the angular momentum. The main uncertainty with this method lies in the conversion of multiplicity to angular momentum.

2) Elastic scattering measurements. From optical model analysis of elastic scattering data the reaction cross-section angular momentum distribution may be obtained. The total reaction cross-section consists of the fusion, direct reaction and Coulomb excitation cross-sections. If the fusion cross-section is a large fraction of the total reaction cross-section its partial cross-section distribution may be similar to the reaction cross-section partial distribution.

3) The fusion cross-section at energies near to and below the fusion barrier is sensitive to the nuclear structure of the nuclei. Reproducing measured fusion cross-sections in this energy-region with theoretical models, which involve nuclear structure effects on the fusion cross-section may be used to reveal the CN angular momentum distribution.

In this thesis the results are presented of a study into the shapes of CN and related distributions with the techniques mentioned above. The angular momentum distributions found are used as input for statistical model calculations to investigate the implications different shapes have on the fission cross-sections.

As a different topic, related to the effects of nuclear structure on the sub-barrier fusion cross-section enhancement, the question of whether the fusion cross-section in this energy-region is sensitive to the negative hexadecapole deformation in the tungsten and hafnium isotopes, as suggested in [Rho85], will be addressed.

The outline of this thesis is as follows; Chapter 2 discusses the basis of optical model theory in relation to elastic scattering, fusion models some of which are used in the data-analysis and some aspects of CN decay. Chapter 3 describes the experimental techniques used in the measurements of elastically scattered particles, evaporation

residues, fission fragments and gamma-ray multiplicities. In chapter 4, the quality of the experimental data is discussed and the results of data reduction are shown. In Chapter 5 the data analysis is presented followed by a discussion and conclusions.

THEORY

CHAPTER 2

THEORETICAL BACKGROUND

2.1 COULOMB SCATTERING

The scattering of heavy ion projectiles from a target-nucleus is described by the Coulomb and nuclear potentials. First consider the action of the Coulomb potential only. To first order the Coulomb interaction between two ions with extended charge distributions can be approximated by a point-charge potential :

$$V_C(r) = \frac{Z_p Z_t}{r} e^2 \qquad (2.1.1)$$

where Z_p and Z_t are the ions charge numbers and r is the separation between their centres.

The effective strength of the interaction depends on the relative velocity v between the ions and is given by the Sommerfeld parameter :

$$n = Z_p Z_t \frac{e^2}{\hbar v} \qquad (2.1.2)$$

For large values of n the motion is near classical, which follows from the Ehrenfest Theorem. The impact parameter b of a classical trajectory is related to the centre of mass scattering angle θ by :

$$b = \frac{n}{k} \cot\left(\frac{\theta}{2}\right) \qquad (2.1.3)$$

where k is the relative wave number of motion.

The distance of closest approach (apsidal distance) for a classical orbit is :

$$D = \frac{n}{k}\left(1 + \sin^{-1}\left(\frac{\theta}{2}\right)\right) \qquad (2.1.4)$$

If the boundary for strong interaction is described with the radius in terms of the projectile and target mass numbers A_p and A_t :

$$R = r_0 \left(A_p^{1/3} + A_t^{1/3}\right) \qquad (2.1.5)$$

then the angle θ_c for which the distance of closest approach equals R can be calculated from :

$$R = \frac{n}{k}(1 + \sin^{-1}(\frac{\theta_C}{2})) \qquad (2.1.6)$$

Angle θ_C is usually called the grazing angle. The corresponding impact parameter b_C is :

$$b_C = \frac{n}{k}\cot(\frac{\theta_C}{2})) \qquad (2.1.7)$$

The grazing angular momentum can then be found from the semi-classical relation between impact parameter and angular momentum (L=kb) :

$$L_C = n\cot(\frac{\theta_C}{2})) \qquad (2.1.8)$$

The above relations are only valid for pure Coulomb scattering in the absence of the strong nuclear force. When in a collision the projectile reaches the strong interaction radius, the trajectory may no longer be described classically as quantum effects (e.g. diffraction and interference) come in to play. Furthermore the action of the nuclear potential may change the identity of the projectile by nuclear excitation or nucleon transfer or even absorb the projectile completely (fusion). To deal with these processes one has to describe the heavy-ion collision quantum mechanically. Nevertheless the classical properties introduced, are useful to understand the global aspects of the scattering process.

2.2 QUANTUM MECHANICAL TREATMENT OF SCATTERING

Consider the scattering of spin zero particles from a short-range potential V(r) ($r\to\infty$;$rV(r)\to 0$). To describe the particle wave function at every stage of the scattering process is a very complicated problem. For calculating the scattering cross-section, which is measured at a large distance from the scattering centre (at the detector position) however, only the asymptotic form of the stationary scattering wave $\Psi(r)$ is needed. The asymptotic form of the wave function $\Psi(r)$ consists of a plane wave in the direction of the beam-particles and a radial wave representing the scattered particles :

$$\Psi_{out}(r) \to e^{ik.r} + f(\theta)\frac{e^{ikr}}{r} \qquad (2.2.1)$$

wave number k=p/ħ where p is the particle momentum vector and h the reduced Planck

constant. The angular dependent function $f(\theta)$ is called the scattering amplitude. The differential cross-section defined as the ratio of scattered flux to incident flux may be calculated from the current density vector :

$$J(r) = \frac{\hbar}{2im}\left[\Psi^*(r)\nabla\Psi(r) - \Psi(r)\nabla\Psi^*(r)\right] \qquad (2.2.2)$$

One obtains for the scattering cross section :

$$\frac{d\sigma}{d\Omega}(\theta) = \left|f(\theta)\right|^2 \qquad (2.2.3)$$

The scattering amplitude $f(\theta)$ may be written in terms of partial waves, which leads to :

$$f(\theta) = \frac{i}{2k}\sum_{L=0}^{\infty}(2L+1)(1-S_L)\,P_L(\cos\theta) \qquad (2.2.4)$$

where $P_L(\cos\theta)$ are Legendre polynomals.

All information on the interaction is contained in the complex quantities S_L, which are asymptotic amplitude ratios of outgoing and ingoing partial waves with angular momentum L. They are often referred to as the elastic scattering or S-matrix and can be written as :

$$S_L = \eta_L \exp(2i\delta_L) \qquad (2.2.5)$$

where δ_L are the nuclear phase shifts and η_L are the attenuation factors, which account for absorption from the elastic scattering channel. Because of the long range of the Coulomb potential, which does not have the property $rV(r)\rightarrow 0$ for $r\rightarrow\infty$, the same derivation leading to (2.2.4) cannot be made for Coulomb scattering. However, a modified mathematical argument [Mot49] results in the same functional form as (2.2.4) for potentials with a r^{-1} dependence. The scattering function describing nuclear as well as Coulomb scattering may then be written as :

$$f(\theta) = f_C(\theta) + f_N(\theta) \qquad (2.2.6)$$

The differential scattering cross-section :

$$\frac{d\sigma}{d\Omega}(\theta) = \left| f_C(\theta) + f_N(\theta) \right|^2 \qquad (2.2.7)$$

therefore accounts for interference between waves from nuclear and Coulomb scattering. The explicit form of $f_C(\theta)$ is given in [Mes70]. It results in a Coulomb scattering cross-section :

$$\frac{d\sigma_C}{d\Omega}(\theta) = \left| f_C(\theta) \right|^2 = \left(\frac{n}{2k} \right)^2 \sin^{-4}(\theta/2) \qquad (2.2.8)$$

which is identical to the classical Rutherford scattering formula. The sum of all non-elastic scattering cross-sections is given by the total reaction cross-section, which may be calculated from the ratio of absorbed to incident flux. The total angle integrated reaction cross-section is given by :

$$\sigma_{React} = \frac{\pi}{k^2} \sum_{L=0}^{\infty} (2L+1)(1 - |S_L|^2) \qquad (2.2.9)$$

Experimental elastic scattering data may be analysed using expressions (2.2.4) and (2.2.7) if a suitable parametrisation for the scattering matrix S_L can be found. For a number of systems this has been done succesfully with Fermi-function parametrisations of η_L and δ_L [McI60] [Spr65],[Fra63]. A more general treatment of quantum mechanical scattering involves solving the Schroedinger equation and will be discussed in the next section.

2.3 THE OPTICAL MODEL AND CHANNEL COUPLING

Consider the scattering of nucleus a from nucleus A, which are both complex nuclei. The stationary wave-function Ψ describing the scattering system may be obtained by solving the time independent Schroedinger equation written in abbreviated form as :

$$H\Psi = E\Psi \qquad (2.3.1)$$

where E is the total energy of the system. It is convenient to separate the Schrodinger equation into parts, which describe the internal motions and the relative motions of the nuclei. The total Hamiltonian may then be written as :

$$H = H_a + H_A - \frac{\hbar^2}{2\mu_\alpha}\nabla^2 + V_\alpha \qquad (2.3.2)$$

where H_a and H_A are the Hamiltonians of the nuclei a and A respectively. They are the sum of potential and kinetic energies of the nucleons in the respective rest-frames. The ∇^2 operator in the kinetic energy term of relative motion acts on the distance r_α between the centres of a and A. The interaction potential between the nuclei is denoted by V_α. Both nuclei are described by the internal wave functions Ψ_a and Ψ_A, which are solutions of the Schroedinger equations :

$$H_a\Psi_a = E_a\Psi_a \;\; ; \;\; H_A\Psi_A = E_A\Psi_A \qquad (2.3.3)$$

with eigen-energies E_a and E_A.

Because the wave functions Ψ_a, Ψ_A describing the various internal states of the two nuclei form complete sets, the total wave function Ψ may be written in terms of them :

$$\Psi = \sum_{a'A'} \chi_{a'A'}(r_\alpha)\,\Psi_{a'}\Psi_{A'} \qquad (2.3.4)$$

If this expansion together with (2.3.2) are substituted into (2.3.1) one obtains :

$$\sum_{a'A'}\left[\nabla^2 - U_\alpha + k^2_{a'A'}\right]\chi_{a'A'}(r_\alpha)\,\Psi_{a'}\Psi_{A'} = 0 \qquad (2.3.5)$$

$$\text{with } U_\alpha = \frac{2\mu_\alpha}{\hbar^2}V_\alpha \quad \text{and} \quad k^2_{a'A'} = \frac{2\mu}{\hbar^2}\left\{E - E_{a'} - E_{A'}\right\}$$

Multiplying (2.3.5) from the left with $\Psi_a^*\Psi_A^*$ and integrating over all internal coordinates τ_a, τ_A of the two nuclei leads to :

$$\left[\nabla^2 - \langle aA\,|U_\alpha|\,aA\rangle + k^2_{aA}\right]\chi_{aA}(r_\alpha) = \sum_{a'\neq a;A'\neq A}\chi_{a'A'}(r_\alpha)\,\langle aA\,|U_\alpha|\,a'A'\rangle \qquad (2.3.6)$$

where :

$$\langle aA \mid U_\alpha \mid a'A' \rangle = \int\int \Psi_a^*(\tau_\alpha)\, \Psi_A^*(\tau_A)\, U_\alpha\, \Psi_{a'}(\tau_a) \Psi_{A'}(\tau_A)\, d\tau_a d\tau_A \qquad (2.3.7)$$

are matrix elements, which are still functions of r_α.

Each pair of states a'A', which are basis states of Ψ, are referred to as a channel. If aA is identified with the groundstates of both nuclei, then the wave function $\chi_{aA}(r_\alpha)$ describes scattering in the elastic channel. The elastic channel is coupled to the inelastic channels via the off-diagonal matrix elements on the right-hand side of equation (2.3.6). When solving this set of equations a similar boundary condition as in (2.2.1) has to be imposed to obtain the wave function describing the scattered particles at large distance from the scattering centre. In principle, if all matrix elements are known, the complete scattering problem can be solved. However, there are an infinite number of matrix elements. In practice the infinite set of equations has to be truncated to a relatively few channels, which are known from experiment or theory to couple strongly.

If in the simplest approach all inelastic processes are ignored, the right-hand side of equation (2.3.6) becomes zero and the remainder is the Schroedinger equation, describing elastic scattering with a single potential. This potential is known as the optical model potential and represents the complicated many body interaction between the complex nuclei. The loss of flux from the elastic channel to all other inelastic channels is accounted for by the introduction of an imaginary potential. The use of a complex (real plus imaginary) potential in the optical model of particle scattering is analogous to the introduction of a complex index of refraction for the propagation of light through an absorbing medium. In the following we will refer to this model as the standard optical model. When coupling to other channels is taken into account, it is called the coupled channels method. Also in coupled channels calculations an optical potential has to be used to account for the channels, which are not described explicitly.

To evaluate the coupling potentials (2.3.7), the eigen functions of (2.3.3) and the interaction potential U_α are needed. Normally one uses rotational model (deformed nuclei) or vibrational model (spherical nuclei) eigenstates for the nuclear wavefunctions. Transition formfactors are also obtained from these models. (e.g. the rotational model transition formfactors are given by $\beta_\lambda{}^N R_N\, dV_N/dr$, $\beta_\lambda{}^C R_C\, dV_C/dr$ for nuclear and Coulomb excitation respectively. So far a channel has been identified with the particular states of excitation a'A' of the nuclei. These states can be further specified by their spins J_a,J_A. The vector sum of these spins $S_a = J_a + J_A$ is called the channel-spin. If furthermore the wavefunctions are expanded into partial waves, a partial channel can be

defined, and identified by the set of quantum numbers $\alpha = \{a,A,J_a,J_A,L_\alpha,S_\alpha,J\}$, where L_α is the relative orbital angular momentum of the nuclei and J the total spin given by : $J = L_\alpha + S_\alpha$.

A complete description of the coupled equations in terms of all quantum numbers can be found in [Aus69],[Sat83],[Rho80]. The standard procedure in solving the say N coupled equations is to find N independent solutions to the N coupled equations and then construct a linear combination which has the asymptotic form :

$$\Psi(r)_{r\to\infty} = \sum_\alpha C_\alpha \left[I_\alpha - \sum_\beta S_{\beta\alpha} O_\alpha \right] \qquad (2.3.8)$$

where I_α and O_α are the incoming and outgoing waves and $S_{\beta\alpha}$ is the scattering matrix. C_α is a normalisation constant. In this process the partial scattering matrix $S_{\beta\alpha}$ is found.

In the derivation leading to equations (2.3.6) and (2.3.7) the orthogonality of the initial and final eigenstates were used. This is correct for the description of nuclear excitation, but not for rearrangements collisions (particle transfer). In general the description of particle transfer leads to integro-differential equations [Aus69],[Sat83]. The coupled-channels calculations which were performed for the system $^{150}Sm+^{18}O$ (discussed in chapter 5) considered coupling to nuclear excitation channels only.

2.4 FUSION

In this section the theory of heavy ion fusion reactions will be discussed. The fusion of two heavy ions is a very complicated process. In the simplest approach fusion is determined by reaction dynamics only. The nuclei are then considered to be rigid spheres and fusion is described in terms of the kinetic energy, the impact parameter and the interaction potential of the colliding system. The next step is to allow for more realistic nuclear shapes and to take the nuclear structure of the participating nuclei into account. As in general both nuclei consist of many nucleons, this is a very complex problem. Especially, because there is an interplay between the dynamics of the collision and the nuclear structure of the colliding species.

When two composite nuclei approach each other, their interaction potential will change the motion of the individual nucleons inside the nuclei. This may lead to

collective motion of the nucleons, which results in nuclear rotation or nuclear vibration. When the nuclei are close enough this may also lead to transfer of nucleons from one nucleus to the other. As a result, part of the total kinetic energy is transformed into excitation energy and part of the relative angular momentum is transformed into intrinsic spins of the nuclei. This will affect the relative motion of the nuclei thus also the fusion probability. In the following, various fusion models, from the rigid sphere approach to models incorporating nuclear structure effects, will be discussed.

2.4.1 Classical fusion model

The potential representing the interaction between two nuclei with charge numbers Z_1 and Z_2 at distance r from each other may be written as :

$$V(r) = -V_N(r) + \frac{Z_1 Z_2}{r} e^2 + \frac{L(L+1)\hbar^2}{2\mu r^2} \qquad (2.4.1)$$

where $V_N(r)$ is the nuclear potential, μ is the reduced mass and L is the relative angular momentum of the colliding system.

In figure 2.1 typical interaction potentials are shown as a function of separation r for several values of L. A projectile approaching from large distance at first experiences a repulsive potential, which increases to a maximum at $r=R_{max}$. If the projectile is energetic enough to overcome the potential barrier, it will experience an attractive force, due to the negative nuclear potential. In this domain strong frictional forces reduce the projectile`s kinetic energy, generally to such an extent that the particle gets trapped in the "pocket" of the interaction potential. The simplest criterion for fusion is to require that the centre of mass energy E_{cm} is higher than the top of the potential barrier (fusion barrier). Any projectile crossing the fusion barrier is assumed to fuse with the target-nucleus. Figure 2.1 shows that for a given E_{cm}, fusion will take place in collisions with relative angular momenta L up to a maximum value L_m.

For $L=L_m$:

$$E_{CM} = V_b + \frac{L_m(L_m+1)\hbar^2}{2\mu R_m^2} \qquad (2.4.2)$$

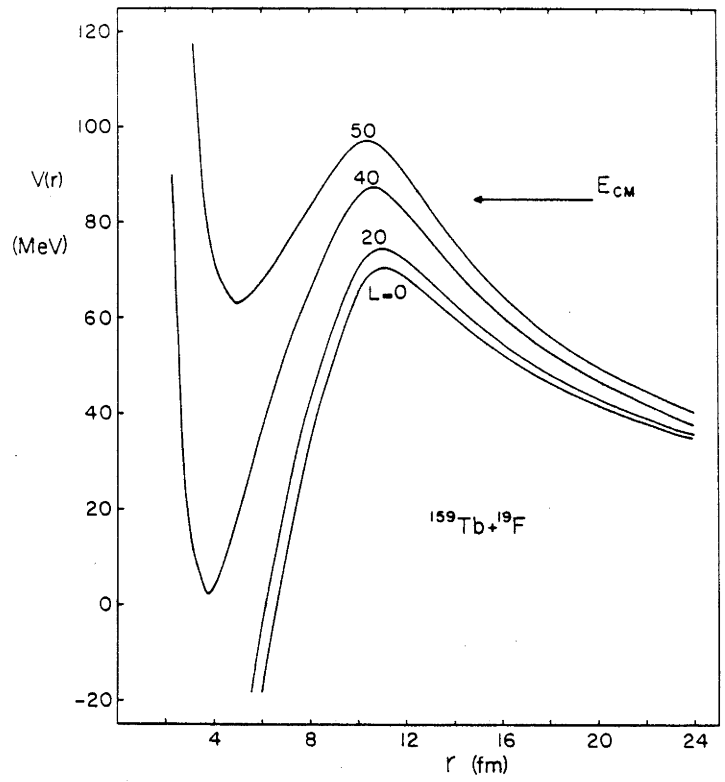

Fig. 2.1 Potential barriers in nuclear collisions with different relative angular momenta.

$$\text{with} \qquad V_b = -V_N(R_m) + \frac{Z_1 Z_2}{R_m} e^2 \tag{2.4.3}$$

Similar to (2.2.9) we may write for the fusion cross-section :

$$\sigma_{fus} = \pi \lambda\!\!\!^{-2} \sum_{L=0}^{\infty} (2L+1)\, T_L \tag{2.4.4}$$

where the transmission coefficient T_L for this simple fusion model is given by :

$$T_L = \begin{cases} 1 & \text{for} \quad L < L_m \\ 0 & \text{for} \quad L \geq L_m \end{cases} \tag{2.4.5}$$

The asymptotic de Broglie wavelength of the projectile is given by : $\lambda\!\!\!^{-} = \hbar/(2\mu E)^{1/2}$.

The summation in (2.4.4) runs from L=0 to L=L_m, thus it is equal to $(L_m+1)^2$. If L_m obtained from (2.4.2) is substituted into (2.4.4) the fusion cross-section can be written as :

$$\sigma_{fus} = \pi R_m^2 \left(1 - \frac{V_b}{E_{CM}} \right) \qquad (2.4.6)$$

This model predicts a linear relationship between σ_{fus} and $1/E_{cm}$, which is correct for energies well above the fusion barrier as demonstrated in fig. 2.2. However, it also predicts $\sigma_{fus}=0$ for $E_{cm}=V_b$, whereas experimentally determined sub-barrier fusion cross-sections are finite. This model is clearly inadequate at energies near and below the fusion barrier. A natural improvement to the sharp cut-off criterion in (2.4.5) is to calculate the transmission coefficients quantum mechanically. This can be achieved with the W.K.B. approximation of quantum mechanical tunneling.

If one assumes a parabolic shape for the potential barrier, the transmission coefficient can be written as :

$$T_L = \frac{1}{1 + \exp\left\{ 2\pi(V_b - E_{CM})/\hbar\omega_L \right\}} \qquad (2.4.7)$$

with :

$$\omega_L = \frac{1}{\mu} \frac{\partial^2 V(r,L)}{\partial r^2} \qquad (2.4.8)$$

This procedure is known as the Hill-Wheeler [Hil53] parabolic barrier approximation. Even with these more refined calculations it is not possible to account for the experimentally observed enhancement in the sub-barrier fusion cross-section. The main short-coming of this model lies in the assumption that the nuclei may be represented by rigid spheres. Most nuclei are deformed and the spherical nuclei are not rigid. Different orientations (or rotation) of a deformed nucleus and the surface vibrations of a spherical nucleus give rise to variations in the fusion barrier. Especially at lower bombarding energies, near the barrier, the fusion probability is very sesitive to these variations. A number of fusion models have been developed, which incorporate these effects. Either by including nuclear surface effects in a barrier penetration calculation, as described above, or in a more general approach by describing the strongest direct reaction channels in a coupled channels calculation.

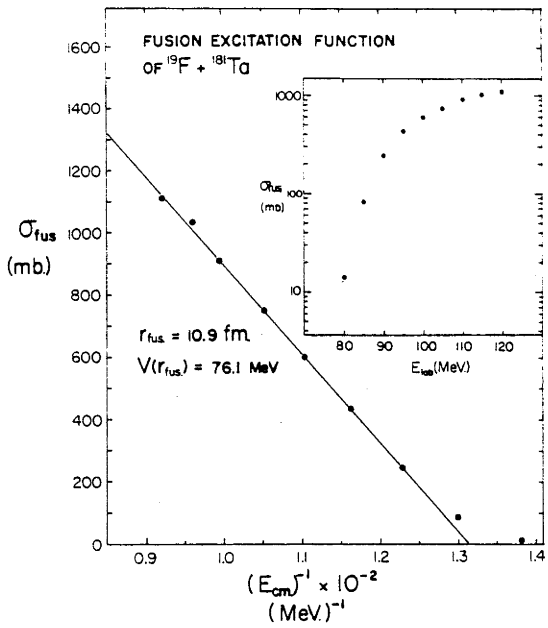

Fig. 2.2 Fusion cross sections versus $1/E_{CM}$ for the reaction $^{19}F+^{181}Ta$. From [Hin82].

If most of the direct reaction cross-section is accounted for, then what remains is the fusion cross-section. In the following sections some of these models will be discussed.

2.4.2 ZERO-POINT MOTION MODEL

The effect of nuclear surface vibrations on the fusion cross-section is described in the zero point motion (Z.P.M.) model of Esbensen [Esb81]. If the vibrational period is much longer than the characteristic time for the fusion process to take place, the nuclear shape may be considered unchanged during the fusion process. The fusion probability may therefore be calculated from a static potential. Although constant during the fusion process, the interaction potential is different from collision to collision. To derive the distribution of nuclear shapes the Z.P.M. model makes use of the collective model of nuclear vibrations [Boh75].

In the collective model of surface vibrations the nuclear radius is written as :

$$R(\theta,\Phi) = R_0\left[1 + \sum_{n\lambda\mu} \alpha_{n\lambda\mu} Y^*_{\lambda\mu}(\theta,\Phi)\right] \qquad (2.4.9)$$

where $\alpha_{n\lambda\mu}$ are the vibrational amplitudes. The indices $n\lambda\mu$ are the principal quantum number, the multipolarity of the vibration and the magnetic quantum number respectively.

The term in (2.4.9) with $\lambda=0$ represents a compression (or dilatation) without change of shape and the terms with $\lambda=1$ are associated with a displacement of the nucleus as a whole. The surface vibrations of lowest multipolarity are therefore the quadrupole modes, with $\lambda=2$. If the surface vibrations are assumed to be independent and harmonic, the nuclear wave function is the harmonic oscillator wave function . The distribution of the nuclear radius in the collective ground state may then be calculated from :

$$g(R) = \langle 0 \,|\, \delta\left(R\text{-}R_0 \left\{ 1+ \sum_{n\lambda\mu} \alpha_{n\lambda\mu} Y^*_{\lambda\mu}(\theta,\Phi) \right\} \right) |\, 0\rangle \qquad (2.4.10)$$

$$g(R) = \sqrt{\frac{1}{2\pi\sigma^2}} \exp - \left\{ \frac{(R-R_0)^2}{2\sigma^2} \right\} \qquad (2.4.11)$$

which is a Gaussian distribution with standard deviation given by :

$$\sigma^2 = R_0^2 \sum_{n\lambda} (2\lambda+1) \frac{\hbar}{8\pi D_{n\lambda} \omega_{n\lambda}} \qquad (2.4.12)$$

where $\omega_{n\lambda}$ is the frequency and $D_{n\lambda}$ the mass parameter of the collective mode $n\lambda$. The standard deviation may be calculated from $B(E\lambda)$ values with the relation :

$$\sigma_\lambda = \frac{r_0 A^{1/3}}{Z(\lambda+3)} \sqrt{(2\lambda+1) \frac{B(E\lambda)}{B_W(E\lambda)}} \qquad (2.3.13)$$

where $B_W(E_\lambda)$ is the Weisskopf unit defined in [Boh75] as :

$$B_W(E\lambda) = \frac{(1.2)^{2\lambda}}{4\pi} \left(\frac{3}{\lambda+3} \right)^2 A^{2\lambda/3} \quad (e^2 fm^{2\lambda}) \qquad (2.4.14)$$

or alternatively from deformation parameter β_2 with :

$$\sigma^2 = r_0 A^{1/3} \frac{\beta_2}{\sqrt{4\pi}} \qquad (2.4.15)$$

A projectile approaching a vibrating target-nucleus experiences a deformed potential at the moment fusion is about to take place. If only quadrupole and octupole deformations of the target-nucleus are considered, the effective potential can be written as :

$$V_{eff}(r) = Z_1 Z_2 e^2 \left[\frac{1}{r} + \frac{3}{5} s_2 R_2 \frac{1}{r^3} + \frac{3}{7} s_3 R_2^2 \frac{1}{r^4} \right] + \frac{L(L+1)\hbar^2}{2\mu r^2}$$

$$- \frac{V_0}{1+ \exp\{(r - s - R_1 - R_2)/a\}} \qquad (2.4.16)$$

where $Z_1, Z_2; R_1, R_2$ are the projectile and target nucleus charge numbers and radii respectively. The variables s_2 and s_3 are the variations in the target radius due to the quadrupole and octupole Z.P.M. ($s=s_2+s_3$). The first term in (2.4.16) is the Coulomb interaction containing a monopole, a quadrupole and an octupole term. In the same way as described in section 2.4.1 the transmission coefficients for barrier penetration may be calculated with the Hill-Wheeler parabolic barrier approximation. The fusion cross-section may then be calculated from :

$$\sigma_{fus} = \pi \lambda^2 \sum_{L=0}^{\infty} (2L+1) \langle T_L(s_2, s_3) \rangle \qquad (2.4.17)$$

where $\langle T_L(s_2,s_3) \rangle$ is the Gaussian weighted average of $T_L(s_2,s_3)$. Averaging is performed with respect to s_2 and s_3.

It should be noted that the assumption of a frozen shape during the fusion process is only valid if $\omega\tau << 1$, where ω is the vibrational frequency and τ the characteristic time for fusion. For example, an ^{16}O-ion with average kinetic energy of 10 MeV near the top of the barrier takes 9 10^{-23} s. to traverse a distance of 1 fm. A target nucleus excited to a state 0.5 MeV above the ground state has a vibrational frequency given by $\omega = E/\hbar = 7$

10^{20} s^{-1}, so $\omega\tau = 0.06$. However, at very low bombarding energies and for excitation to high-lying states, dynamical deformation effects should be considered. These effects have been studied by Esbensen et al. [Esb83]. They calculated barrier penetration coefficients with the coupled channels method, discussed in the next section, including the coupling between the relative motion of the nuclei and modes of surface vibration. A total hamiltonian of the following form was used :

$$H = \frac{-\hbar^2}{2\mu}\frac{\partial^2}{\partial r^2} + V(r,s) + H_{osc.} \qquad (2.4.18)$$

where $$H_{osc.} = \frac{-\hbar^2}{2D}\frac{\partial^2}{\partial s^2} + \frac{1}{2}D\omega^2 s^2 \qquad (2.4.19)$$

is the intrinsic hamiltonian for the surface vibration. Fig. 2.3 shows the calculated fusion probability as a function of energy at different values of $\hbar\omega$ for the system $^{148}Sm+^{16}O$.

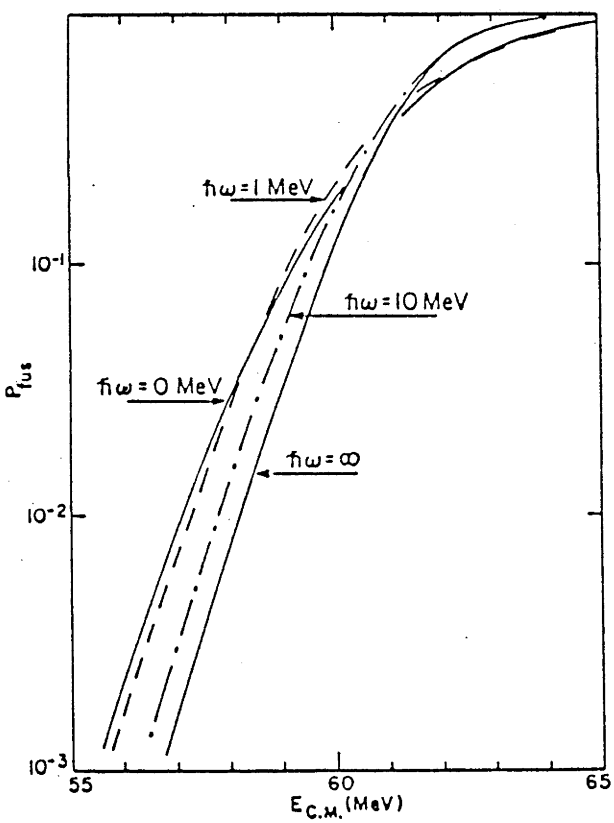

Fig. 2.3 Fusion probabilities for the reaction $^{16}O+^{148}Sm$ versus E_{CM}. The results were obtained from coupled-channels calculations, for various values of the one-phonon excitation energy $\hbar\omega$. The standard deviation of the ZPM amplitude was s=0.27 (fm). From [Esb83].

One of the conclusions of this study was that nuclear excitation during the barrier

penetration only leads to a minor modification of the frozen approximation ($\omega = 0$,s is finite) results, when the collective state is low-lying (say $\hbar\omega<1$ MeV). A further conclusion was that although giant quadrupole and giant octupole states in Sm have some effect, the dominant enhancement is due to low-lying states.

For many projectile-target systems it has been demonstrated [Esb81], [Pen83] [Vul86] that the Z.P.M. accounts for a large fraction of the sub-barrier fusion enhancement. Although strictly, the ZPM model should be used for systems with vibrational nuclei, it has been quite successful in reproducing experimental fusion data for deformed systems as well.

2.4.3 FUSION AND NUCLEAR DEFORMATION

An earlier attempt, to take surface degrees of freedom into account in the calculation of the fusion cross-section, was made by Wong [Won73]. He derived an expression for the fusion cross-section considering quadrupole deformation in the target-nucleus and projectile. As in the Z.P.M. model no dynamical effects were considered. Then the interaction potential becomes a function of the orientation angles of the nuclei :

$$V_N(r,\theta) = \frac{-V_0}{1+\exp[\{r - \sum_{i=1}^{2} R_i(1+\sqrt{\frac{5}{4\pi}}\,\beta_2^{(i)}P_2(\cos\theta_i))\}/a]} \qquad (2.4.20)$$

$$V_C(r,\theta) = Z_1 Z_2 e^2 \left[\frac{1}{r} + \frac{1}{r^3}\left\{\frac{3}{\sqrt{20\pi}}\sum_{i=1}^{2} R_i^2\beta_2^{(i)}P_2(\cos\theta_i) + \frac{3}{7\pi}\sum_{i=1}^{2} R_i^2(\beta_2^{(i)}P_2(\cos\theta_i))^2\right\}\right] \qquad (2.4.21)$$

where θ_i is the angle measured between the radius vector r and the symmetry axis of the i^{th} nucleus.

Because the interaction is now angle dependent, the angular momentum is not a good quantum number. However, in the model it is assumed that the perturbation on the orbital motion due to nuclear deformation is negligible, so that angular momentum may be considered as an approximate integral of motion.

The fusion-barrier may then be written as :

$$E_L(\theta_1,\theta_2) = E_0(\theta_1,\theta_2) + \frac{\hbar^2 L(L+1)}{2\mu R_0^2} \qquad (2.4.22)$$

where $E_0(\theta_1,\theta_2)$ is the barrier height in a head-on collision.

In expression (2.4.22)) it is further assumed that the radius, at which the interaction barrier is maximum, does not change much with L (so $R_L \approx R_0$). If also $\hbar\omega_L \approx \hbar\omega_0$ is used in the Hill-Wheeler approximation (2.4.7), the fusion cross-section can be written in an explicit form :

$$\sigma(E,\theta_1,\theta_2) = \hbar\omega_0 R_0^2 \ln\left[1 + \exp\left\{\frac{2\pi}{\hbar\omega_0}(E - E_0(\theta_1,\theta_2))\right\}\right] \qquad (2.4.23)$$

The total cross-section is obtained by averaging over all angles. Figure 2.4 shows fits to experimental fusion cross-sections with the Wong model for $^{16}O+^{208}Pb,^{232}Th$ [Mur86].

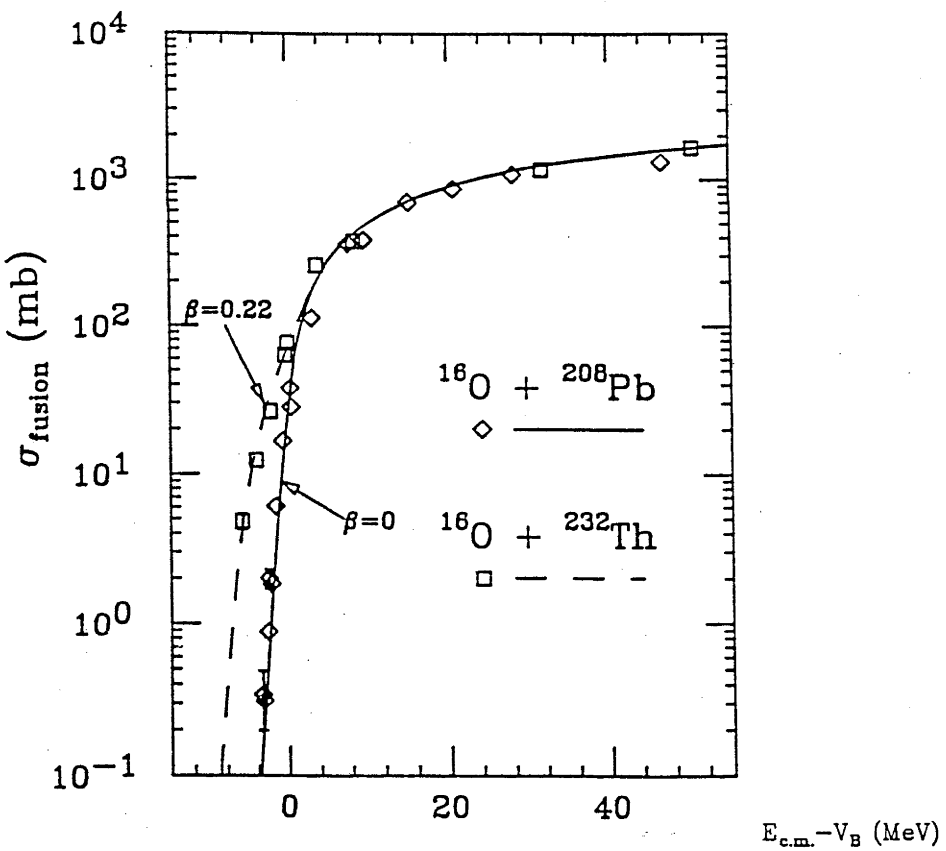

Fig 2.4 Fusion excitation functions calculated for $^{16}O+^{208}Pb$ (solid line) and $^{16}O+^{232}Th$ (dashed line). The value β=0.22 needed to fit the experimental data for $^{16}O+^{232}Th$ is in good agreement with the deformation parameters deduced from Coulomb excitation measurements. From [Mur86].

In a somewhat different approach the effect of target-deformation on the fusion cross-section was investigated by Stokstad and Gross [Sto81]. They studied the fusion reaction mechanism for the systems $^{148,150,152,154}Sm+^{16}O$. The fusion cross-section was obtained by solving the Schroedinger equation using a complex potential and equating the absorption cross-section to the fusion cross-section. Spherical real and imaginary nuclear potentials were found to reproduce the experimental fusion excitation function of $^{148}Sm+^{16}O$. The ^{148}Sm nucleus was considered to be spherical. For the other Sm isotopes fusion cross-sections were calculated for different orientations of the deformed target nucleus and were then averaged over orientation angles θ :

$$\sigma_{fus} = \int_0^{\pi/2} \sigma_{fus}(\theta) \sin\theta \, d\theta \qquad (2.4.24)$$

As in the Wong model the orientation of the nucleus was only specified by the polar angle θ, which is equivalent to the assumption that all collisions are head-on. Finite impact parameter collisions were considered by the addition of the usual cetrifugal potential for the collision of two point masses. The experimental fusion cross-sections for the different Sm-isotopes could well be fitted (fig. 2.5), but with much smaller deformation parameters (fig.2.6) than obtained from other methods (i.e. Coulomb excitation,muonic atoms and alpha scattering).

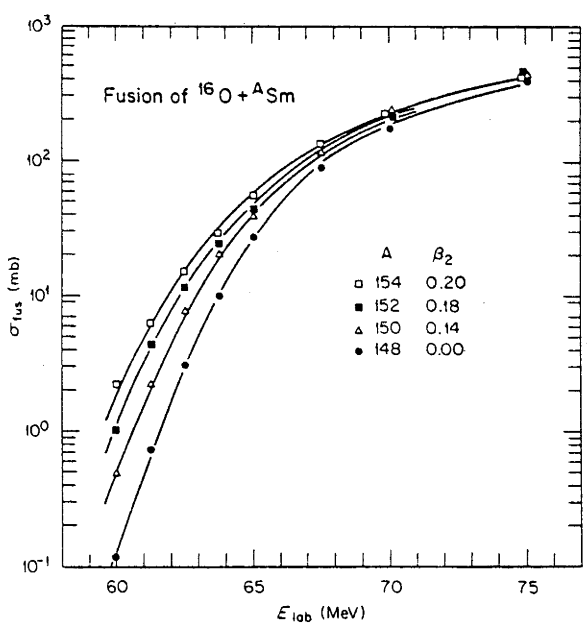

Fig. 2.5 Cross sections for the fusion of $^{16}O+$ $^{148,150,152,154}Sm$. The full curves are fits to the data as described in the text. From [Sto81].

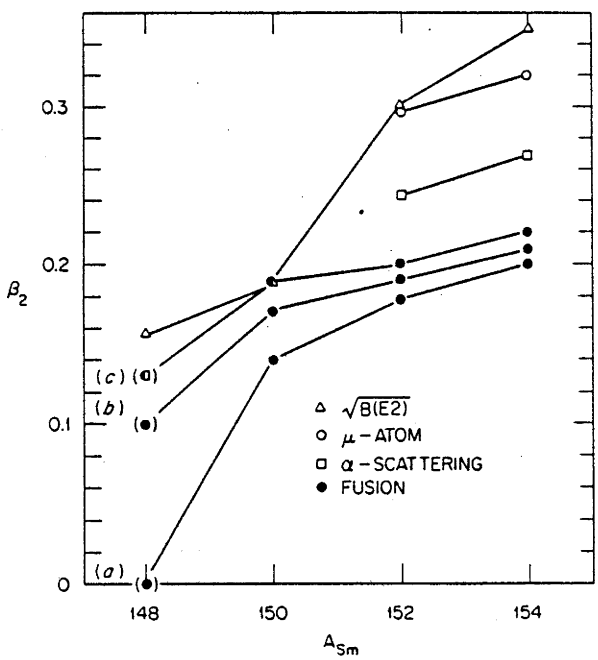

Fig. 2.6 Comparison of the values of β_2 deduced from fitting σ_{fus} with those deduced by other methods. The full dots indicated by a are obtained as described in the text. Those labeled with b and c are obtained by assuming deformation of the ^{148}Sm nucleus. From [Sto81].

To explain the discrepancy many different effects were investigated. It was concluded that also zero-point motion along with static deformation should be considered and that further studies of dynamical effects were needed (i.e. coupled channels).

The investigations by Wong and Stokstad showed the effect of quadrupole deformation on the sub-barrier fusion cross-sections. Calculations by Rhoades-Brown [Rho83] showed that nuclei with quadrupole moments and large negative hexadecapole moments have enhanced fusion cross-sections over elongated isotopes. Figure 2.7a shows the effect of introducing the negative hexadecapole deformation on the potential barrier for the system $^{184}W+^{16}O$. The curves correspond to U_A (δ_2=0.262,δ_4=-0.189); U_B(δ_2=0.262, δ_4=0) and U_C (δ_2=0,δ_4=0). Deformation parameters δ_2,δ_4 are defined in [Boh75] (page 139). The value of δ_2 is to first order given by δ_2=0.945β_2.

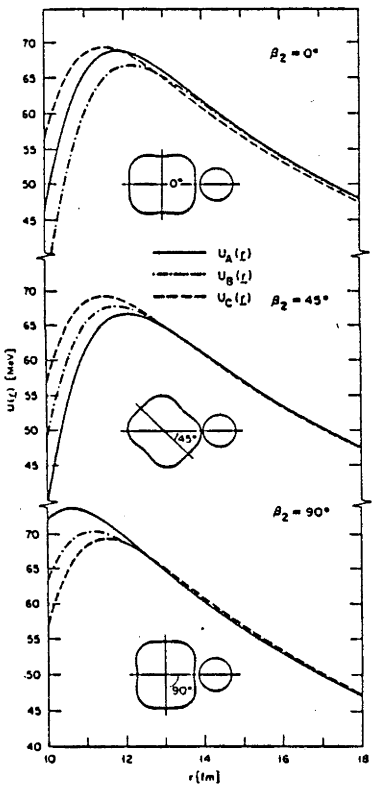

Fig. 2.7a Total nuclear plus Coulomb potentials for $^{16}O+^{184}W$, calculated for three values of the orientation angle β_2. The meaning of $U_A(r)$,$U_B(r)$ and $U_C(r)$ is described in the text. The inserts show a representation of the shape of ^{184}W with the deformation parameters of [Lee75]. From [Rho83].

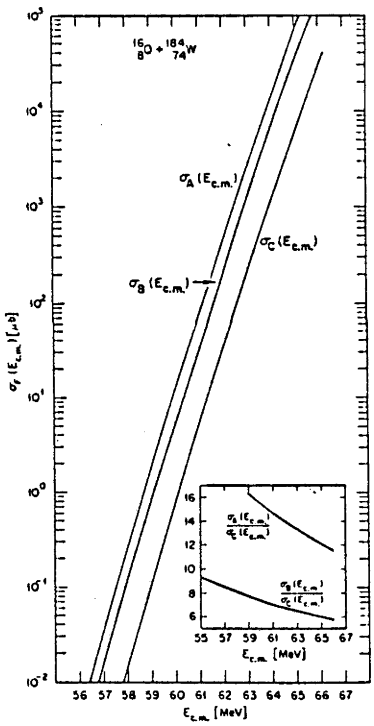

Fig. 2.7b Total fusion cross sections. The cross sections labeled σ_A,σ_B and σ_C correspond to the fully deformed system, zero hexadecapole moment and spherical, respectively. The inset shows the ratio of these quantities. From [Rho83].

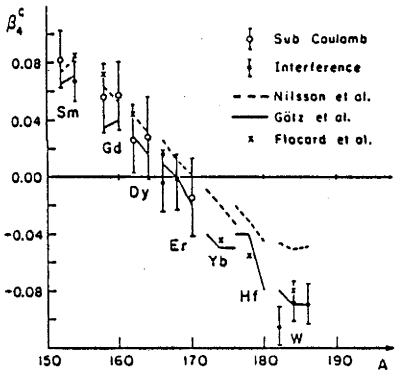

Fig. 2.7c Experimental and theoretical β_4 deformation parameters. From [Lee75].

In the 45° orientation the nucleus with hexadecapole deformation has the lowest barrier, because for this orientation the Coulomb force is smallest when nuclear matter start to overlap. The fusion cross-sections, calculated from these potentials by averaging the barrier penetration coefficients over all angles, are shown in fig. 2.7b.

Very few nuclei are known to have quadrupole deformation as well as a large negative hexadecapole moments (fig. 2.7c). From Coulomb excitation experiments [Lee75] and electron scattering measurements [Ron78] the ^{184}W and ^{180}Hf nuclei are suggested to be suitable candidates.

In chapter 5 it will be shown that the fusion cross-sections for different isotopes of tungsten and hafnium, which are expected to have different hexadecapole moments, do not show different degrees of enhancement.

DIRECT REACTION MODELS

2.4.4 COUPLED-CHANNELS METHOD

The coupled-channels formalism, described in section 2.3 in relation to elastic scattering may also be used to calculate the fusion cross-section. An extensive study into the role of channel coupling on the fusion cross-section has been made by the Copenhagen group [Das83a],[Das83b],[Das85]. To show how the coupled channels method can be used to calculate the fusion cross-section and to show the effect of channel coupling on the fusion cross-section, we will follow a simple description given by Dasso et al. [Das83].

The total Hamiltonian for a colliding system, described in one spatial dimension x is :

$$H = H_0(\xi) + K + V(x) + V_{cpl}(x,\xi) \qquad (2.4.25)$$

where H_0 is the intrinsic hamiltonian for the two colliding nuclei and ξ are the variables, describing the internal structures. The relative kinetic and potential energy are denoted by K and V, respectively. If the eigenstates of H_0 are given by :

$$H_0|n\rangle = \varepsilon_n|n\rangle \qquad (2.4.26)$$

then the total wave function describing the colliding nuclei may be expanded as :

$$\Psi = \sum \chi_n(x)\,|n\rangle \qquad (2.4.27)$$

From the stationary Schroedinger equation a set of coupled equations can be derived :

$$\left[-\frac{\hbar^2}{2\mu}\frac{d^2}{dx^2} + V(x) - E \right] \chi_n(x) = -\sum_m \varepsilon_n \delta_{nm} + \langle n|V_{cpl}(x,\xi)|m\rangle\, \chi_m(x) \qquad (2.4.28)$$

similar to equation (2.3.6). Here we are interested in the waves, which penetrate through the potential barrier. Thus an appropriate boundary condition to be imposed on the set of coupled differential equations is :

$$\chi_n(x) = \begin{cases} \delta_{n0}\exp(-ik_n x) + r_n \exp(ik_n x) & x\to\infty \\ t_n \exp(-ik_n x) & x\to\infty \end{cases} \qquad (2.4.29)$$

with $(\hbar k_n)^2/(2m) = E-\varepsilon_n$. The systems in their ground states are labelled with $n=0,\varepsilon_0=0$.

Boundary condition (2.4.29)) demands a plane wave in the entrance channel (n=0) traveling in positive x direction, reflected waves r_n from all channels in negative direction and transmission waves t_n in positive direction. Fusion may occur in each channel. The total transmission function is therefore the sum of the contributions from all channels :

$$T = \sum |t_n|^2 \qquad (2.4.30)$$

In order to derive analytical expressions for the transmission function, simplifying assumptions about the coupling interactions have to be made. Although this may distort the real situation to some extent, it provides a clear picture of the effects of channel-coupling on the fusion cross-section. The following assumptions are made :

1) The coupling interaction may be factorized into an intrinsic and a relative motion

part : $\langle n|V_{cpl}(x,\zeta)|m\rangle = F(x)G_{nm}$,and $F(x)=F_0$ is constant in the barrier region so that $\varepsilon_n\delta_{nm} + F_0G_{nm}=M_{nm}$.

2) The incident relative energy is large compared to the relevant intrinsic energies and the coupling strength, so that $k_n=k_0=k$.

With the coupling interaction independent of x a unitary matrix U_{mn} (independent of x) can be found, which diagonalizes M_{nm} and thus uncouples the set of differential equations. The transmission function may then be written as :

$$T = \sum_m |U_{m0}|^2 \, T[E,V(x)+\lambda_m] \qquad (2.4.31)$$

where $|U_{m0}|^2$ are given by the overlap-factors of the groundstate with the eigen-vectors of matrix M_{nm}. The constants λ_m are the eigenvalues of matrix M.

Expression (2.4.31) shows the influence channel-coupling has on the potential barrier. The effect of coupling is to replace the barrier V(x) with a set of barriers $\{V(x)+\lambda_m\}$. The total transmission function is a weighted average of the transmission functions for each effective barrier. In the classical barrier penetration description, enhancement of the fusion cross-section at sub-barrier energies is obtained if at least one eigenvalue λ_m is negative. It can be shown [Lan85] that the eigenvalues λ_m are distributed around zero. Hence any off-diagonal coupling interaction will cause an enhancement in the
transmission probability with respect to the no-coupling limit at energies below the original barrier and a reduction at energies just above the barrier, irrespective of the nature of the system.

Figure 2.8a shows the overlap weight-factors $\langle m|0\rangle^2$ as a function of the eigenvalues λ_m, calculated for a linearly coupled oscillator with :

$$M_{mn} = -nQ\delta_{mn} + F\{\sqrt{n}\,\delta_{n,m+1} + \sqrt{n+1}\,\delta_{n,m-1}\} \qquad (2.4.32)$$

and a fixed coupling strength F=2 MeV. [Das83]. Going from top to bottom of the figure the Q-values are -10,-5,-2 and -0.5 MeV. If the coupling is weak in comparison to Q the distribution is Poisson-like, whereas a Gaussian distribution is obtained as $Q\rightarrow 0$. In fig. 2.8b the corresponding transmission functions are shown. The transmission

function takes the form of a staircase for strong coupling instead of a step-function for no coupling. The Q→0 limit recovers the zero-point motion model (section 2.4) if it is assumed that $F(x)G(\zeta) = \zeta dV/d\zeta$.

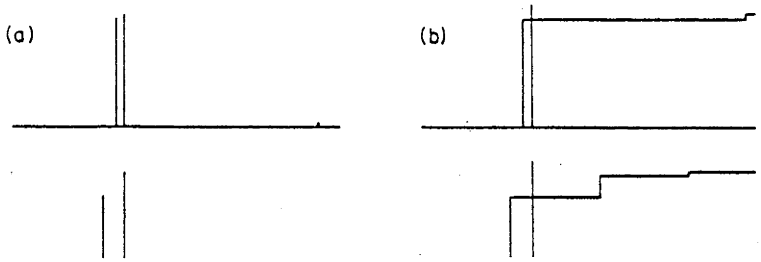

ERRATUM

Fig. 2.8 should appear before Fig. 2.9 on page 25.

enhancement are shown by the solid lines in part (a). The enhancement as a function of -Q for a fixed value of F=2 MeV is shown in part (b). From [Das83].

Fig. 2.9 shows the effect of finite Q-values on the sub-barrier fusion enhancement. The Z.P.M. model ignores Q-values effects and therefore tends to overestimate the enhancement, especially for systems with higher first excited states.

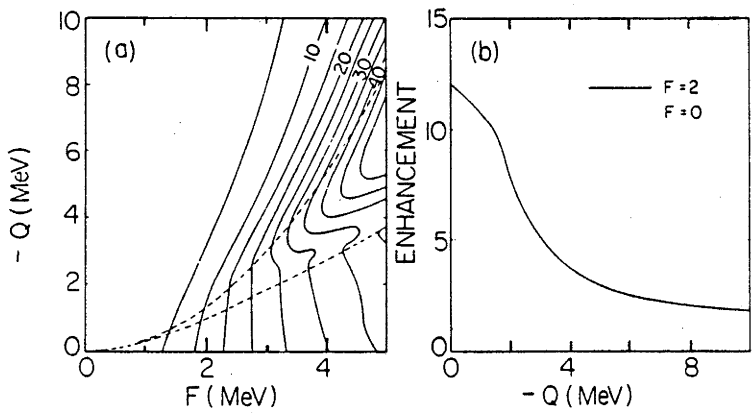

Fig. 2.8 Transition from weak to strong coupling limits with the linearly coupled oscillator. Part (a) shows the eigenvalues λ_m (abscissae) and the overlap weighting factors (ordinates) for a fixed coupling F=2 MeV and excitation energies - Q=10,5,2 and 0.5 MeV in order from top to bottom of the figure. The corresponding classical transmission coefficients as a function of the energy with respect to the barrier are shown in part (b). From [Das83].

A short-coming of all fusion models, discussed so far, is that the interaction potential is modified or channel coupling is introduced to describe the fusion process only. It would be desirable to describe various processes simultaneously on an equal footing. Extensive calculations were performed by Rhoades-Brown et al. [Rho84],[Pie85], who studied the system $^{208}Pb+^{16}O$, using a coupled channels method, described in [Rho80]. Different from the approach in which the fusion cross-section is calculated directly, including the effects of channel coupling, they described the most significant direct reaction-channels simultaneously and tried to obtain agreement with experimental data. The unitarity of the S-matrix was then used to obtain the fusion cross-section. The coupled channels calculation included the first 2^+, 3^- and 5^- excited states of ^{208}Pb and the first 3^- state in ^{16}O. Furthermore particle transfer channels were considered, describing the ^{17}O,^{15}N and ^{12}C reaction products. A short-range (r_i=1.0 fm) imaginary potential was used to take account of compound nucleus formation only. The real potential and the coupling interactions took care of the distribution of flux over the various channels. By adjusting the real potential good agreement with experimental excitation functions of various reaction-channels could be obtained (fig. 2.10 and 2.11). The reaction-channels considered in the calculations almost completely exhausted the total reaction cross-section, which was determined from elastic scattering. These calculations show that it is possible to predict the energy-dependence of elastic, quasi-elastic and fusion channels simultaneously with a single energy-independent real potential. It was found that particle-transfer channels took account of a large fraction of the sub-barrier fusion cross-section enhancement. Fig. 2.12 shows the partial reaction cross-section distribution decomposed in fusion, inelastic and transfer-channel components. There is a considerable reduction in the lower partial waves of the fusion cross-section due to transfer-channel coupling.

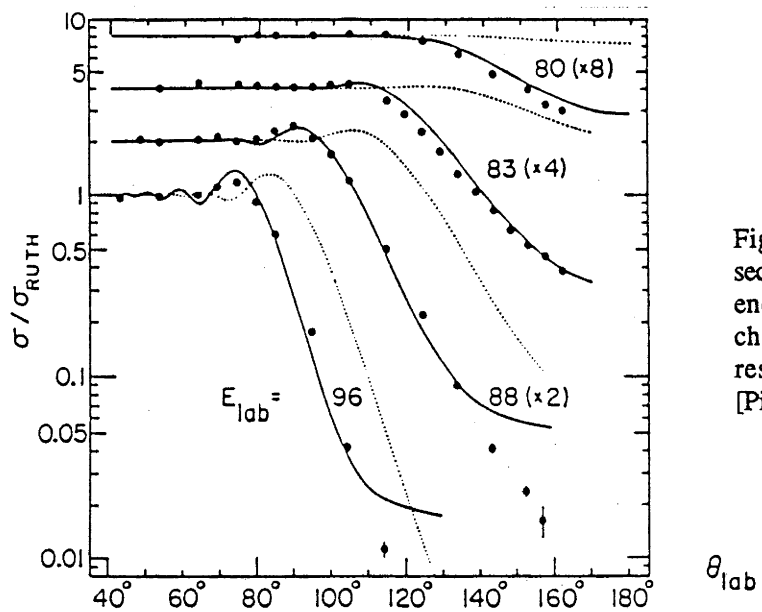

Fig. 2.10 Elastic differential cross sections for $^{16}O+^{208}Pb$ at the indicated energies. Solid curves are coupled channels results; dotted curves are results with no couplings. From [Pie85].

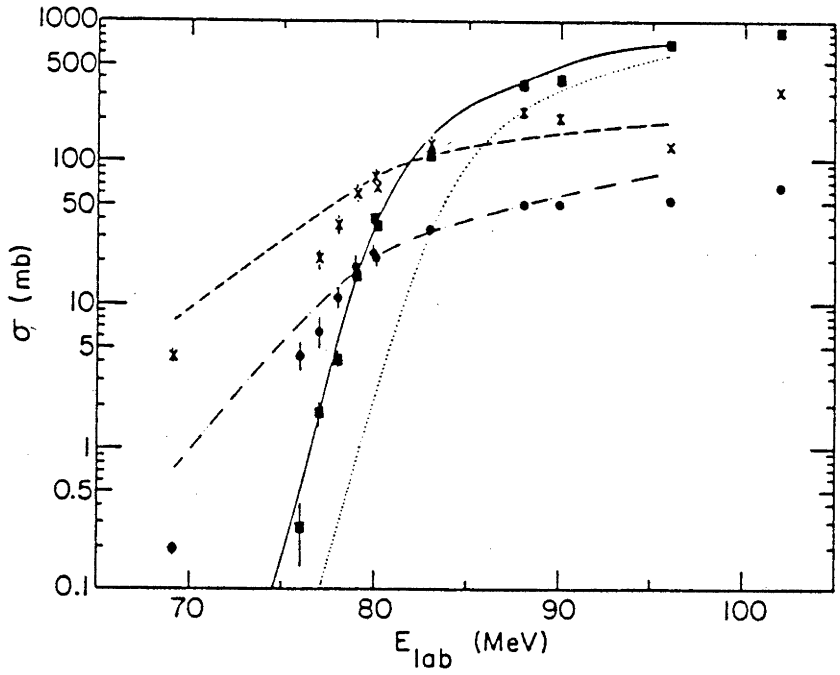

Fig. 2.11 Total cross sections versus E_{lab} for the $^{16}O+^{208}Pb$ system. Solid curve and boxes are fusion; dashed curve and crosses are total quasi-elastic; dash-dotted curve and dots are the (^{16}O,^{15}N) reaction. The dotted curve is single channel fusion. From [Pie85].

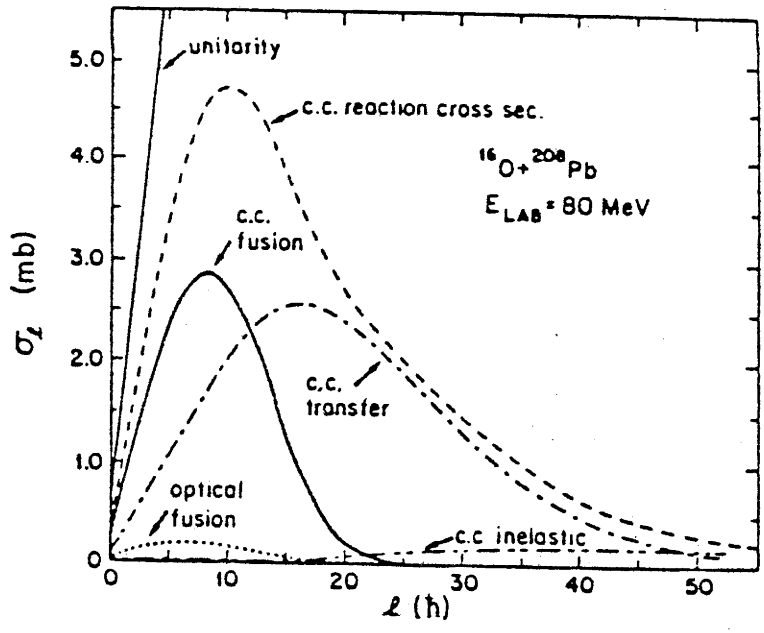

Fig. 2.12 Partial cross-sections as a function of angular momentum for the $^{16}O+^{208}Pb$ reaction at 80 MeV incident energy (lab). The various contributions to the reaction cross-section are indicated.

2.4.5 ELASTIC FUSION MODEL

Although less rigorous than the coupled channels method of Pieper et al., the elastic fusion model [Uda85] also describes fusion within the frame-work of the direct reaction theory. It uses the standard optical model to describe elastic scattering and fusion simultaneously. In the standard optical model calculation the Schroedinger equation is solved, using an optical model potential U = -V-iW :

$$(T + U)\chi(r) = E\chi(r) \tag{2.4.33}$$

where T is the total kinetic energy operator and $\chi(r)$ is the distorted wave function. As explained in section 2.2, the total reaction cross-section may be written as :

$$\sigma_R = \frac{\pi}{k^2} \sum_{L=0}^{\infty} (2L+1)\, T_L \tag{2.4.34}$$

It can be shown that :

$$T_L = \frac{8}{\hbar v} \int_0^{\infty} |\chi(r)|^2 \, W(r)\, dr \tag{2.4.35}$$

where $\chi_L(r)$ are the partial waves and v is the relative velocity. The basic idea of the model is to divide the absorptive potential W(r) into a direct reaction part and a fusion part W_F. The simplest division is a sharp cut-off potential :

$$W_F = \begin{cases} W & \text{for } r < R_F \\ 0 & \text{for } r \geq R_F \end{cases} \tag{2.4.36}$$

$$\text{with} \qquad R_F = r_F (A_1^{1/3} + A_2^{1/3}) \tag{2.4.37}$$

This leads to :

$$T_{F,L} = \frac{8}{\hbar v} \int_0^{R_F} |\chi_L(r)|^2 \, W(r) \, dr \qquad (2.4.38)$$

$$\sigma_F = \frac{\pi}{k^2} \sum_{L=0}^{\infty} (2L+1) \, T_{F,L} \qquad (2.4.39)$$

With optical model potentials from elastic scattering measurements Udagawa et al. were able to reproduce experimental fusion cross-sections for energies above the fusion barrier to far below the fusion barrier for a variety of systems with values of r_F from 1.46 fm for $^{148}Sm + ^{16}O$ to 1.42 fm for $^{124}Sn + ^{58}Ni$. Fig. 2.13 and 2.14 show some examples of the agreement obtained with experimental data. For the $^{152}Sm+^{16}O$ system no good fit could be found by varying parameter r_F only. It was pointed out that this could be due to fusion proceeding through direct reaction channels. Including the effect of the ($^{152}Sm\ 2^+$) inelastic channel was shown to improve the fit to the experimental fusion cross-sections.

The fusion angular momentum distribution, predicted by the elastic fusion model for $^{124}Sn+^{58}Ni$ at E_{cm}=180 MeV. is shown in fig. 2.15. Although this energy is well above the fusion barrier, there is a considerable reduction in the partial cross-sections ($\sigma_{F,L} \sim 1/2\ \sigma_{R,L}$) even for low L-values. The coupled-channels calculations for $^{208}Pb+^{16}O$,

discussed earlier, also predict a reduction for the lower partial waves, but not to such an extent as the elastic fusion model.

This feature of the elastic fusion model can best be understood considering the integrand A(r) of (2.4.38). Fig. 2.16 shows the intergrands for $^{124}Sn+^{58}Ni$ and $^{148}Sm+^{16}O$ for different L-values cross-sections up to L=60 ($\hbar$). For the $^{148}Sm+^{16}O$ system the integrand is much more broadly distributed and the maximum moves to larger r, as L increases. Here the difference between $\sigma_{R,L}$ and $\sigma_{F,L}$ is small at low L-values, but increases at higher angular momenta.

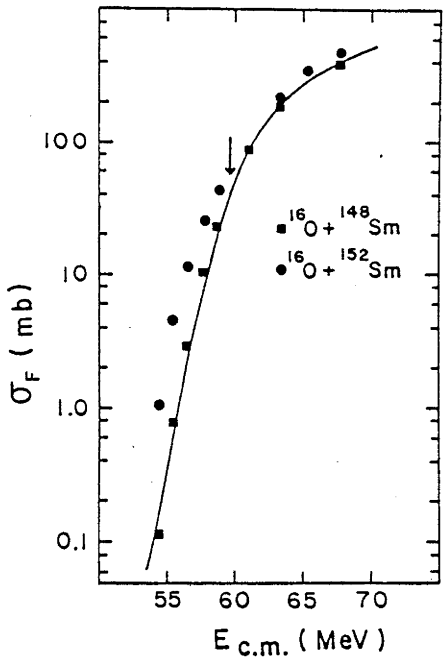

Fig. 2.13 Comparison of calculated (σ_{EF}) and experimental fusion cross sections for the $^{16}O+^{148,152}Sm$ systems. Since the calculated σ_{EF} for the two systems are almost identical, only one curve is shown. The arrow indicates the s-wave barrier-height. From [Uda85].

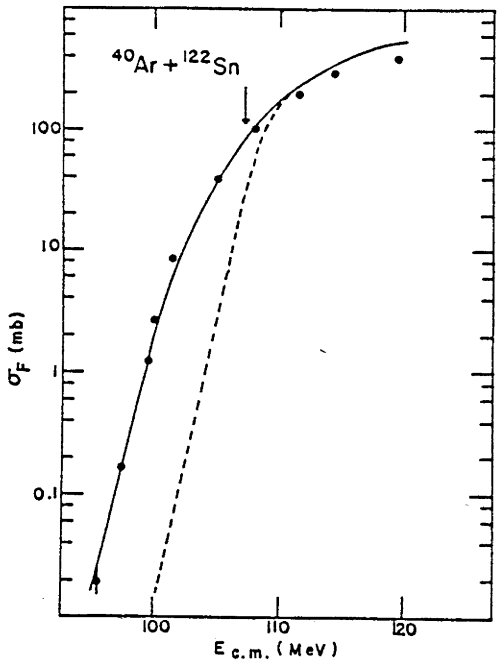

Fig. 2.14 Comparison between σ_{EF} and experimental cross-sections for the system $^{40}Ar+^{122}Sn$. The full and dashed curves are, respectively, the fusion cross-sections calculated by the elastic fusion theory and the barrier penetration method. From [Uda85].

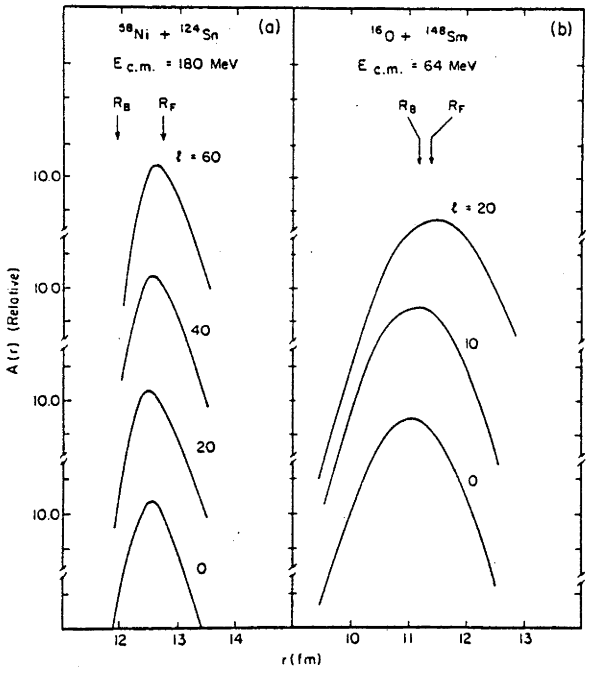

Fig. 2.16 Radial dependence of the integrands of eq.(2.4.38) for several values of the angular momentum L, for the $^{58}Ni+^{124}Sn$ and $^{16}O+^{148}Sm$ systems. From [Uda85].

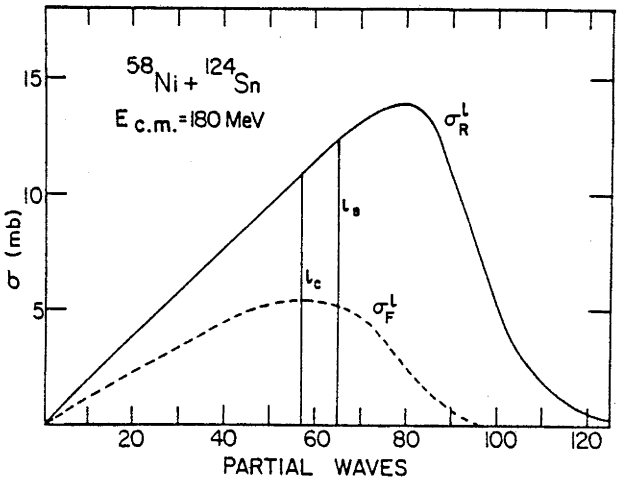

Fig. 2.15 Partial wave distributions of σ_R and σ_{Fus} predicted by the elastic fusion model for the system $^{58}Ni+^{124}Sn$ at E_{CM}=180 MeV. From [Uda85].

and at energies for which E_{cm}/V_b are the same (V_b is the fusion barrier-height). For the $^{124}Sn+^{58}Ni$ system the integrand A(r) is symmetrically distributed around a radius close to R_F and the peak of the distribution hardly changes from L=0 (ħ) to L=60 (ħ). This explains the factor 1/2 between the reaction- and the fusion partial

2.5 COMPOUND NUCLEUS DECAY

2.5.1 DECAY BY PARTICLE EVAPORATION AND GAMMA-RAY EMISSION

A hot rotating compound nucleus, formed in a heavy-ion fusion reaction decays by emitting particles and gamma-rays. In the first stage of the decay enough energy is available to overcome particle-binding energies and some combination of neutrons protons and alpha-particles are emitted. Because of the inhibiting Coulomb barrier far more neutrons than charged particles are emitted, provided that the compound nucleus is not too neutron deficient.. The emitted particles remove a large fraction of the internal kinetic energy and therefore cool the compound system. However, neutrons do not carry much angular momentum (on average ~0.7 (ħ) per neutron) The bulk of the compound nucleus spin is removed by gamma-ray emission. Figure (2.17) gives a schematic picture of the compound nucleus decay. It shows the excitation energy vs. angular momentum plane with the Yrast-line, which connects the states of lowest excitation energy for different angular momenta. Above the Yrast-line an entry-line may be defined which connects the states for which gamma-ray decay starts to compete strongly with neutron evaporation (not shown in fig. 2.17). After particle evaporation the compound nucleus arrives in a state near the entry-line and further decays by gamma-ray emission. Most of the gamma-rays are of E1 and E2 type [Gro67]. There are statistical gamma-rays (E1), which cool the nucleus, but do not remove much angular momentum and there are Yrast-like gamma-rays (E2) from transitions parallel to the Yrast-line.

For a residual nucleus in a state near the entry-line there are many different pathways to the Yrast-line. Individual transitions are therefore not resolved, one observes a continuous gamma-ray spectrum. For lower spins (<30 (ħ)) near the Yrast-line the pathways are less differentiated and individual transitions become visible in the gamma-ray spectrum.

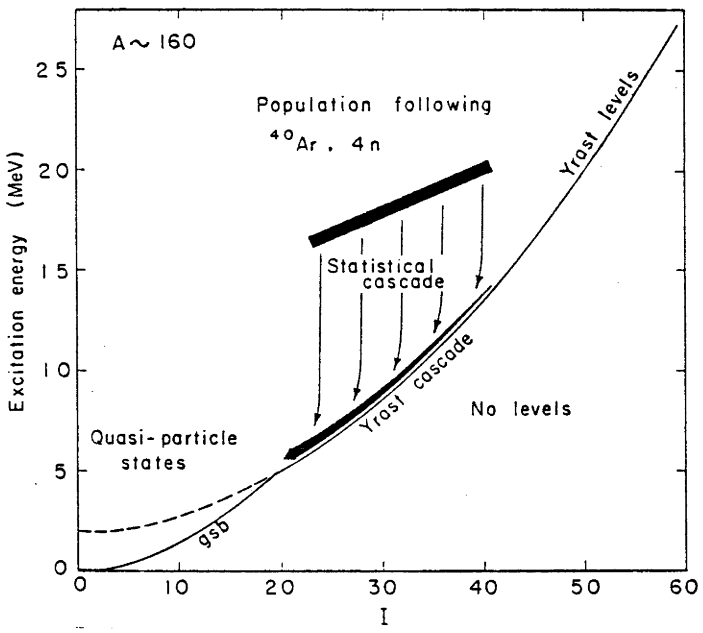

Fig. 2.17 Schematic picture of gamma-ray cascades following particle-evaporation deexcitation of a nucleus with mass around A=160. The populated energy and angular momentum range is shown. From [Ste72].

2.5.2 GAMMA-RAY MULTIPLICITY AND COMPOUND NUCLEUS ANGULAR MOMENTUM

Since the few neutrons emitted by the compound nucleus do not remove much spin, the angular momentum distribution of the residual nucleus is very similar to that of the compound nucleus. Thus the number of emitted gamma-rays (multiplicity) and their multipolarities directly provide the spin of the compound nucleus. The average multiplicity of gamma-rays may be measured with an array of NaI-detectors, which detect the number of gamma-rays associated with a single gamma-ray cascade. The nucleus from which the cascade originates is usually identified by simultaneous measurement of the energy spectrum with a high resolution Ge-detector. Coincidence with a gamma-ray of a characteristic transition (generally a ground-band transition), provides a selection of residual nuclei.

Since the detection efficiency of gamma-ray detectors is rather low and the detector array usually does not cover a 4π solid angle, not all gamma-rays from a cascade are detected. However,the average number of detected gamma-rays can be related to the gamma-ray multiplicities with the help of probability theory. Consider N identical

detectors with detection efficiencies Ω. The probability that k gamma-rays are detected out of a cascade of M uncorrelated gamma-rays can be expressed as :

$$P_k(M) = \sum_{n=k}^{M} P(\text{the N detectors are hit by n gammas}) \times P(\text{the n gammas are distributed over k detectors}) \qquad (2.5.1)$$

This expression takes into account that more than one gamma-ray from the same cascade may hit a detector, but still is counted as one hit. Because of the resolving-time, the detector cannot differentiate between gammas from the same cascade. The k-fold coincidence probability $P_k(M)$ may be written as [Hag75],[Wer78] :

$$P_k(M) = \binom{N}{k} \sum_{n=0}^{k} (-1)^{k-n} \binom{k}{n} [1 - (N-n)\Omega]^M \qquad (2.5.2)$$

where N is the number of gamma-ray detectors and Ω their average detection energy, which for simplicity is here assumed to be the same for all detectors. A one-fold coincidence corresponds to the detection of one gamma-ray in the Ge-detector and gamma-rays in one of the NaI-detectors. If more than one gamma-ray from the same cascade hit the same detector, it would be counted as one, because of the electronic resolving-time of the detector.

If the gamma-ray multiplicity distribution is denoted by ρ(M), then the experimental k-fold coincidence probability $P_{exp}(k)$ may be expressed as :

$$P_{exp}(k) = \sum_{M=0}^{\infty} \rho(M)\, P_k(M) \qquad (2.5.3)$$

Applying the binomial expansion to eq. (2.5.2) gives for the theoretical k-fold probability :

$$P_k(M) = \sum_{m=0}^{\infty} \binom{M}{m} m!\, A_{km}(\Omega) \qquad (2.5.4)$$

$$\text{where : } A_{km}(\Omega) = \frac{(-1)^m}{m!}\binom{N}{k}\sum_{n=0}^{k}(-1)^{k-n}\binom{k}{n}(N-n)^m\Omega^m \qquad (2.5.5)$$

Substitution of (2.5.4) into (2.5.3) results in the following relation between the experimental k-fold probability and the factorial moments of the multiplicity distribution :

$$P_{exp}(k) = \sum_{m=0}^{\infty}\sum_{M=0}^{\infty}\binom{M}{m} m!\,\rho(M)\,A_{km}(\Omega)$$

$$= \sum_{m=0}^{\infty}\langle\binom{M}{m} m!\,\rangle\,A_{km}(\Omega) \qquad (2.5.6)$$

By inversion of eq. (2.5.6) the moments of the multiplicity distribution may be obtained. In practice the detection efficiencies of the detectors may not be identical. Also the assumed isotropy in the gamma-ray emission is not correct. Corrections for these effects are discussed in [Wer78].

Conversion of the gamma-ray multiplicity to angular momentum requires information about the multipolarity of each gamma-ray. Because the statistical gamma-rays and part of the Yrast-line transition gamma-rays form a continuous energy spectrum, the number of E1 and E2 transitions can only be determined on average. Over a limited energy range it was found that on average ~4 statistical E1 gamma-rays are emitted. The remaining gamma-rays are from stretched E2 transitions. The conversion is then obtained from :

$$\langle L\rangle = 2(M_\gamma - 4) \qquad (2.5.7)$$

From thermal neutron capture reactions, where the average angular momentum brought into the compound nucleus is about

zero, it was found that $M_\gamma = 4 \pm 1$. This is in agreement with M_γ from (2.5.7) in the limit $\langle L\rangle \rightarrow 0$.

A number of publications on gamma-ray multiplicity measurements in relation to compound nucleus angular momentum distributions have been published [Van83],[Gil85],[Nol85],[Fis86],[Haa85],[Das85],[Ruc86].Vandenbosch and Gil et al. investigated the behavior of <L> as a function of bombarding energy for fusion of ^{154}Sm

with ^{4}He,^{12}C and ^{16}O. They showed the effect of the centrifugal potential on barrier penetration. The centrifugal barrier is inversely proportional to the reduced mass μ of the system. Thus for heavier projectiles more partial waves have barriers comparable to the incident energy and can be affected by barrier-penetration. From this point of view more spreading of the distributions is expected for systems with larger reduced masses. Figure (2.18) shows <L> as a function of $L_{crit.}$, which are the sharp cut-off L-values, adjusted to reproduce experimental fusion cross-sections.

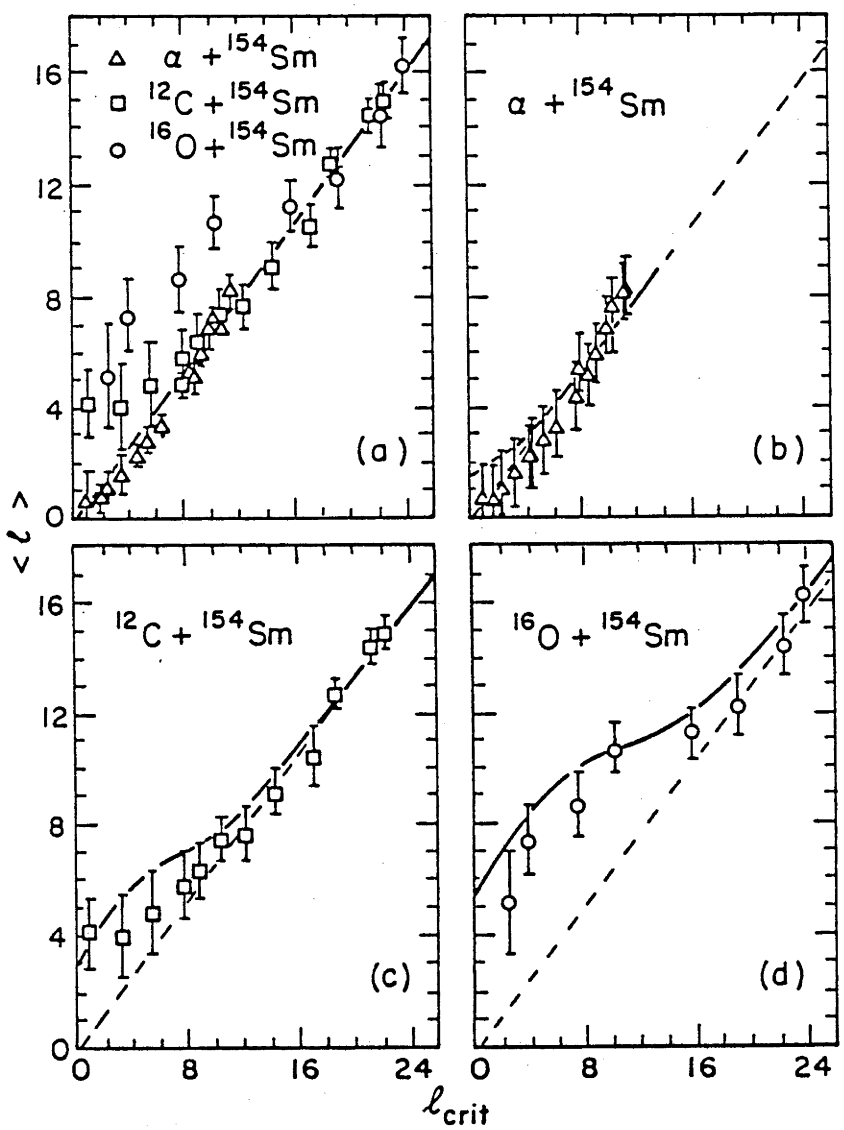

Fig. 2.18 Experimental values of <L> plotted versus L_{crit}. In (b),(c) and (d) the results for different systems are shown separately. The error bars of <L> include both the uncertainties in the measured multiplicities as well as the uncertainty in converting them to angular momentum. The solid curves are the predictions of the Wong model. From [Gil85].

For the system with the lightest projectile the <L>-values are consistent with $2/3L_{crit.}$, which are the average L-values of the sharp cut-off distributions. For the systems with the heavier projectiles deviation from this behavior is observed as the Coulomb-barrier energy is approached. This deviation is well reproduced by the Wong model.

One of the conclusions of this study was that at high bombarding energies the sharp cut-off distribution is a reasonable approximation. This, however, need not be correct. The Wong model predictions of <L> shown in fig 2.18 is also compatible with the data-points, but is rather diffuse even at energies well above the fusion-barrier. To make a statement about the shape of the angular momentum distribution, higher moments of the distribution have to be measured.

In this thesis it will be shown that the second moment of the spin-distribution, obtained from gamma-ray multiplicity measurements for a comparable system $^{159}Tb+^{19}F$, is not in agreement with the sharp cut-off model at energies well above the fusion-barrier.

2.5.3 DECAY BY FISSION

Compound nucleus decay by fission is often described using the concept of a rotating liquid drop. The idea of treating a nucleus as a charged liquid drop, possessing surface tension, originates from von Weiszacker [Wei35]. The effective potential energy of a rotating liquid drop is given by :

$$E = E_S + E_C + E_R \tag{2.5.8}$$

where E_S is the surface energy, E_C the electrostatic energy and E_R the rotational energy. If the surface, electrostatic, rotational and total energy of the nucleus in the spherical shape are denoted by : $E_S^{(0)}$,$E_C^{(0)}$,$E_R^{(0)}$ and $E^{(0)}$ then the deformation energy relative to the spherical surface energy may be written as :

$$\xi = \frac{E-E^{(0)}}{E_S^{(0)}} = \frac{E_S-E_S^{(0)}+E_C-E_C^{(0)}+E_R-E_R^{(0)}}{E_S^{(0)}} \tag{2.5.9}$$

$$= (B_S-1) + 2x(B_C-1) + y(B_R-1)$$

where $B_S=E_S/E_S^{(0)}$; $B_C=E_C/E_C^{(0)}$ and $B_R=E_R/E_R^{(0)}$ are dimensionless functions of the shape of the nucleus, which assume the value 1 for the spherical configuration. The quantity $x=E_C^{(0)}/2E_S^{(0)}$ is the nuclear fissility parameter, which is a measure of the size of the disruptive Coulomb force compared to the cohesive surface tension forces. Similarly $y=E_R^{(0)}/E_S^{(0)}$ is a measure of the disruptive centrifugal forces. The equilibrium shape of a rotating liquid drop with given values for x and y may be found from the condition $\delta E=0$ for all infinitesimal variations of the degrees of freedom, specifying the system.It depends on the nature of the stationary point (minimum,saddle point or maximum) if the equilibrium configuration is stable or not.
It can be shown [Mye74] that for $x\geq 1$, the nucleus has no equilibrium shape, and decays instantaneously by fission (even in the absence of rotation). In fig. 2.19 the rotating liquid drop configurations are shown (solid curves) for various values of x and y. Also shown are the shape configurations for which the stationary point is a saddle point (broken curves). On the bottom line y=0 (no rotation) the equilibrium shape is a sphere for all

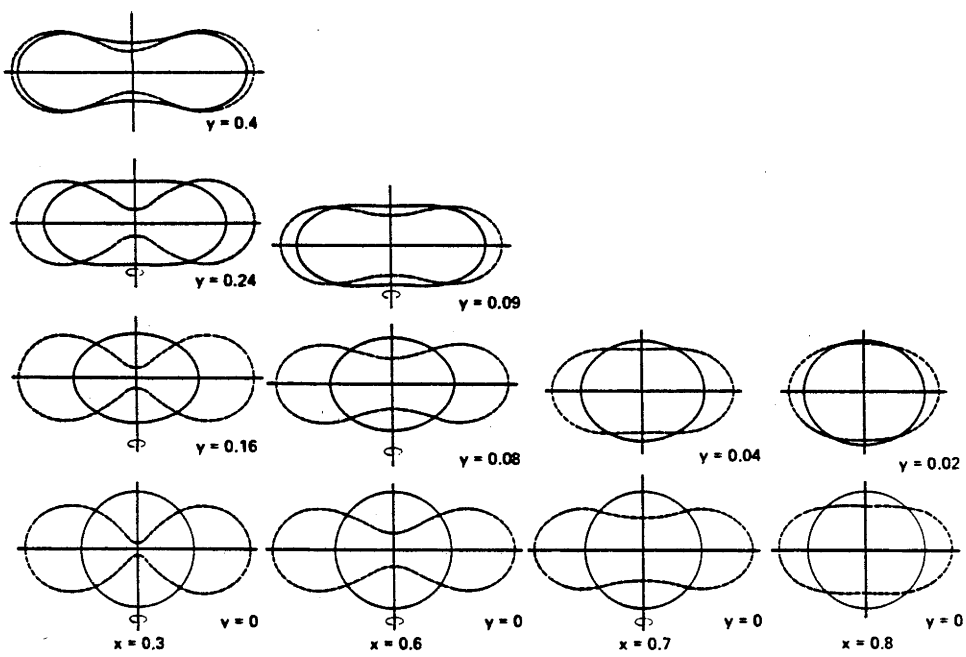

Fig. 2.19 Rotating liquid drop model (RLDM) configurations for various values of x and y. The smooth curves represent the equilibrium shapes and the dashed curves represent the saddle-point shapes. From [Bla82].

values of x. The saddle point shapes change with x and become more and more like the equilibrium shape as the fissility x increases. Introduction of rotation (y>0) brings the equilibrium point and the saddle point closer together. The minimum energy needed to overcome the remaining potential barrier between the two shape configurations is called the fission barrier, which is clearly angular momentum dependent. To calculate the fission barrier of a nucleus one must specify x and y. The surface energy, Coulomb energy and centrifugal energy may be calculated from [Mye67] :

$$E_S^{(0)} = c_2 A^{2/3} = 17.944[1 - 1.793\left(\frac{N-Z}{A}\right)^2]A^{2/3} \text{ (MeV.)} \qquad (2.5.10)$$

$$E_C^{(0)} = c_3 Z^2 A^{-1/3} = 0.7053\, Z^2 A^{-1/3} \text{ (MeV.)}$$

$$E_R^{(0)} = \frac{1/2\,(hL)^2}{2/5\,MR^2} = 34.54\, L^2 A^{-5/3} \text{ (MeV.)}$$

The parameters c_2 and c_3 were obtained from fits of liquid drop model masses to experimentally determined ground-state masses (Lysekil parameters).The shape functions B_S,B_C,B_R may be expressed in terms of Legendre polynomals. In this way R.L.D.M. fission barriers may be calculated for a nucleus specified by the value of x at different angular momenta specified by the value of y.

A modification to the L.D.M. fission barriers was made by [Kra79] and later extended to the R.L.D.M. by Sierk and Mustafa et al. [Mus82]. Fission barriers were recalculated including the effect of a diffuse nuclear surface and a finite range of the nuclear force. The finite range of the nuclear force brings the nascent fragments in the saddle point configuration closer together, which has the effect of a reduction in the fission barrier-height. This effect is most pronounced for lower mass systems, which have a low fissility and therefore a saddle point shape with considerable "neck" formation (see fig. 2.19). The nuclear surface energy was calculated using a Yukawa-plus-exponential potential as :

$$E_S = - \frac{c_2}{8\pi^2 r_0^2 a^3} \iint \left[\frac{|r - r'|}{a} - 2 \right] \frac{\exp -\{(r - r')/a\}}{|r - r'|} dr^3 dr'^3 \qquad (2.5.11)$$

where a is the range of the Yukawa potential. The constants a,r_0 and c_2 were obtained from fits to experimental ground-state masses. Figure 2.20 shows fission barriers as a function of angular momentum as predicted by the R.L.D.M. and by Sierk and Mustafa, including the finite range and diffuseness effects. Differences between the Mustafa and Sierk barriers are due to different nuclear shape parameterisations used.

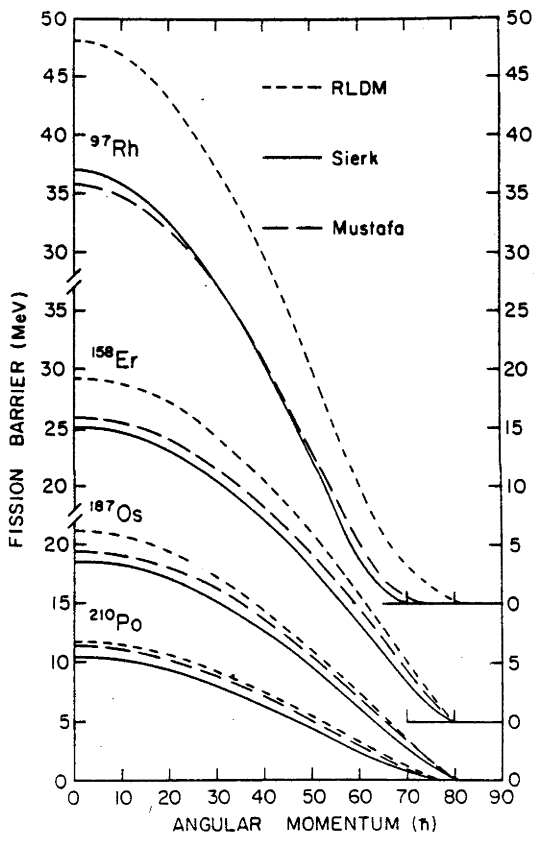

Fig. 2.20 Angular momentum dependent fission barriers from the RLDM and from the RLDM including effects of the finite range of the nuclear force and the diffuseness of the nuclear surface. (Sierk,Mustafa). From [Cha84].

2.5.4 THE STATISTICAL MODEL

In the statistical model description of compound nucleus decay it is assumed that once a compound system has been formed with a definite excitation energy E and angular momentum J, its decay is completely determined by the statistical weights of the various possible final states. In the first stage of the decay fission and/or particle evaporation are

the dominant modes although some weak competition does exist from electromagnetic decay via giant dipole resonances. After particle emission and fission is no longer possible, further decay proceeds entirely through electromagnetic interactions (gamma-ray and conversion-electron emission). The statistical weights of the various competing processes are proportional to the decay-widths. The decay-width for particle evaporation Γ_ν is given by [Zeb74],[Bec78] :

$$\Gamma_\nu(E,J) \propto (2s_\nu+1) \sum_{L=0}^{\infty} \sum_{J'=|J-L|}^{J+L} (2J'+1) \int_0^{E-B_\nu} \rho_\nu(E-B_\nu-E_R-\varepsilon)\, T_\nu^L(\varepsilon)\, d\varepsilon \qquad (2.5.12)$$

$T_\nu^L(\varepsilon)$ is the transmission coefficient for particle ν with kinetic energy ε carrying angular momentum L. The decay width is proportional to the level density in the residual nucleus, denoted by ρ_ν.The level density is dependent on the excitation energy in the residual nucleus $E-E_R-B_\nu-\varepsilon$, where E_R is the rotational energy of the residual nucleus and B_ν is the particle binding energy in the decaying nucleus. The integration in eq. (2.5.12) runs from $\varepsilon=0$ to a maximum available particle kinetic energy of $E-E_R-B_\nu$. The first summation is over all angular momentum-values L of the evaporated particle and the second summation is over the possible spin values J' of the residual nucleus. The factor in front of the summations accounts for the different orientations of the particle's intrinsic spin.

Generally the excitation energy of the compound system is high enough to assume a continuum of particle states. In the statistical model calculations described in chapter 5 a Fermi-gas level density expression was used [LeC59],[Lan66] :

$$\rho(E,J) \propto (2J+1) \frac{\exp(2\sqrt{aE})}{E^2} \qquad (2.5.13)$$

where a is known as the level density parameter.

The fission decay-width is derived from the transition state method of Bohr and Wheeler [Boh39]. This method assumes that if a nucleus attains the saddle point shape, it will undergo fission. The minimum energy needed to deform the nucleus from its equilibrium shape to the saddle point shape is the fission barrier, discussed in the previous section. The fission decay-width may be written as :

$$\Gamma_f(E,J) \propto \frac{1}{2\pi\rho(E,J)} \int_0^{E-E_{SP}(J)} \rho_f(E-k,J)\, dk \qquad (2.5.14)$$

where $\rho_f(E)$ is the level density in the saddle-point shape configuration. Expression (2.5.14) involves a summation over all saddle point states associated with a kinetic energy,k, in the fission mode. In the fission cross-section calculations of chapter 5 no shell or pairing effects are taken into account . It is assumed that due to the high excitation energies and the large angular momenta, associated with heavy-ion reactions, these effects are washed out. For a more detailed explanation see [Cha84],[Hin82].

CHAPTER 3
EXPERIMENTAL METHODS

In the course of the work described in this thesis measurements have been made of generalized-elastic, elastic and particle-transfer reaction cross-sections, and the cross-sections of evaporation residues and fission. All these particles must be reliably identified, and the absolute cross-sections determined.

In this chapter, experimental techniques will be discussed for each of the catagories. The theory of operation of the detectors used will be outlined, and their physical characteristics detailed. The experimental procedures used to ensure reliable results will be described, whilst finally general features of the experiments such as accelerator operation, vacuum system and target details will be discussed.

3.1 DETECTION TECHNIQUES

3.1.1 DETECTION OF ELASTICALLY SCATTERED HEAVY IONS

Elastic scattering is characterised by the conservation of the total kinetic energy. Other processes closely related to elastic scattering are inelastic scattering in which part of the kinetic energy is converted into excitation energy of the projectile, target nucleus or both, and transfer reactions in which neutrons or protons are exchanged between projectile and target nucleus. Measuring elastic scattering requires that all other reaction products be separated. Especially in heavy ion scattering where many transfer reactions take place this is not easily achieved. Reaction-products from charged particle transfer may be identified with the E-ΔE technique. In this detection method both the energy-loss (ΔE) in a transmission detector and the total kinetic energy (E) are measured. The rate of energy loss of a heavy ion with effective charge z and velocity v is given by the Bethe-Bloch relation :

$$-\frac{dE}{dx} \propto \left(\frac{z}{v}\right)^2 \ln\left(\frac{m_e v^2}{I}\right) \qquad (3.1.1)$$

where I is the average ionisation potential of the material and m_e the electron rest mass. An effective charge z is used to account for the fact that heavy-ions constantly change charge-state while traversing the medium. Expression (3.1.1) may approximately

be transformed into :

$$-\frac{dE}{dx} \propto \frac{z^2 M}{E} \qquad (3.1.2)$$

when the velocity v is written in terms of the kinetic energy ($v^2 = 2EM^{-1}$) and the logarithmic function is considered to be constant. This shows that reaction products differing in z^2M value are separated in the E-ΔE plane. Products from charged particle transfer reactions can readily be separated from elastic scattering events because of the change in z. The change in mass due to neutron transfer is mostly not sufficient to give a clear separation. In the following the elastic yield obtained from the E-ΔE method only will be called generalized-elastic.

Another method of identifying different reaction products is based on the deflection of moving ions in a magnetic field. When an ion in charge state q travels with velocity v through a magnetic field B, the trajectory will be circular with radius of curvature ρ given by :

$$\rho = \frac{Mv}{Bq} \qquad (3.1.3)$$

If the magnetic field-lines inside or at the boundaries of the magnet are shaped in an appropriate way, the ions can be made to converge to a focal plane. Ions with the same rigidity $B\rho = Mvq^{-1}$ will focus to one point in the focal plane. A position sensitive detector located in the focal-plane may be used to resolve reaction-products with different magnetic rigidities. Using the non-relativistic expression for the kinetic energy, (3.1.3) can be written as :

$$\frac{M}{q^2} \propto \frac{(B\rho)^2}{E} \qquad (3.1.4)$$

A combination of the E-ΔE technique with magnetic deflection allows the quantities Mq^{-2} and Mz^2 to be measured simultaneously, which in many cases identifies the reaction products uniquely.

3.1.2 DETECTION OF EVAPORATION RESIDUES

Evaporation residues (E.R.) are decay products of compound nuclei formed in fusion reactions. Specifically they result from the evaporation of a few particles (neutrons, protons,alphas) followed by a cascade of gamma-rays. Initially the compound nucleus moves in the same direction as the beam particles. The evaporated particles which are emitted in random directions in the centre-of-mass frame impart small recoil velocities to the compound nucleus which is then slightly deflected from its original direction of motion. However on average the velocity of the E.R. remains that of the compound nucleus (V_{cn}). The subsequent gamma-ray cascade does not remove any significant linear momentum. As a result the E.R. angular distribution is strongly forward peaked. This is more pronounced the higher the beam-energy or the heavier the projectile for a given target nucleus. More spread in the E.R. angular distribution can be obtained by means of multiple scattering in a thicker target. Because elastically scattered projectiles are not as much affected by multiple scattering as E.R. , some angular separation may be obtained. However, increasing the target thickness also increases the uncertainty in beam-energy. Especially at energies near the fusion-barrier this is undesireable, because the fusion cross-section changes very rapidly with energy. Hence the E.R. have to be identified in the presence of a strong flux of elastically scattered beam particles ($\sigma_{RUTH} \propto \sin^{-4}(\theta/2)$).

The kinetic energy of the elastic particles is much higher than of the E.R. So in principle the residues can be identified by measuring the kinetic energy. In practice however the detector has to be collimated to define the measuring angle accurately. Some elastically scattered particles will again be scattered and degraded in energy by the detector-collimator and produce a low energy tail in the energy spectrum. This low-energy tail of slit-scattered particles extends into the energy region of the E.R. ,which makes identification difficult. From equation (3.1.2) it would appear that the particles can be resolved using the E-ΔE technique. However, it should be noted that the effective charge of the E.R. is not the bare nuclear charge. Only a few electrons are stripped off from the compound nucleus. furthermore the logarithmic term in (3.1.1) changes rather dramatically with energy at low velocities. As a result the E.R. and the slit-scattered particles overlap in the ΔE versus E plane as can be seen in figure 3.1, which shows the calculated energy-loss in isobutane gas for different spieces as a function of energy. Evidently more information is needed to make clear identification possible. Our approach has been to utilise the large mass difference between the projectiles and the E.R. Information about the velocity and the kinetic energy should give a clear event signature.

The velocity was measured by means of the flight time over a fixed distance (90mm.) using the E-ΔT telescope described in section 3.3.3.

In a fusion reaction involving a projectile with mass m=20 and target nucleus M=160, which are typical values for the systems studied here, the velocities of E.R. (V_{cn}) and slit-scattered particles (V_{sc}) with the same kinetic energy are related by $V_{cn} = [m/(m+M)]^{1/2}\ V_{sc} = 1/3\ V_{sc}$. For a beam-particle energy of 90 MeV the compound nucleus kinetic energy may be calculated using conservation of momentum as : $E_{cn} = m/(m+M)\ E_{beam}$. This is 10 MeV for our system, which gives flight times of about 30ns and 10ns over the 90mm flight path for the E.R. and slit-scattered elastic particles with the same kinetic energy respectively. Assuming an energy spread for the E.R. of about 5 MeV, the difference in times of flight is still at least 15 ns. The time resolution of a few nano seconds for our E-ΔT telescope is more than adequate to resolve the two species.

In addition to the particles mentioned so far, fission fragments and recoil nuclei are also detected. However, the fission fragments have kinetic energies a factor 4 to 6 higher than the E.R. Recoiling nuclei have energies only about a factor 2 higher but their cross section is rather small at forward angles.

This detection technique was used to measure E.R. at beam energies well above the fusion barrier for which the cross section is of the order 100 - 1000 mb. At lower beam-energies identification is complicated, because of a decrease in E.R. kinetic energy and a dramatic increase in the ratio of slit-scattered elastic particles to E.R. . Measuring low cross-sections over a long time-period also requires high-stability in electronics and detector operation. A short-term instability may introduce spurious events in the E-ΔT region of interest. Because of the very low E.R. count-rate this is highly undesirable. To make identification of E.R. under these conditions more reliable, additional time of flight information was obtained using the 14 UD pulsed-beam facility, described in section 3.5.2. The R.F. signal associated with the beam pulses together with the telescope silicon surface barrier detector (s.b.d.) signal effectively provided the time of flight between the target and the E counter. Only events which showed the right time of flight in both time spectra were considered to be evaporation residues.

3.1.3 DETECTION OF FISSION-FRAGMENTS

The velocity of a fission fragment originating from the decay of a compound nucleus, formed in a heavy-ion induced fusion reaction, is determined by the vector sum of

the compound nucleus velocity and the asymptotic velocity of the fragment in the centre of mass frame. The fission fragment velocity in the center of mass system is dependent on the energy released in the fission process. This energy is divided between fission fragment excitation energy and kinetic energy of the fragments. An empirical relation for the average kinetic energy released in the fission process was found to be [VIO85] :

$$E_k = 0.1189\, Z^2 A^{-1/3} + 7.3 \quad (MeV) \qquad (3.1.5)$$

where A and Z are the mass and nuclear charge numbers of the compound nucleus.

For our typical compound system with m=20 ,M=160 and Z=75 the total kinetic energy released in the fission process is E_k=126 MeV. Assuming equal mass-split the fission fragment velocity in the centre of mass (C.M.) system is $V_{ff} = 1.389\, [E_k A_{cn}^{-1}]^{1/2}$ =1.2 cm/ns. At 90 MeV the C.M. velocity is $V_{cm} = 1.389\, [E/A_{proj}]^{1/2}\, A_{proj}/A_{cn} = 0.3$ cm/ns. Thus in contrast to E.R. the angular distribution of the fission fragments extends to backward angles. Therefore to obtain the total fission cross-section the angular distribution has to be measured over a much wider angular range. However, for the systems studied here it was found that the angular distribution in the center of mass frame was consistent with a $\sin^{-1}(\theta_{cm})$ dependence [Cha86]. This experimental fact was used in the measurement of low cross-sections. The fission yield was measured at one angle and the total fission cross-section was derived assuming a $\sin^{-1}(\theta_{cm})$ distribution.

As can be seen from figure 3.1, fission fragments can easily be identified with the E-ΔE technique. The separation from other reaction products is most pronounced at

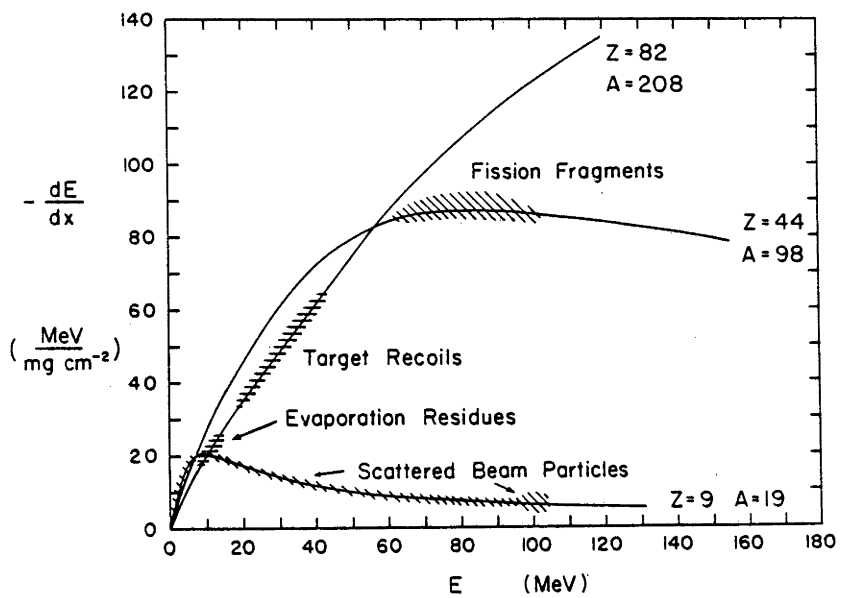

Fig. 3.1 Variation of -dE/dx with energy for various nuclear species in isobutane gas. (from [Cha84]).

forward angles [Oph82], at which the fragment kinetic energy is highest. Considering the intense Rutherford scattering at forward angles our choice of detection angle was between 45 and 60 degrees.

In measuring low cross-section fission yields similar problems arise as with E.R. When measuring over a long time-period, spurious counts appeared scattered all over the E-ΔE plane. The origin of these counts is not clear, they could result from cosmic radiation or activity in the scattering chamber.

To avoid this problem both fission fragments were measured. Care was taken to ensure that for every fission event in the E-ΔE telescope, the complementary fragment is recorded in the other detector. When the telescope is positioned at a certain angle the angle of the complementary fragment can be calculated from kinematics. This can be done for different mass-splits and assuming a variation in the total kinetic energy. From the results an estimate can be made of the solid angle required to detect all complementary fragments. Experimentally this was checked by measuring the coincidence rate as a function of complementary detector angle. Over a certain angular range the coincident fission yield was found to be constant. In the actual experiment the complementary detector was positioned in the center of that range. In addition to the E-ΔE information and the coincidence requirement, the fission fragments time difference and sum-energy were used so that fission events could be identified with confidence.

3.2 THEORY OF DETECTOR OPERATION

3.2.1 GAS IONISATION CHAMBERS

When a charged particle traverses a gas volume with high velocity it loses part of its kinetic energy to ionisation of the gas molecules. The electron-ion pairs created in this process can be separated by means of an applied electric field. At low field strength not all created charges are collected at the anode and cathode, due to trapping and the recombination of electrons with gas-ions. Raising the field strength initially increases the fraction of collected charge until a saturation current is reached. At still higher fields the accelerated electrons become energetic enough to ionise the gas molecules by themselves and in this way more charge is collected than was originally created by the ionising particle (gas amplification). In both the saturation current and gas amplification mode of operation the collected charge is proportional to the total original ionisation charge. The charged particle does not only lose kinetic energy due to ionisation but also by excitation of gas molecules. However, the competiton between ionisation and excitation of the gas

molecules is practically independent of the particle energy (above a few keV). For this reason the collected charge is not only proportional to the created charge but also to the energy deposited in the gas. On average the amount of energy needed to create an electron-ion pair in isobutane gas is about 30 eV.

In the experiments described in this thesis the gas ionisation chamber was operated in pulse mode, which means that the total electron charge is measured for individual ionisation events. Practical problems arise when currents, induced by individual ionising particles, are measured in the external circuit. The difference in mass between electrons and gas-ions gives rise to different collection times, which are typically in order of 1μs and 1ms for electrons and gas-ions respectively. Considering count-rate and energy resolution it is better to use the electron component of the induced signal only. However, the pulse-height of the electron induced signal, measured in the external circuit, is dependent on the position of the particle track in the detector, which degrades the energy resolution. A solution to this problem was found by placing a Frisch-grid [Bun49] across the detector. This grid, kept at a lower potential than the anode, screens the anode from the area between grid and cathode. Only electrons drifting beyond the grid contribute to the induced anode current-pulse. In this way the anode current is independent of the positive-ion collection and the pulse-height is independent of the particle-track position. A detailed calculation of pulse formation in ionisation chambers can be found in [Sta53].

3.2.2 GAS IONISATION and TIMING

In the above, the gas-ionisation process was discussed in relation to the measurement of particle energies. Gas-ionisation can also be used for fast timing. In particular, fast timing is achieved when high field gradients are used, which create an avalanche of secondary electrons. The electric field-strength is chosen as high as possible, but below the threshold at which voltage break-down occurs. The pulse-height is still proportional to the energy of the ionising particle. Best time-resolution is obtained with a parallel plane construction consisting of conducting anode and cathode foils at short distance (typically 1 mm.), which the particles traverse at right angles (parallel plate avalanche counters [Hem75] [Bre77],[Ste76]). The rise time of the anode pulse depends mainly on two effects. The variation in the time-interval between first ionisation and the start of electron multiplication and the time spread in collecting electrons from the multiplication process. In a planar avalanche counter the first effect is much smaller than the second because the field-strength is uniform. The rise time T_e of the electronic component of the signal is then approximately given by [Cof85] :

$$T_e = \frac{1}{\alpha V_e} \qquad (3.2.1)$$

where α is the first Townsend coefficient and V_e the average electron velocity.

Assuming V_e=5cm/ns and α =100cm^{-1} (estimated from the observed pulse height) then T_e=2 ns. A parallel plane construction, described above, is mainly used as a transmission detector for the timing of light particles. For heavier evaporation residues multiple scattering in the foils can cause considerable deflection. This may be prevented by replacement of the foils with planes of narrowly spaced thin wires [Lei81]. For an anode in the form of wires the electric field is non-uniform and a contribution from the first effect has to be considerable.

For a detailed theory of the electron avalanche process see [Ric74].

3.2.3 SOLID-STATE DETECTORS

Particle detection

Ionisation produced by a fast moving charged particle in a solid may be detected if the produced charge can be collected efficiently and if the net concentration of free charge carriers in the solid is low. The latter requirement is needed to keep the detector-noise as low as possible. A p-n junction provides a perfect charge-carrier free region. With a reversed bias across the junction this free charge depleted region may be extended and charge from traversing ionising particles can readily be collected. This detection technique is used in all surface barrier and diffused p-n junction detectors. An important difference between semiconductor detectors and the gas ionisation detectors is the much higher stopping power of a solid. Also the energy needed to create an electron-hole pair is about a factor ten smaller than the average ionisation potential of a gas, which greatly improves the statistical accuracy of the collected charge. These properties of solid detectors make them very useful in high-resolution energy measurements.

In the experiments described here silicon surface barrier detectors, manufactured at the ANU, were used. Silicon has a low intrinsic conductivity and can therefore be operated at room temperature without excessive leakage current. The p-n junction in a surface barrier detector is formed by surface oxidation of a silicon slice doped with phosphorus

(n-type). At the surface a strongly p-type layer is formed which creates the p-n junction. A detailed description on the manufacturing of s.b.d. is given in [Eng74] and references therein. In all experiments s.b.d. were used to measure the energy of fully stopped particles. The detectors were sufficiently thick to stop all species of interest. After a certain particle radiation-dose the s.b.d. shows deterioration in energy and time resolution accompanied by an increase in leakage current. Whenever radiation damage occurred the detector was replaced.

Detection of gamma-rays

Semiconductors are also used in the detection of gamma-rays. Mostly germanium is chosen because of its higher charge number. A disadvantage of germanium is the small gap between the valance band and conduction band, which makes cooling to liquid nitrogen temperatures nescessary to reduce thermal noise.

In gamma-ray absorption there are three processes of main importance: Compton scattering, the photo electric effect and pair production. A gamma ray entering the detector does not always lose all of its energy . Compton scattered gamma-rays or annihilation photons may escape from the detector. Compton scattering produces a low energy continuous spectrum, which may obscure low energy photopeaks. The Compton back-ground may be reduced by surrounding the detector with a Compton-shield of NaI. Gamma rays, which are Compton scattered in the Ge-detector traverse the NaI-shield in which they may produce scintillation-photons. These photons are detected by the photo-sensitive cathode of a photo-multiplier tube. Events which produce signals in both the Germanium detector and the Compton-shield are rejected.

NaI crystals are also used for gamma-ray energy measurements. The gamma-ray detection efficiency of a NaI-detector is higher than of a Ge-detector, but the energy-resolution is worse.

3.3 DETECTORS USED IN EXPERIMENTS

3.3.1 MULTI-ANGLE GAS IONISATION-CHAMBER

The elastic scattering experiments were performed with a nine-angle gas ionisation-chamber. It consists of nine E-ΔE telescopes 6 degrees apart, and each telescope consists of an entrance window, a ΔE gas counter and a silicon s.b.d. The ΔE

signals are obtained from electron collection on anode planes of 10 cm. length. All anode planes have Frisch-grids which are interconnected and capacitively coupled to a common cathode plane. The anode-grid-cathode distances are 10 and 48 mm. respectively. The nine detector window-holders can be screwed in the detector-frame and are vacuum sealed with O-rings. A gas inlet is attached at the side of the detector, which may be connected via a flexible bellows to a gas handling system outside the scattering chamber. The radius of curvature of the array of telescopes is 300 mm. A picture of the 9 angle gas ionisation detector in the 2 m. diameter scattering chamber is shown on the following page. The detector is attached to an arm, which can be rotated electronically. In the lower left corner of the photograph the beam-collimators are visible. A target-wheel, which can hold up to six targets is attached to the lid of the scattering-chamber and comes in position when the lid is lowered.

3.3.2 FOCAL PLANE DETECTOR

The focal plane detector, which was used in the high resolution elastic scattering measurements with the Enge magnetic spectrograph, is a position-sensitive gas ionisation detector [Oph78]. A cross sectional view of the detector is shown in fig. 3.2. It consists of a large area cathode, two grids and an anode made up of several different elements. The anode planes, two ΔE and E-residual, collect electrons from that part of the particle-track

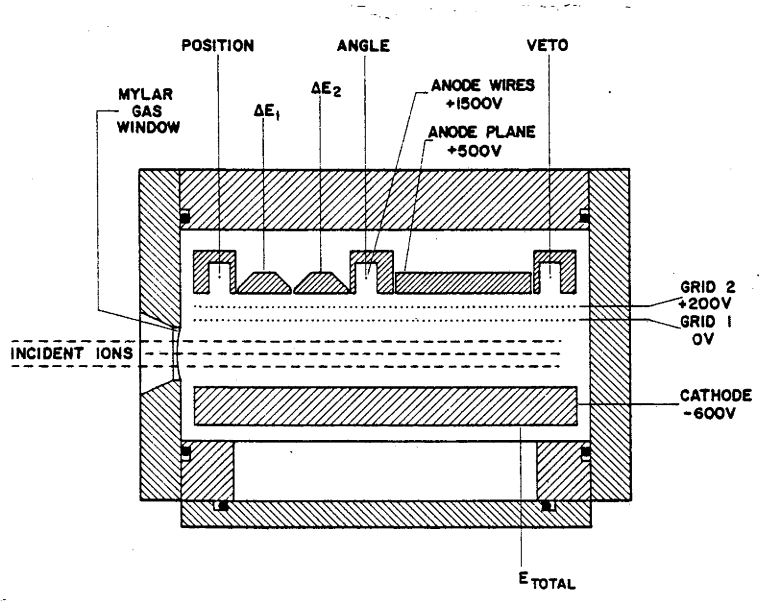

Fig. 3.2 Sectional view of the focal plane detector, showing its electrode structure (from [Oph78]).

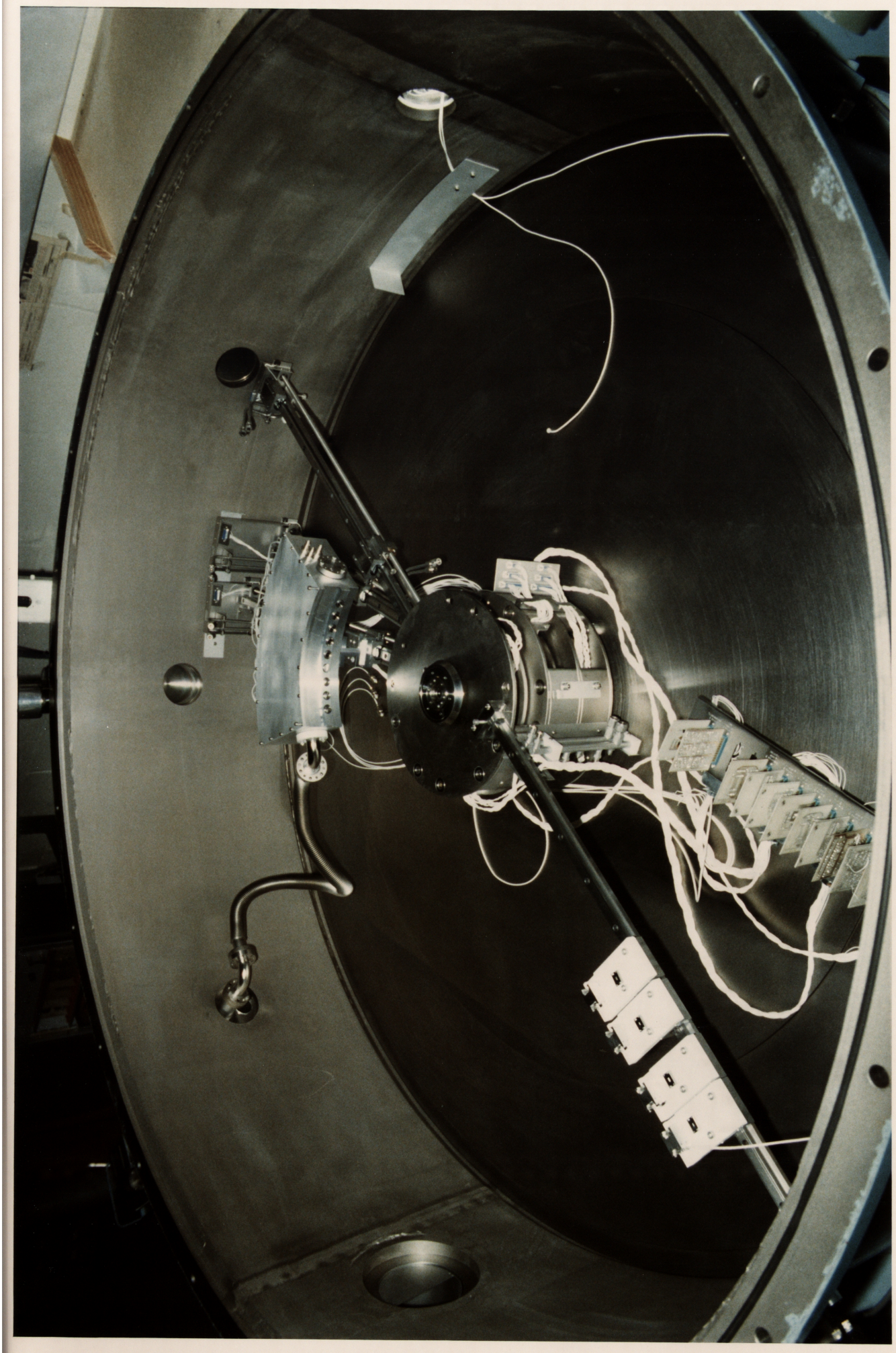

covered by the planes. The created positive ions drift slowly to the cathode inducing a signal with a long rise-time, which is unsuitable for energy determination. However, the electronic component of the signal induced at the cathode may be used to measure the total energy if the particle is stopped in the active gas volume, which is true in the absence of a veto signal from the wire at the back of the gas volume. Because grid 1 is capacitively coupled to the cathode the fast component of the cathode signal is formed by induction from electrons drifting beyond grid 1. The region between this grid and the cathode forms essentially a Faraday cage. The dots indicated with position, angle and veto are highly resistive wires (1700 Ω/mm) consisting of a layer of pyrolitic graphite deposited on a fine quartz fiber. Because of the high resistance the distributed capacitance along the wire introduces an RC delay line. Consequently, the rise times of the signals appearing at either end of the wire are proportional to the distance between each end and the site of the ionising event.

By measuring the position signals from two wires the angle of incidence can also be determined and is used for correcting the ΔE signals so as to maintain good ΔE resolution when the spectrograph is used with large solid angle. The position and angle wires are operated at potentials between 1500-2400 Volts depending on the gas pressure. These high potentials give a gas amplification factor of ~20. The performance of the detector i.e. the position and energy resolution depends on the window thickness and the gas pressure. For a given particle and energy a minimum gas pressure should be chosen to stop the particle in the active gas volume and a minimum window thickness strong enough to withstand the pressure.

3.3.3 EVAPORATION RESIDUES DETECTOR

A time of flight telescope was designed for the measurements of E.R. The telescope consists of a multi wire proportional counter (M.W.P.C.) and a silicon s.b.d. enclosed in a gas ionisation chamber. The existing M.W.P.C. [Lei81] had been constructed following a design of Breskin [Bre77]. It consists of three wire planes, a central anode sandwiched between two cathode planes at 3.2 mm distance. Gold plated tungsten wires 20 μm. in diameter are soldered at 1 mm. spacings on annular printed circuit boards. The three circular boards 15 mm. in diameter are enclosed in a solid state detector-can, used in this laboratory.

Both cathode planes make electrical contact with the metal detector-can while the anode wires have a common connection to a microdot feedthrough attached to the can. A cross sectional view of the M.W.P.C. is shown in figure 3.4 . The distance between the M.W.P.C. and the silicon s.b.d. is 90mm. In the design of the telescope special attention

was paid to compactness and accessibility to the detector components. Both detectors are mounted on a bracket which together with the microdot vacuum feed-throughs are attached to the lid of the detector chamber. A gas inlet is provided at the bottom of the chamber to be connected via a flexible bellows to a gas handling system outside the scattering chamber. The telescope entrance window consists of a 7 mm. diameter threaded hollow bolt to which a formvar film may be attached. All removable parts such as the window-holder , the gas inlet flange and the detector-chamber lid are vacuum sealed by means of O-rings. Blind tap holes are open to the vacuum system by means of pump holes at the bottom of the threads. This prevents gas being trapped in cavities, which may cause long pumping time due to tiny leaks between the cavity and the vacuum system.

A collimator together with an electron deflection magnet may be attached to the window holder. A cross sectional view of the telescope inside the ionisation chamber is shown in figure 3.5. To provide a beam current reading when the detector chamber intercepts the beam ($\theta < 3^{\circ}$) a tantalum strip is mounted on the window holder. The strip is electrically insulated from the metal frame with macor.

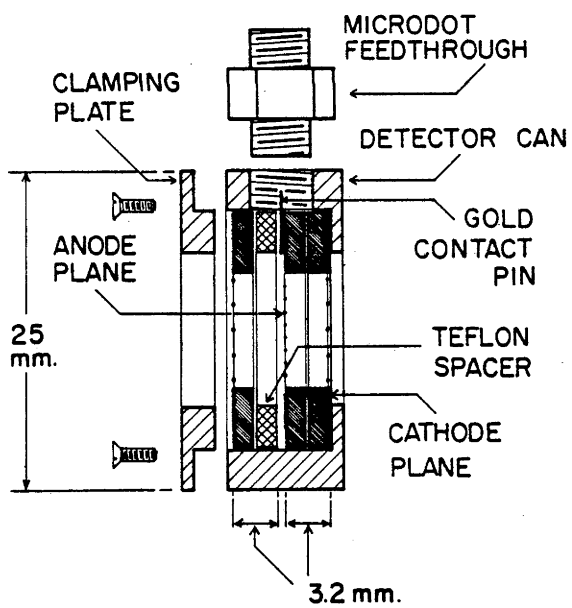

Fig. 3.4 Sectional view of the M.W.P.C.
(from [Lei81]).

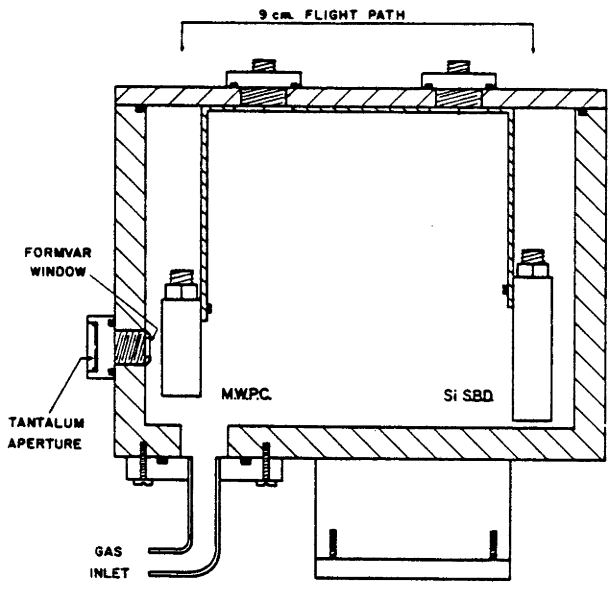

Fig. 3.5 Sectional view of the time of flight telescope inside the gas chamber. During operation the gas-inlet is attached to flexible bellows, which are connected connected to the gas-handling system outside the scattering chamber.

3.3.4 FISSION FRAGMENTS DETECTOR

For the fission fragment measurements the same ionisation chamber was used as for the E.R. experiments. The M.W.P.C. was replaced with a ΔE counter consisting of a 4 cm. long anode electron collection plane accompanied by a parallel Frisch-grid plane at 15 mm. distance. The chamber`s metal frame acted as a cathode, which may have introduced non uniformity in the electric field. However, for the purpose of detecting fission fragments this was of no significance.

3.4 EXPERIMENTAL PROCEDURE

3.4.1 GENERALIZED-ELASTIC SCATTERING

Angular distributions of elastically scattered beam particles were measured in a 2m. diameter scattering chamber. Reaction products were detected simultaneously in eight of

the nine gas-ionisation surface-barrier detector telescopes, described in section 3.1. The ninefold gas ionisation detector telescope was mounted on a movable arm at 300 mm. from the target. Rotation of the arm was controlled electronically and angles could be selected with 0.05 degrees accuracy. The angular distance between each detector telescope and the absolute angle of the movable arm were determined from elastic scattering measurements of ^{18}O ions from a 2 mm. wide gold strip target at 65 MeV beam energy. At this energy the elastic scattering is assumed to be pure Rutherford. Yields were measured in each of the eight detectors at two arm positions 36 degrees apart. The ratio of yields for each detector was compared with the Rutherford cross section ratio from which absolute detector angles could be determined. The results of this angle calibration will be shown in the next chapter.

In front of each detector window a 2 mm. diameter collimator was placed subtending a 0.4° angle or solid angle of 35 μSr. Strip targets 1 mm wide were used to restrict beamspot variations. Isobutane gas at 30 mbar. pressure was used as ionisation gas. The gas was kept separated from the vacuum system with 80 $\mu g/cm^2$. thick formvar windows in front of each detector telescope. During the experiment the gas was renewed whenever there were signs of gas deterioration, which manifested itself through a decrease in ΔE signal. Gas pressures could be changed with a gas-handling system which was connected to the detector via a flexible bellows inside the scattering chamber. Beams were monitored for normalisation with two silicon s.b.d. at 15° on both sides of the beam-axis. Reaction products could be measured over an angular range from 30 to 160 degrees. Forward angles were limited by the presence of the monitor counter.

ELECTRONICS. During the experiment all detector signals were pre-amplified and sent to the control room for further processing. The electronics used for the data processing is shown in figure 3.6. It effectively reduces the nine detector signals to three data words containing the energy, Δ-energy and an identification word indicating which detector had fired. These three words as well as the monitor signals were stored on magnetic tape. All gate signals were recorded with scalers for dead-time determination in the ADC`s and the HP21MXE processing computer. The explanation of abreviations used in fig. 3.6 is given in table 3.1.

3.4.2 ELASTIC SCATTERING

Angular distributions of elastically scattered ^{18}O particles from a ^{150}Sm target were measured with the Enge magnetic spectrograph of the ANU. A relatively thin, 1 mm. wide

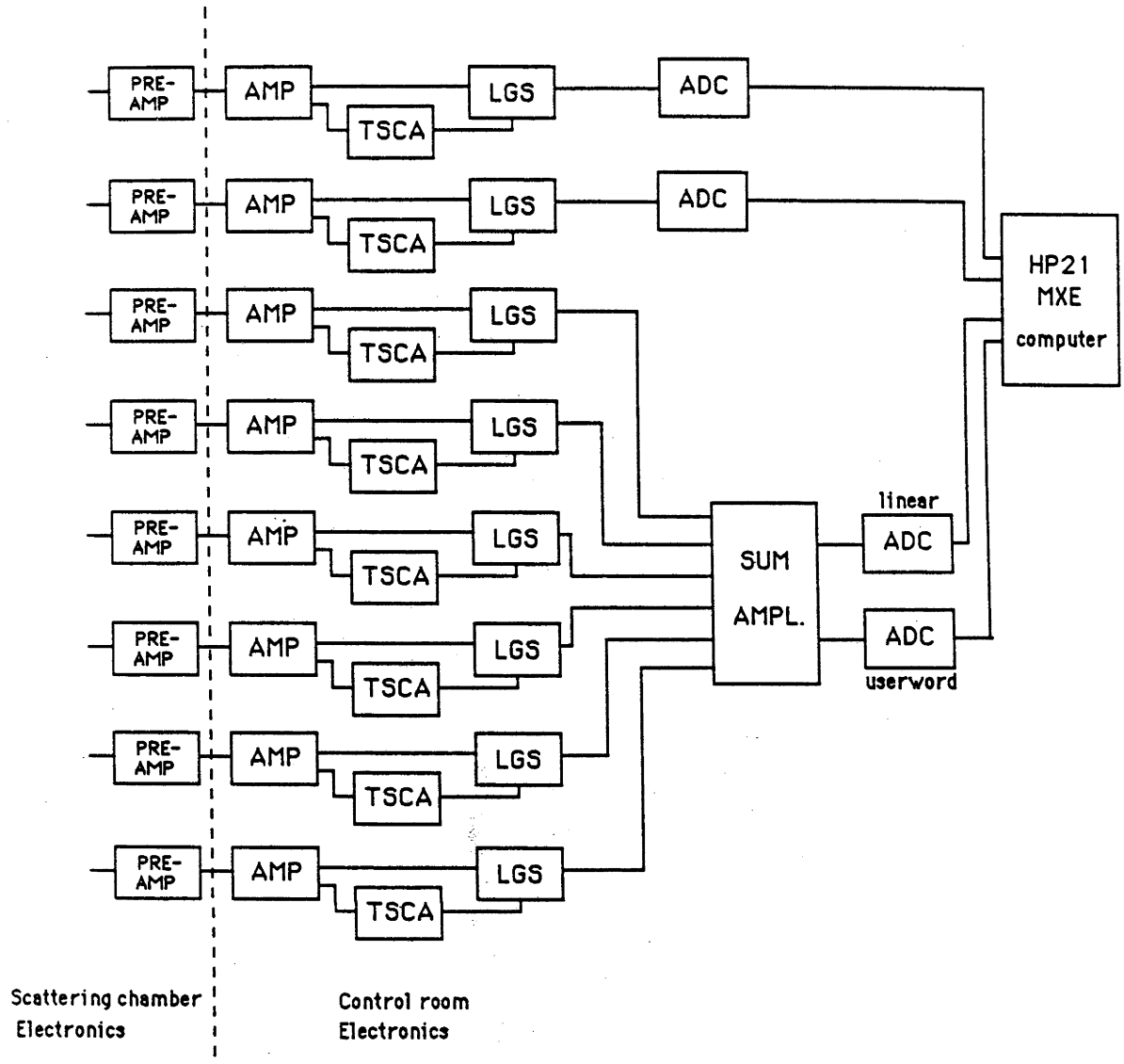

Fig. 3.6 Electronics scheme employed in the elastic scattering experiments with the E-ΔE detection method. Electronic units are identified in Table 3.1.

strip target, of 30 $\mu g/cm^2$ evaporated on a 15 $\mu g/cm^2$ carbon backing, was placed in the center of a 51 cm. diameter scattering chamber, located in front of the Enge spectrograph.

The calculated energy-loss in this target is about 50 KeV., which enables resolution of the first 2^+ excited state in ^{150}Sm at 334 KeV. Two monitor detectors at +15° and -15° degrees were used to normalize elastic yields, measured at different angles. At every angle measured, reaction products within 1.5° horizontal and 4.5° vertical acceptance angles (1.4 mSr.) were analysed by the spectrograph.

For a given magnetic field strength, particles within a limited energy range are

focussed into the focal plane. In heavy-ion scattering the particle energy changes considerably with scattering angle. Therefore the focal plane detector-position had to be adjusted with each change of angle. This re-adjustment is known as kinematic shift correction. The positioning of the focal-plane detector was electronically controlled. The appropriate magnetic field-strengths and detector position coordinates for each angle were obtained from a computer program, which calculated the corrections to compensate the kinematic shift.

The focal plane detector, described in section 3.2, was operated at 180 Torr. pressure which was sufficient to stop elastically scattered ^{18}O ions in the active gas volume at the highest bombarding energy (100MeV.) measured. The isobutane ionisation gas was kept inside the detector with a 2.5 μm thick mylar window.

3.4.3 EVAPORATION RESIDUES

All E.R. measurements were performed in a 51 cm. diameter scattering chamber. A cross sectional view of the experimental set up is shown in fig. 3.7.

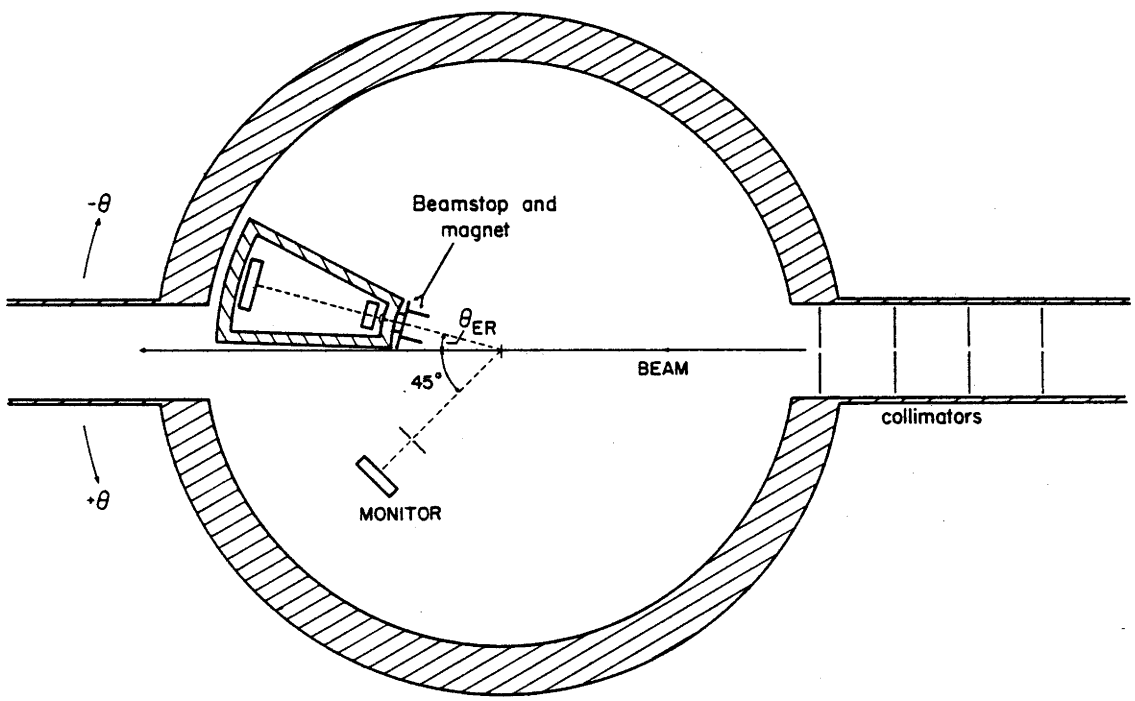

Fig. 3.7 Detector arrangement in the 51 cm. scattering chamber for evaporation residues measurements.

The 90 mm. time of flight detector telescope, described in section 3.3, was mounted on the outermost turntable leaving about 12 cm. between the target and the detector. At such a short distance beam-spot movements on the target contribute considerably to detector angle uncertainty. This is most undesirable because the E.R. cross section changes strongly with angle. To limit this effect 1mm. wide strip targets were used in all experiments. Another uncertainty in the detector angle is introduced by the accuracy with which the detector can be aligned with the turntable angle marker. The deviation ($\Delta\theta$) from the nominal angle was calculated from elastic scattering yields, measured in both the telescope and a monitor detector at 30°. Since the elastic scattering is pure Rutherford at forward angles the quantity :

$$\frac{N_{tel}}{N_{mon}} \frac{1}{\sigma_{Ruth}(\theta+\Delta\theta)} \qquad \text{is constant}$$

where θ is the turntable angle; N_{tel} and N_{mon} are elastic yields in respectively the telescope and the monitor counter. N_{tel}/N_{mon} was measured for a number of angles $|\theta|>6^\circ$ on both sides of the beam axis. At these angles the elastic scattering from the target and the carbon backing material could be resolved. The offset angle $\Delta\theta$ was found by adjustment until the best agreement with a constant value was obtained. It was found that $|\Delta\theta| < 0.15^\circ$ in all experiments.

As mentioned in section 1.2, the time of flight between the target and the E-counter was measured with the RF-signal from the pulsed beam facility. With this method a complication in the identification of E.R. arose because beam particles scattered off the beam-line collimators happened to have the same T_{RF-E} as E.R. This was possible because the beam particles slowed down in scattering from the beam-line collimator and arrived later at the target than non slit-scattered particles. This delay compensated for the longer time the E.R. took to travel from the target to the E-counter. This effect could easily be avoided by changing the position of the beamline collimators. Evaporation residues were measured over an angular range from 2 to 15 degrees on both sides of the beam axis. To reduce systematic errors due to beamspot movement an alternate sequence of angles was measured at. (typically -2,+3,-4,+5 etc.).

Evaporation residue cross-sections were measured for three tungsten and two hafnium isotopes to investigate the influence of the hexadecapole moment on the sub-barrier fusion cross-sections. In comparing σ_{fus} for the different isotopes it was

important to measure under identical experimental conditions. Therefore E.R. were measured for all isotopes during one experiment. The targets were mounted on a target-ladder, which enabled subsequent measurement of isotopes for identical detector angles.

ELECTRONICS. The pre-amplifiers and the fast timing circuitry for all detectors were located near the scattering chamber to limit noise and pick-up as much as possible. The rest of the signal processing was done in the control room. The electronic scheme employed is displayed in figure 3.8.

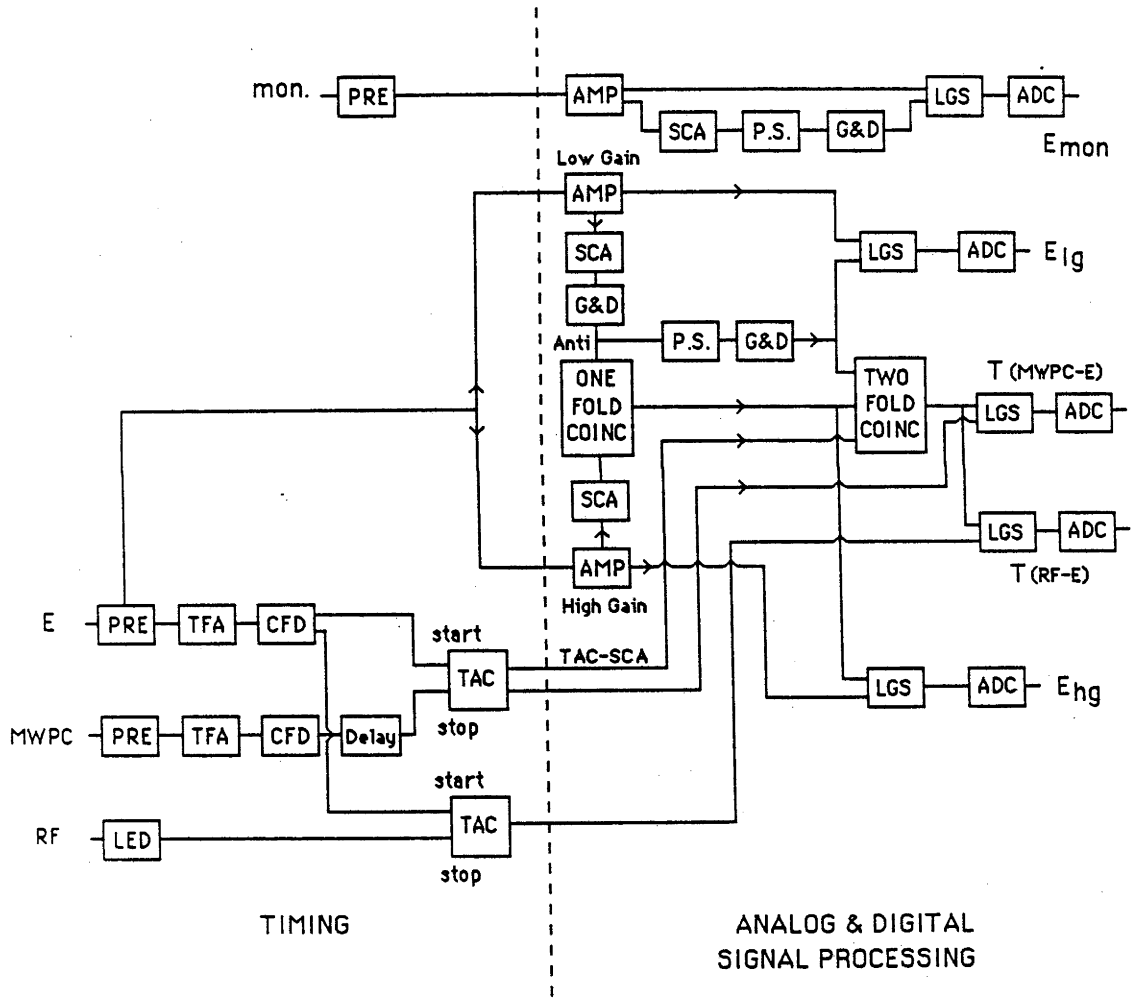

Fig. 3.8 Electronics scheme employed in the evaporation residue measurements. For explanation see text. Electronic units are identified in Table 3.1.

To record the energy of the E.R. and the elastic events simultaneously the E-signal is split up in a high- and low gain branch. The amplification factor of the two amplifiers differs by about a factor 10 covering a wide range of energies. At very small angles the rate in the low-gain branch was scaled down to avoid excessive dead time in the ADC and computer. The high gain, scaled-down low-gain energy signals, as well as the time of flight signals T_{RF-E} and T_{MWPC-E}, were recorded in coincidence mode. The monitor energy-signal was recorded in singles mode. All gate signals were counted with scalers for dead-time correction. Rates in the ΔE and E counters were continuously monitored and kept below 2000 counts per second. Absolute partial cross sections were obtained by comparing E.R. yields in the telescope with elastic yields in the monitor detector at 30° :

$$\frac{\partial\sigma_{ER}}{\partial\Omega}(\theta) = \frac{N_{ER}}{N_{mon}} \frac{\Omega_{mon}}{\Omega_{tel}} \frac{\partial\sigma_{Ruth}}{\partial\Omega}(30°) = \frac{N_{ER}}{N_{mon}} A \qquad (3.4.1)$$

The factor A containing the solid angle ratio between monitor and telescope detectors was obtained from elastic scattering in both detectors.

3.4.4 FISSION FRAGMENTS

Fission fragment measurements were performed in a 51 cm. diameter scattering chamber with the detection technique described in section 3.3.4. A cross sectional view of the experimental set-up employed in the fission cross section measurements for the systems $^{159}Tb+^{19}F$; $^{169}Tm+^{19}F$; $^{181}Ta+^{19}F$; $^{139}La+^{19}F$ and $^{150}Sm+^{18}O$ is shown in fig. 3.9. The E-ΔE telescope operated at 25 Torr. gas pressure was positioned at +60° which required a complementary detector angle of 100°. This detector angle only needed slight adjustment for different systems. A 1 mm. diameter aperture was used in front of the telescope subtending a solid angle of 50 μsr. The 100° detector was located at 28 mm. from the target to cover the whole angular range of complementary fragments. Because of this small distance electrons, knocked out of the target by beam particles, gave rise to high electron count rates. This detector noise was reduced with a 750 $\mu g/cm^2$ gold foil placed in front of the detector. Fission fragments lose about 10 MeV. in the foil, which did not noticably affect the coincidence rate.

During the $^{124}Sn+^{58}Ni$ measurements the detector telescope was positioned at +45° and the complementary detector at -60°. In this experiment nickel ions were stripped to the

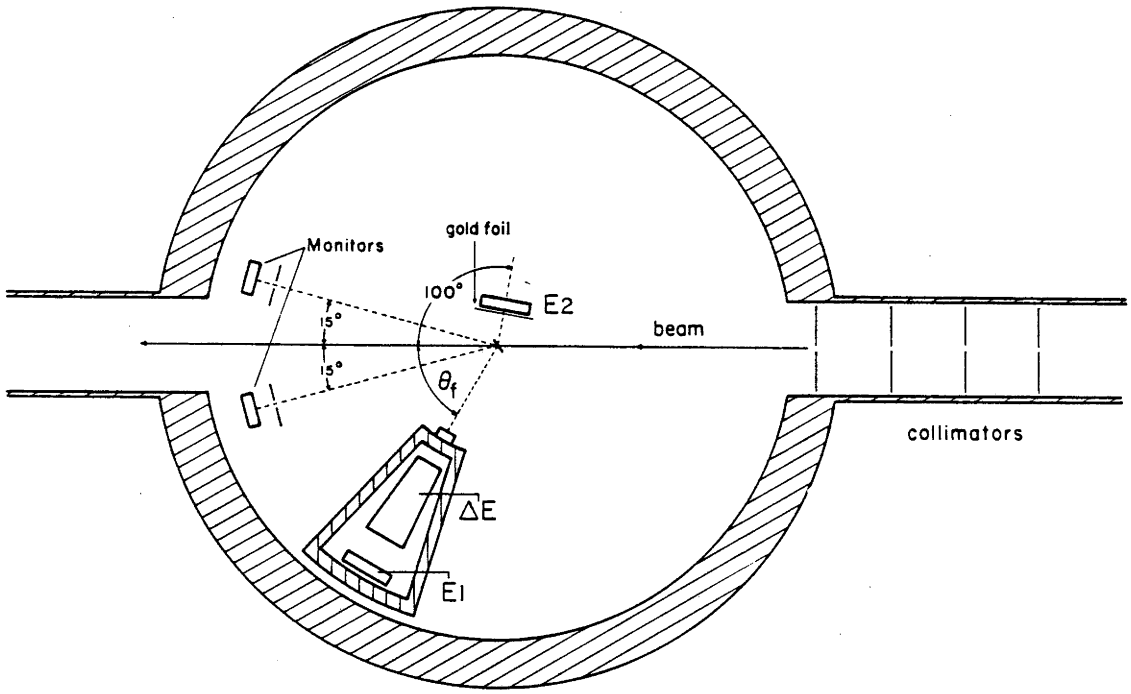

Fig. 3.9 Detector arrangement in the 51 cm. scattering chamber for the fission fragment measurements.

19^+ charge state with double stripping. Different combinations in the number of electrons stripped in the first and second stripper foils caused the creation of several particle-beams with nearby energies. Due to a slight drift in the terminal voltage or after recovery from a voltage break-down in the accelerator the machine may stabilize on a different beam. To select the right beam energy calibrated monitors were used to measure the energy of elastically scattered particles. Throughout the experiment the monitor spectra were displayed so any change in beam-energy could be noticed immediately. The monitors at nominal angles +15° and -15° were also used for normalisation and absolute cross-section determination. The absolute angles of the two monitor detectors were derived from elastic scattering measurements in the same way as described for the nine angle detector (section 4.1).

ELECTRONICS. As in all other experiments the pre-amplifiers and electronics for fast timing were located near the scattering chamber. The amplified signals were sent over to the control room to be further processed. The electronic arrangement used during the fission experiments is shown in fig. 3.10.

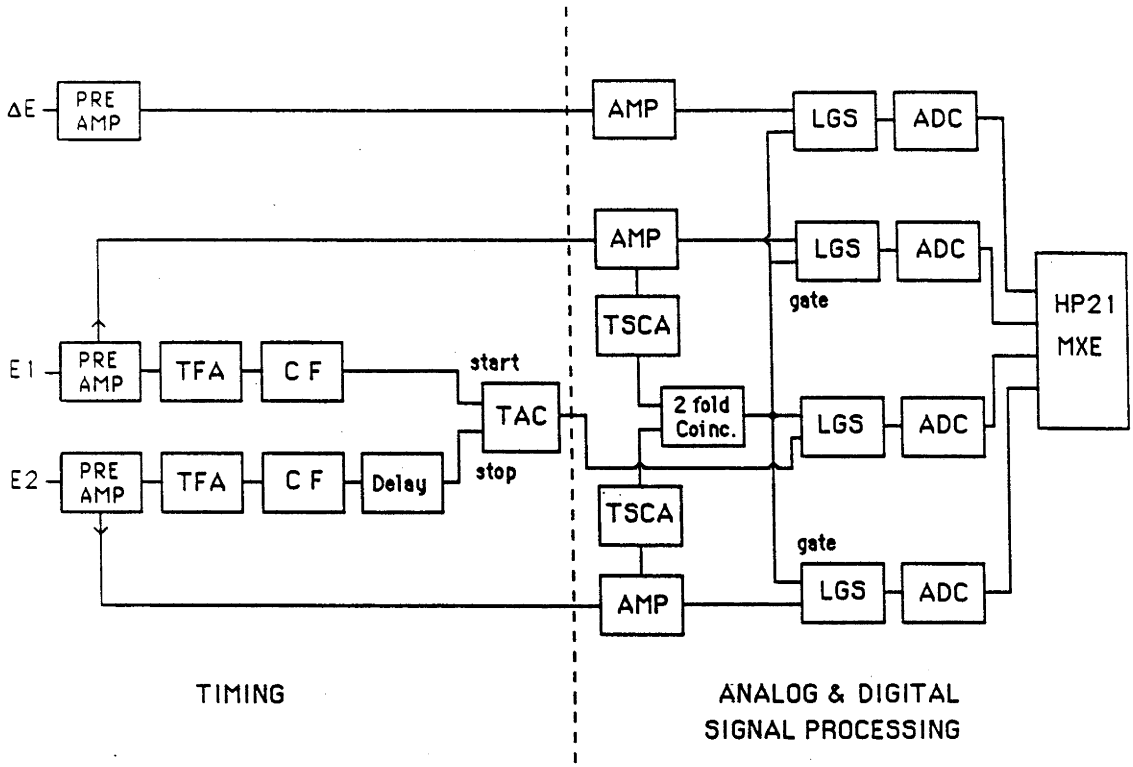

Fig. 3.10 Electronics scheme employed in the fission fragments measurements. Electronic units are identified in table 3.1

3.4.5 GAMMA RAY MULTIPLICITY MEASUREMENTS

Gamma-ray multiplicities were measured from the decay of ^{178}W, formed in the fusion reaction ^{159}Tb+^{19}F at 80,85,90 and 100 MeV energies. The multiplicity filter used, consisted of 6 NaI (5.08 cm diameter x 5.08 cm long) crystals, which were positioned around the beampipe, as illustrated in the schematic lay-out of fig 3.11. A high energy-resolution Ge-detector was used to select (off-line) complete fusion events. The multiplicity filter was strobed by gamma-rays from the Ge-detector. Off-line the gamma-ray multiplicities for different $^{(178-xn)}$W nuclei could then be determined by setting windows on the photopeaks of the appropriate characteristic transitions.

A number of precautions were taken to ensure reliable determination of the multiplicities :

1) Along with gamma-rays also neutrons are detected by the NaI-array. To be able to correct for this the ratio of gamma-rays to neutrons was measured with a large NaI crystal

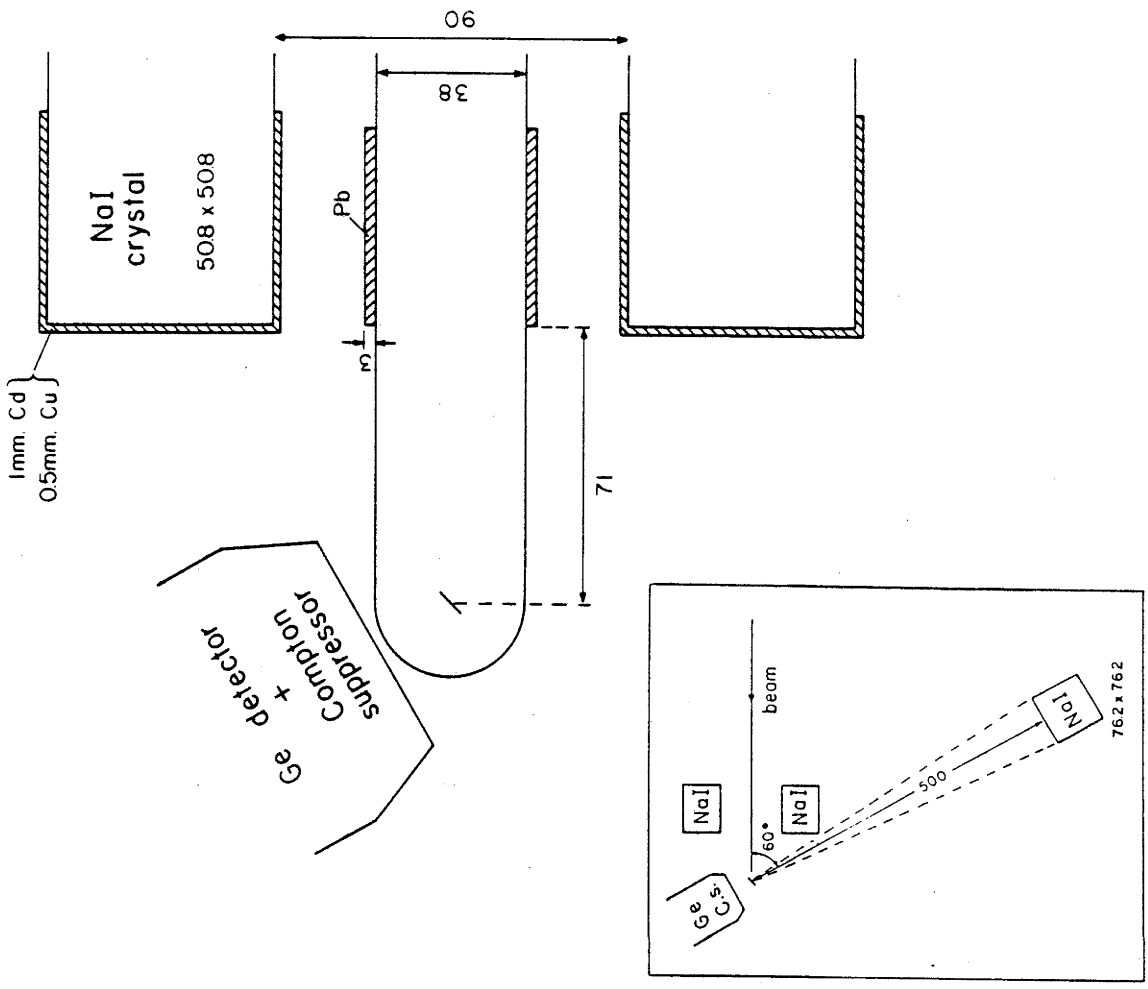

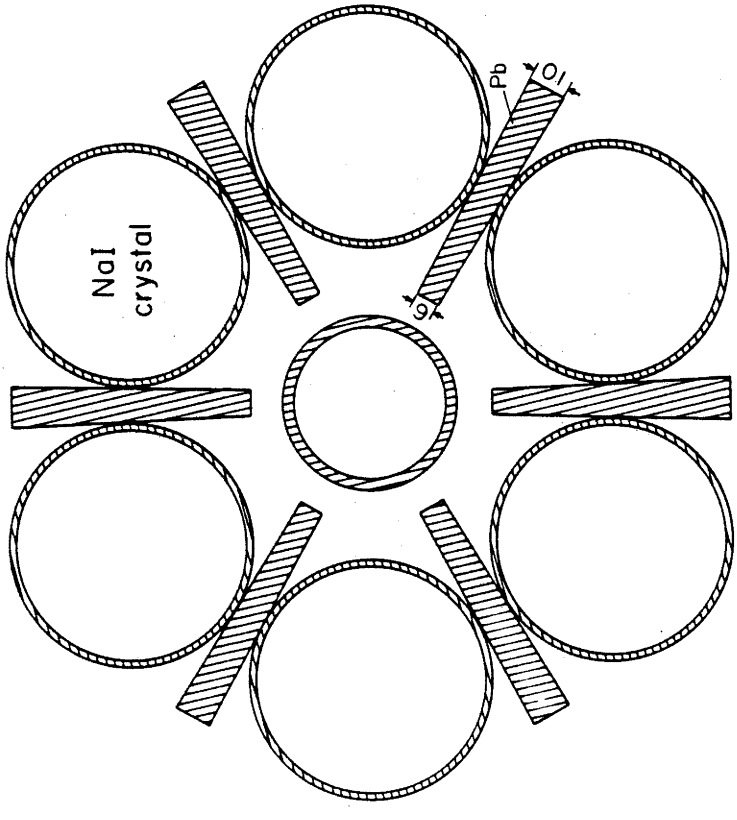

Fig. 3.11 Schematic diagram of the 6 NaI detectors configuration and its shielding. The insert shows the detector arrangement during the gamma-ray multiplicity measurements.

(7.26 cm diameter x 7.26 cm long), positioned at 50 cm from the target. The neutrons were identified by measuring the time difference between signals in the Ge-detector and the 7.26 cm NaI detector.

2) Compton scattering of high-energy gamma-rays in the Ge-detector produces a background underneath the photopeaks of interest. To reduce this background a Compton suppressor, a large NaI crystal surrounding the Ge-detector, was used; pulses from it vetoed pulses from the Ge-detector.

3) Gamma-rays emitted from the recoiling compound nucleus are Doppler shifted and broadened, which affects the energy-resolution. To minimize this, a lead backing was attached to the 900 $\mu g/cm^2$ rolled ^{159}Tb target to stop the recoiled compound nuclei.

4) A gamma-ray detected in one of the 6 NaI detectors may have Compton scattered and escaped from it to produce another signal in a neighboring detector. This would result in increased values of the multiplicities. To minimize cross-talk, lead absorbers were placed in-between adjacent detectors and around the beam-pipe as shown in fig. 3.11.

5) The x-rays produced in the target and in the lead-absorbers were absorbed by layers of 0.5 mm Cu and 1 mm Cd surrounding the NaI detectors. The copper was placed behind the cadmium to absorb the cadmium x-rays. Gamma-rays produced by the photo-electric effect in the copper shield are lower in energy than from lead or cadmium and could be absorbed by the aluminum, surrounding the detector crystal.

ELECTRONICS. Figure 3.12 shows the electronic scheme employed in the on-line data processing. Signals from the multiplicity array were fed into a fast multiplicity box, which was strobed by a signal derived from coincidences between all array pulses and the Ge pulses; the timing of the strobe pulses was determined from the NaI signals. The multiplicity box provided pulses whose heights were proportional to the number (fold) of NaI detectors, which were in coincidence with the Ge-detector.

Five parameters were recorded event-by-event on magnetic tape. These were : the Ge energy-signals in coincidence with pulses from the array plus the 7.62 cm NaI-detector; the fold-signal; the Ge/ΣNaI time to amplitude converted (TAC) signal; the Ge/7.62cm NaI TAC-signal and the 7.62 cm NaI energy signal.

In order to reduce dead-time in the event-by-event mode, the 1-fold events were scaled down by a factor of ten. In addition the signals, 0-fold,1-fold and 2-fold Ge-spectra were accumulated in singles mode and these, together with the true coincidences, were scaled so that dead-times could be determined. They were normally less than 5% and the relative dead-times between folds, the important quantities in the analysis, considerably less.

The efficiencies of the multiplicity array and of the 7.62 cm NaI-detector were determined from coincidence measurements with the Ge-detector of gamma-rays from

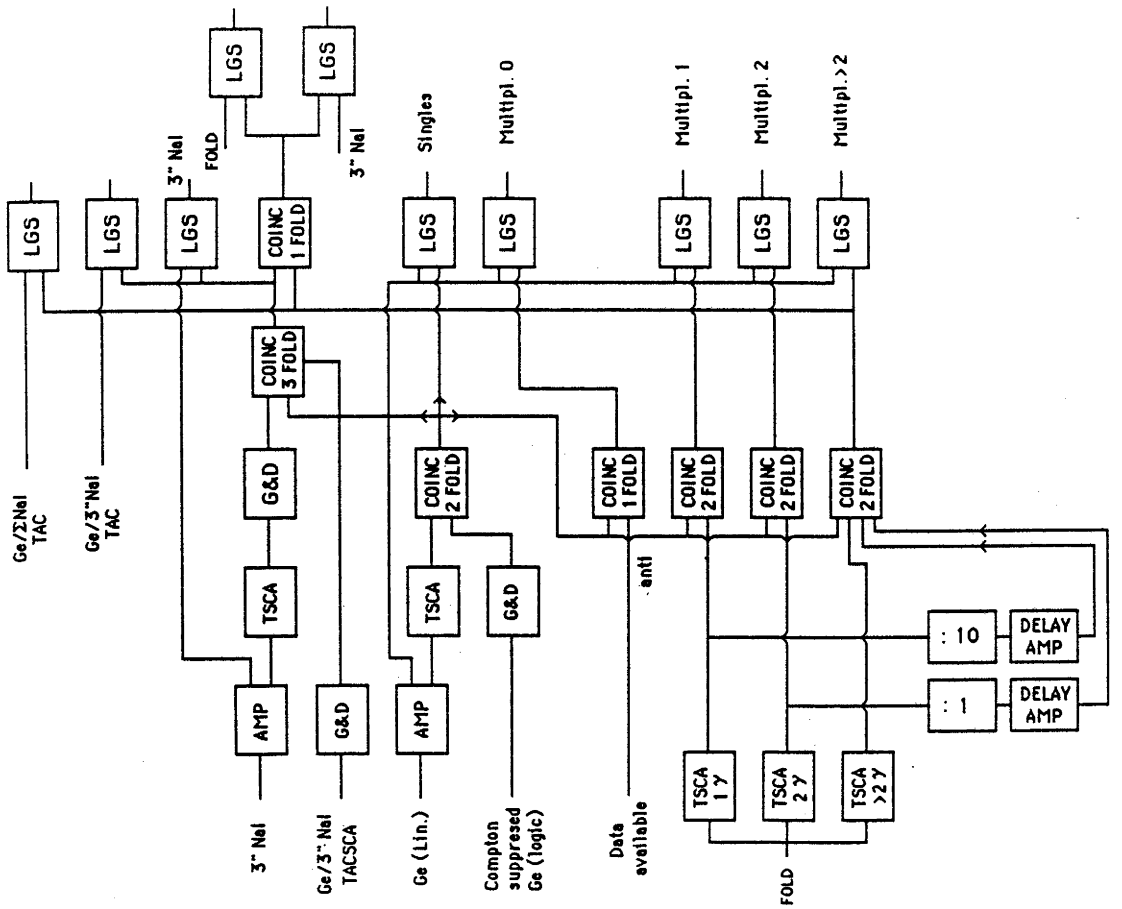

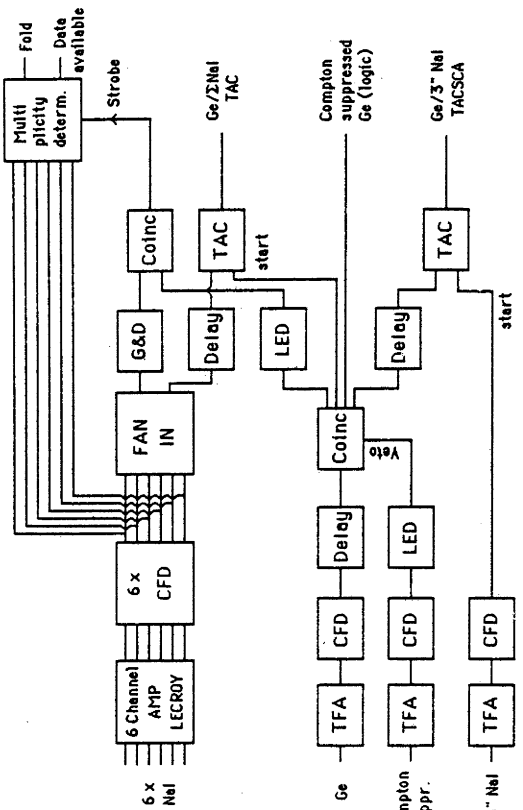

Fig. 3.12 Electronic scheme employed in the gamma-ray multiplicity measurements. Explanation given in text. Electronic units are identified in Table 3.1.

sources ^{152}Eu,^{207}Bi and ^{60}Co, mounted in the target position. The measurements also showed that the effect of scattering between the detectors had a negligible effect on the determination of multiplicity fold-distributions.

3.5 ACCELERATOR BEAMS AND TARGETS

In this section a brief description of the accelerator the beam bunching system and beam-line equipment as well as details about exprimental targets will be given.

3.5.1 14 UD ACCELERATOR

The heavy-ion accelerator of the A.N.U. is a N.E.C. 14-UD vertical tandem pelletron [Tro74]. It consists of a 22 m long 5.5 m diameter pressure vessel containing the accelerator tube surrounded by a support column made up of 28 1MV. modules [Her74]. The terminal potential is maintained by a charging system consisting of rotating chains of metal pellets joined by links of insulating material. The electrostatic potential is graded along the column using corona current across point to plane gaps, and a uniform field is maintained by evenly spaced metal rings round the column, which are electrically connected to the corona points. For optimum insulation the pressure vessel is filled with sulfur hexafluoride gas SF_6.

Heavy ions are accelerated in two stages. Firstly negative ions, produced in a ceasium sputter ion source, are inflected into the machine at ~150 kV and accelerated to the high voltage terminal halfway down through the tube. The ions pass through a carbon stripper foil losing several or all of their electrons and are subsequently accelerated to ground potential. The energy gained is :

$$E = (Q+1)\,TV \qquad (MeV) \qquad (3.5.1)$$

where Q is the charge state of the ion after stripping and TV is the terminal voltage. A second stripper located at a position equivalent to 2/3 of the terminal potential can be made operational if higher energies are required. The fully accelerated beam is energy and charge state analyzed with a 90° product $MEQ^{-2} = 200$ analyzing magnet before it reaches a switching magnet, which steers the beam into one of seven available beamlines. At various points along the machine and beam-lines there are bending and focussing magnets to optimize beam transport.

3.5.2 PULSED BEAMS

The pulsed beam facility of the 14-UD consists of a pre-tandem, room-temperature buncher, two choppers and a super-conducting post-tandem buncher. Room temperature bunching is achieved with a 9.375 MHz sine wave across two parallel wire planes.

Ions cross the wire planes at energies of typically 150 keV, which for ^{16}O means a velocity of 1.3 mm/ns . Because the gap between the grids is of the order 1 mm. the ions effectively experience a constant field between the grids. Within time interval (t_0,t_1) (fig. 3.13) the later arriving ions experience a higher accelerating field causing the formation of bunches, which narrow as time progresses. By adjusting the buncher field strength the time focal point can be positioned at the experimental target. The background of particles between the bunches is removed with two choppers. One chopper, consisting of two parallel deflection plates in front of a slit, operates at half the buncher frequency. The relative phases are chosen such that the bunches pass through the chopper at the nodes of the sine wave. Particles between the bunches are removed from the beam by deflection on to the slits. This chopper leaves a 6.6 ns. window round the bunches. Another chopper,

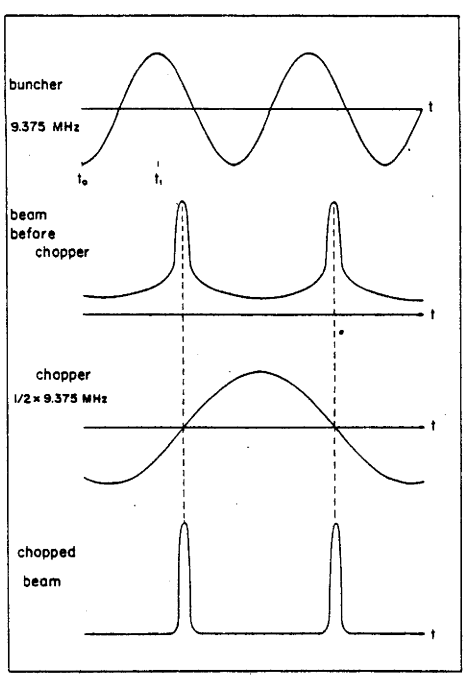

Fig. 3.13 Schematic diagram of the operation of beam-bunching.

with four times the bunching frequency, cuts off the tails of the bunched beam by providing a 2 ns. wide window. The higher frequency provides a steeper slope at the

nodes, which results in a more sharply defined time interval. In the experiments, described here, the super-buncher was not used. With the room temperature buncher a time resolution < 1 ns. could readily be achieved for ^{19}F and ^{18}O ions.

3.5.3 VACUUM SYSTEM

Good vacuum during all experiments was achieved with a system designed at the ANU [Oph74a],[Oph74b]. The scattering chamber and part of the beamline were pumped from atmospheric pressure to about 5 10^{-7} Torr. in two stages. During the first stage a rotary carbon vane pump reduced the pressure to ~100 Torr. after which a Varian vacsorb, operating with zeolite at liquid nitrogen temperature, brought the pressure down to $<10^{-2}$ Torr. For the 51 cm. diameter scattering chamber this rough pumping stage took 30 to 45 minutes depending on the outgassing rate in the chamber. In the second stage cryogenic and ion pumps (getter/sublimer and sputter pumps) were used to obtain high vacuum. The cryogenic pump works like a cold trap which removes condensable vapours from the system. Liquid helium is used as coolant. The cryopump was used as an intermediate system between roughing and final ion pumping.

Getter/sublimer pumps use vapourized titanium from an indirectly heated cathode to chemically combine (gettering) with gas molecules like oxygen, nitrogen and carbon dioxide. Non chemically active gases like helium and argon are reduced with sputtering. Gas molecules are ionised by electrons moving in an applied electric field. The gas ions accelerate to the cathode, where impact causes sputtering of the cathode material, titanium. The sputtered titanium either chemically combines with the ions or buries them. To enhance the ionisation efficiency a magnetic field is applied, which causes the electrons to spiral, increasing the electrons path length considerably.

Good vacuum could be achieved and maintained by thoroughly cleaning of all detector components and avoiding the use of materials with bad outgasing properties. One advantage of a low outgasing rate was that no gas flow system was required for the ionisation chambers.

3.5.4 TARGETS AND DETECTOR-WINDOWS

Thin film-targets were produced by the vacuum evaporation technique. Target materials were evaporated by heating and subsequently condensed on masked (strip form) carbon substrates. Samarium, terbium and thulium materials have low enough evaporation temperatures to be resistance heated, but tantalum had to be evaporated by electron

bombardment. Samarium in oxide form Sm_2O_3 was first reduced with a lanthanum reaction agent before being evaporated. Growth of the condensed layer was monitored with a quartz crystal. The frequency of the crystal changes as vapour gets deposited on its surface. Knowledge of the directional dependence of evaporation allows determination of the layer thickness on the carbon substrate. The mass deposited on the crystal can be measured to better than 1 μg. accuracy. However, accuracy in the thickness depends mainly on the uniformity, which is largly determined by the condition of the substrate surface and the sticking factor of the evaporated material. The estimated accuracy of the target thickness is 10 %.

Hafnium and tungsten have melting points of 2227 °C and 3410 °C respectively. Targets of these materials were therefore not produced with the evaporation technique but were prepared with a fine beam saddle-field ion-source. The ion-source consisted of a doughnut-shaped anode kept at 5 kV. potential and enclosed in a cylindrical cathode at ground potential. The electric field between the doughnut and the cylinder caused electrons to describe multiple loops through the centre of the doughnut. This increased the probablity of ionisation of gas molecules (argon) near the axis of the doughnut. Argon ions produced at the axis experience a repulsive force along the axis and leave the cylinder through a 1 mm. diameter aperture. The positive argon ion beam was used to sputter W and HfO_2 onto a carbon substrate. The targets so produced for the E.R. measurements were typically 40 $\mu g/cm^2$ thick.

The E.R. and fission fragment cross-sections change rapidly at energies near and below the Coulomb barrier. It is therefore essential to have a well defined beam energy. The uncertainty in the particle energy at the moment of nuclear interaction is determined by the accuracy in beam energy of the accelerator and the energy loss in the target prior to nuclear interaction. The accelerator beam energy-spread is less than 0.1 %, which for 80 MeV. ^{19}F means 80 keV. In chosing the target thickness one has to compromise between energy resolution and count rate. As an example the measurement of 1 mb/sr. cross-section with a 100 nA ^{19}F (9^+) beam current on a 100 $\mu g/cm^2$ ^{159}Tb target with a detector solid-angle of 100 μsr. gives a count rate of 10 counts per hour. The energy-loss of 80 MeV ^{19}F-ions in the same target is ~250 keV. The thickness of target, used in various experiments, are given in table 3.2. Table 3.3 gives the isotopic compositions.

In most of the experiments formvar windows were used to confine isobutane ionisation-gas to the detector. The windows were made from a 5-10% solution of formvar in chloroform. A microscope slide was immersed in the solution and the fluid was drained away with the slide in vertical position. A film of formvar, the thickness of which depends on the rate of flow and the concentration of the solution was left on the slide. The film was

then floated off in distilled water and inspected in thickness by observing the optical interference colour in reflection. From comparison with a set of calibrated formvar films the thickness was estimated. The film is attached to the stainless steel window holder using the formvar solution as glue. A vacuum test chamber was used to check for larger leaks while minute leaks were spotted in the scattering chamber. The ion pump current gauge provided a most sensitive leak testing device.

TABLES

Table 3.1 Explanation of symbols used in electronic diagrams.

ADC	Canberra 8060 Analogue to Digital Converter.
Amp	Tennelec 203 BLR Linear Amplifier.
CFD	Ortec 473A Constant Fraction Discriminator.
Coinc	Canberra 1446 Coincidence unit.
Delay	Ortec 425 Nanosecond delay.
Delay Amp	Canberra 1457 Delay Amplifier.
FAN	Le Croy fast FAN in/out.
G&D	Ortec 416A Gate and Delay generator.
LED	Le Croy 821 Leading Edge Discrimination.
LGS	Canberra 1454 Linear Gate and Stretcher.
Logic shaper	Canberra 1455A Logic shaper and delay.
PRE	Ortec 125 or 142B Pre-amplifiers.
PS	ANU pre-scaler.
SCA	Canberra 1437 Timing Single Channel Analyser.
Sum Amp	ANU Sum Amplifier.
TAC	Canberra 1443 Time to Amplitude Converter.
TFA	Ortec 454 Timing Filter Amplifier.
TSCA	same as SCA.
6xAMP	Le Croy 612A Fast Amplifiers.
6xCFD	Le Croy 821 Constant Fraction Discriminators.

Table 3.2 Thicknesses of targets ($\mu g/cm^2$), used in various measurements.Targets used in the elastic scattering measurement were in the forms of 2mm. wide strips on carbon backings of ~30$\mu g/cm^2$. For the E.R. and fision fragment measurements 1mm. strips were used on ~15$\mu g/cm^2$ carbon backings.

NUCLEUS	ELASTIC SCATTERING	EVAP. RESIDUES	FISSION FRAGMENTS	GAMMA MULTIPLICITY
^{124}Sn			230[1]	
^{139}La	100		150	
^{150}Sm	150/30[2]	30	100	
^{159}Tb	100	200		900[3]
^{169}Tm	150	50	100	
^{181}Ta	100		150	
$^{182,184,186}W$		40		
$^{176,180}Hf$		40	40	

1) Full area, self supporting.
2) In the high energy-resolution measurements with the Enge-spectrograph the target thickness was 30.
3) Rolled target with lead backing.

Table 3.3 Isotopic composition of the target materials used.

TARGET	ISOTOPIC COMPOSITION
^{124}Sn	^{124}Sn (96.96%);^{122}Sn (1.04%)^{120}Sn (0.94%);^{118}Sn (0.41%)
^{139}La	^{139}La(100%)
^{150}Sm	^{150}Sm (95.5%);^{149}Sm (1.7%);^{152}Sm (1.5%); ^{154}Sm (0.5%)
^{159}Tb	^{159}Tb (100%)
^{169}Tm	^{169}Tm (100%)
^{181}Ta	^{181}Ta (100%)
^{182}W	^{182}W (98.2%)
^{184}W	^{184}W (95.1%)
^{186}W	^{186}W (97.1%)
^{180}Hf	^{180}Hf (98.2%)
^{176}Hf	^{176}Hf (77.5%);^{177}Hf (11.4%);^{178}Hf (5.8%); ^{179}Hf (2%)

CHAPTER 4
DATA REDUCTION & RESULTS

The results of elastic scattering, evaporation residue, fission fragment, and gamma-ray multiplicitiy measurements will be discussed in this chapter. Table 4.1 indicates the measurements which have been performed for each reaction.

TABLE 4.1

SYSTEMS	ELASTIC SCATTERING	EVAPORATION RESIDUES	FISSION FRAGMENTS	GAMMA-RAY MULTIPLICITY
$^{18}O+^{150}Sm$	√*	√	√	
$^{19}F+^{139}La$	√		√	
$^{19}F+^{159}Tb$	√	√	√	√
$^{19}F+^{169}Tm$	√	√	√	
$^{19}F+^{181}Ta$	√		√	
$^{16}O+^{182,184,186}W$		√		
$^{16}O+^{176,180}Hf$		√	√	
$^{58}Ni+^{124}Sn$			√	

*) High resolution measurements as well as E-ΔE generalized-elastic measurements were done for this system.

4.1 ELASTIC SCATTERING AND PARTICLE TRANSFER

In this section the results will be presented of the elastic scattering experiments, which were performed with an E-ΔE particle detector-telescope for the systems $^{139}La,^{159}Tb,^{169}Tm,^{181}Ta+^{19}F,^{150}Sm+^{18}O$ and also with the Enge magnetic spectrograph for the scattering of ^{18}O from ^{150}Sm as well. Elastic scattering, measured with the E-ΔE detection technique contains inelastic scattering (to about 1 MeV.) and will be called generalized-elastic in the following.

4.1.1 GENERALIZED-ELASTIC SCATTERING AND CHARGED PARTICLE TRANSFER

IDENTIFICATION

The identification of reaction-products is illustrated in figure 4.1. It shows the reaction products measured at 60° for the scattering of 90 MeV ^{19}F-ions from ^{181}Ta.

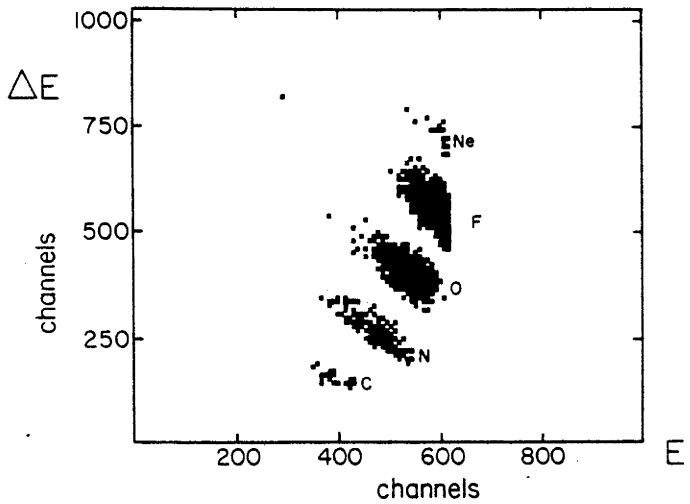

Fig. 4.1 Charge separation with the E-ΔE detection technique for the reaction ^{181}Ta+^{19}F at 90 MeV. Each group contains different isotopes.

The groups indicated by O(xygen),N(itrogen) and C(arbon) result from respectively 1,2 and 3 proton transfer reactions. They produce progressively smaller signals in the ΔE gas-detector because of their lower charge. The less intense group of events with ΔE-signals larger than the F(luorine) group result from one proton pick-up reactions. It should be noted that mass identification is not performed thus each group may contain contributions from several masses.

Energy-spectra associated with generalized-elastic scattering were obtained by sorting the events on magnetic tape with software contour gates in the E-ΔE spectra. The spectra were calibrated using elastic peak positions, measured at different angles, in reaction kinematics calculations. The energy resolution for each detector-telescope was determined from the width at half maximum of the elastic peak, measured at the most forward angles. A typical value of 600 KeV was found, which is the sum of contributions from energy-straggling in the target, detector-window and detector-gas as well as from the resolution of the solid state detector.

For all systems measured, the first excited states of the nuclei are less than 400 KeV. Thus some of the inelastic scattering events are not resolved from the the elastics. Most of the neutron transfer-products could be resolved except for 2n pick-up for the reactions ^{159}Tb,^{169}Tm and ^{181}Ta+^{19}F. In heavy ion scattering the particle transfer yields are strongly dependent on the kinematics of the reaction [But71]. At energies just above and below the Coulomb-barrier the optimum Q-values for neutron stripping or pick-up is

Q=0, which may be interpreted in terms of matching the Rutherford orbits in the entrance and exit channels. For neutron transfer reactions with large negative Q-values the cross-sections will be much reduced. In table 4.2 the ground-state Q-values are shown for neutron pick-up and stripping reactions for the systems under study.

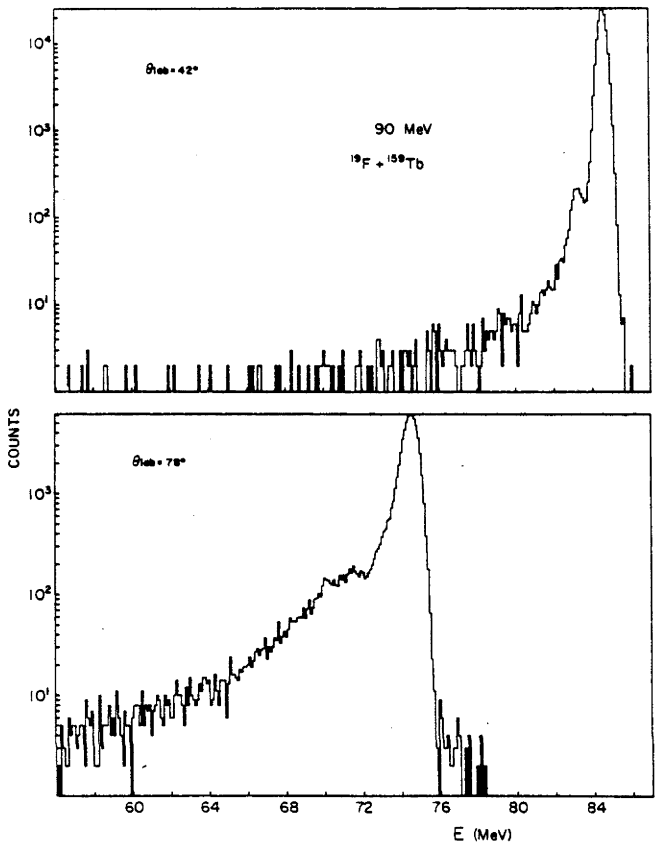

Fig. 4.2 Fluorine energy spectra from the reaction $^{159}Tb+^{19}F$ at 90 MeV. The lower spectrum, which was measured near the grazing angle, shows an increased yield near the energy where 1n pick-up reaction products are expected.

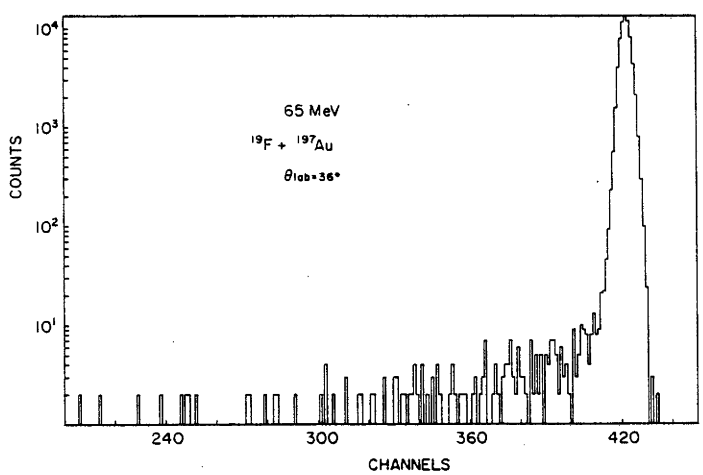

Fig. 4.3 Sub Coulomb-barrier scattering of ^{19}F from ^{197}Au, measured with the same detector as was used for the spectra of fig. 4.2. It shows that the structure observed in fig. 4.2 is not due to detector response.

Table 4.2 Ground-state Q-values in MeV.

Systems	1n p.u.	2n p.u.	1n str.	2n str.
$^{19}F+^{139}La$	-2.2	-2.5	-5.3	-7.7
$^{19}F+^{159}Tb$	-1.5	-0.2	-4.1	-5.5
$^{19}F+^{169}Tm$	-1.4	-0.2	-3.8	-5.5
$^{19}F+^{181}Ta$	-1.0	+0.5	-4.4	-6.6
$^{18}O+^{150}Sm$	-4.0	-2.3	-2.5	+1.7

It shows that the two neutron pick-up reaction for the systems ^{159}Tb, ^{169}Tm, $^{181}Ta+ ^{19}F$ have Q-values closest to zero. Figure 4.2 shows the fluorine energy spectra from the reaction $^{159}Tb+^{19}F$, measured at a forward angle (42°) and measured near the grazing angle (78°). An increase in relative yield in the 78° measurement can be observed near the energy where products from one neutron pick-up reactions are expected. To show that the observed structure is not an artefact of the detector, the elastic scattering energy spectrum of ^{19}F from a thin gold target is shown in fig 4.3. It has been shown [Boc70],[Dub71] that cross-sections for successive nucleon transfer reduces by a factor 3 to 10. Hence from the 1n pick-up yields shown in figure 4.2, the unresolved 2n pick-up yields were estimated to be less than 2% of the generalized-elastic yields. To check this, neutron transfer and pick-up reaction-products have been measured from the reaction $^{159}Tb + ^{19}F$ with the ANU Enge magnetic-spectrograph. The different reaction products were identified with ΔE, E and position information from the focal-plane detector, described in section (3.3.2).

Measurements were made for angles θ_{cm} from 60° to 95°. It was found that for E_{beam} =90 MeV the 2n pick-up yields were less than 0.5% of the sum of elastic and inelastic yields. At 100 MeV they are less than 1.5%. Furthermore it was found that the ratio 1n/2n pick-up is 5 and 9 for 90 and 100 MeV beam-energies respectively. In [Sob86] a ratio of 8 was found for the same system at 181 MeV. beam energy. From observed 1n pick-up yields for ^{19}F-ion scattering from ^{169}Tm and ^{181}Ta and assuming the same 1n/2n ratios as for ^{159}Tb similar percentages were found for these systems. Thus the generalized-elastic yields are virtually free from particle transfer products.

Figure 4.4 shows the energy spectra of the fluorine, oxygen, nitrogen and carbon ejectiles from the reaction $^{159}Tb+^{19}F$ at 90 MeV energy. The distributions are continuous and extend over a wide energy range, indicating a high density of particle states.

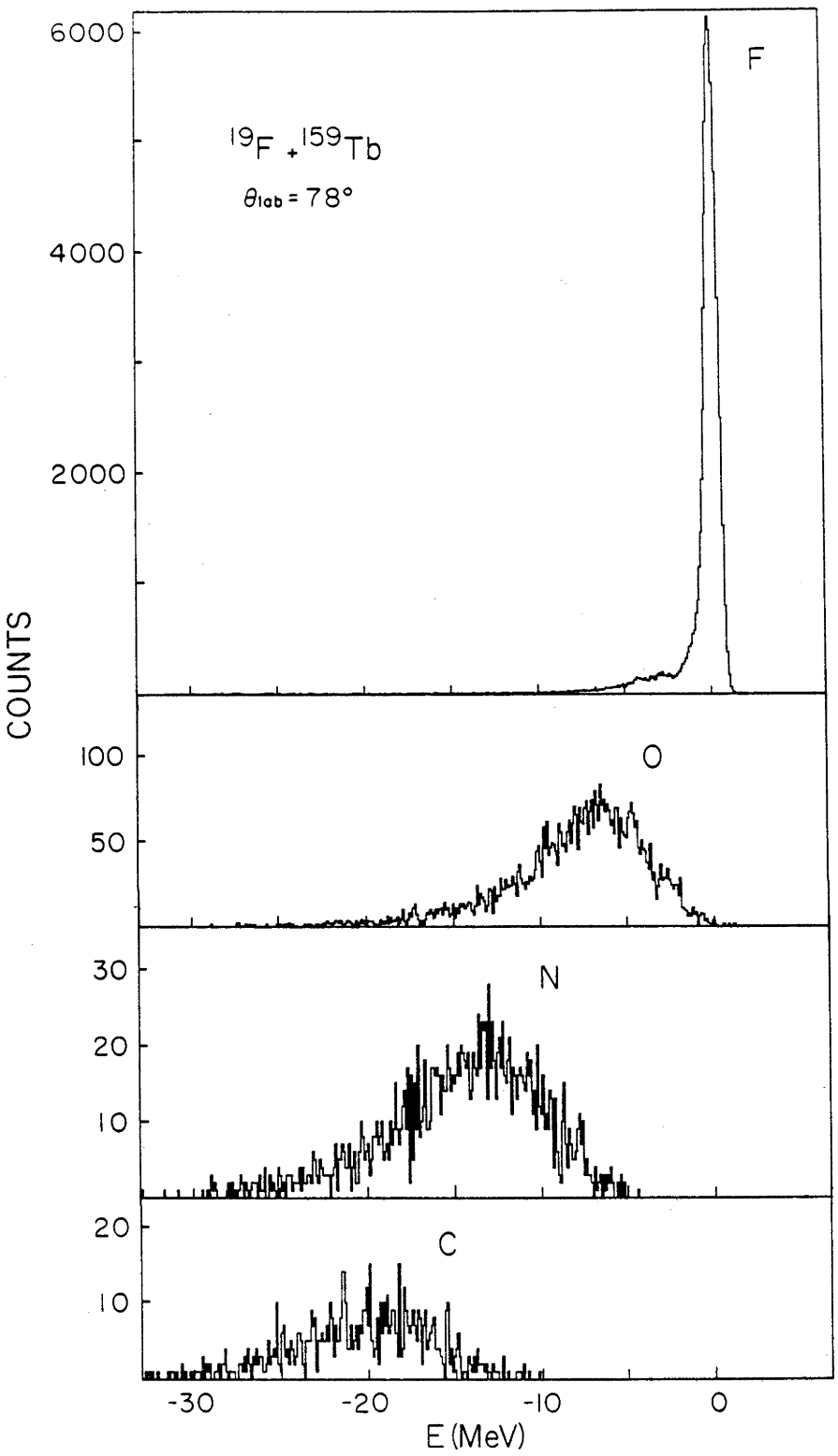

Fig. 4.4 Energy-spectra of the fluorine, oxygen, nitrogen and carbon ions from the reaction $^{159}Tb+^{19}F$ at 90 MeV.

CALIBRATION AND NORMALISATION

The angles and solid angles of each of the eight detector telescopes used, were measured with elastic scattering of ^{19}F-ions from ^{197}Au at 65 MeV beam energy, which is about 20 Mev below the Coulomb-barrier. Elastic cross-section ratios were determined for each detector-telescope by measuring elastic yields with the detector-arm positioned at 60° and 96° nominal angles. For each detector the experimental ratio $d\sigma_{el}(\theta)/d\sigma_{el}(\theta+36)$ was compared with the Rutherford cross-section ratio for the same 36° difference in angle. The detector-telescope angle is then determined by θ for which the Rutherford ratio was equal to the measured ratio. Figure 4.5 shows the result of this procedure. The difference in angle $\Delta\theta$ between the measured and nominal design-values is consistent with $\Delta\theta=0$ within statistical accuracy. Solid angles were calculated from the same elastic data and expressed as ratios to the solid angle of telescope number 2. Detectors 3,4 and 8 had 2% to 3% smaller values, which was corrected for in later analysis.

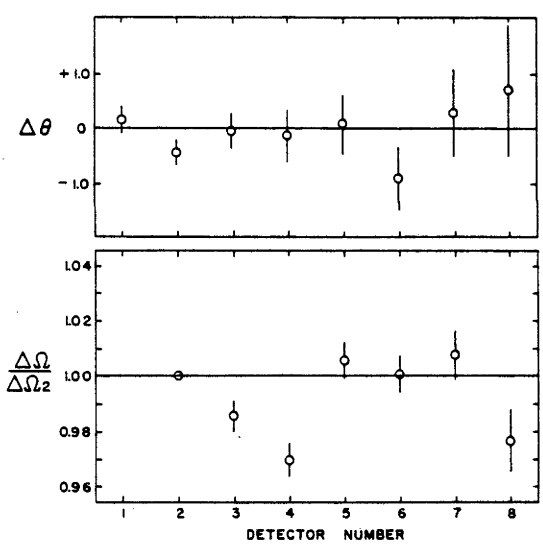

Fig. 4.5 Deviations ($\Delta\theta$) from nominal detector angles as measured with sub Coulomb-barrier scattering of ^{19}F from ^{197}Au. $\Delta\Omega/\Delta\Omega 2$ is the solid angle ratio relative to detector 2.

The ratio for detector 1 is not shown because the collimator size differs from the others ($\Delta\Omega 1/\Delta\Omega 2 \sim 0.47$). A smaller size collimator was chosen to reduce the count-rates at forward angles. The generalized-elastic yields were converted to cross-sections using the normalisation constant :

$$\frac{\Omega_{mon}}{\Omega_{det}} \frac{d\sigma_{Ruth}}{d\Omega}(\theta_{mon})$$

,which was determined from measured generalized-elastic yields at the most forward

angles, where the scattering was considered to be pure Rutherford.

When corrected for the energy dependence of $\sigma_{Ruth}(\theta_{mon})$ the normalisation constant was within 1% of the measurements at different beam-energies.

RESULTS

The generalized elastic yields were obtained by fitting Gaussian distributions to the elastic scattering energy spectra. Since the elastic scattering peaks showed tails on the low-energy side, which were partly due to inelastic processes and to energy straggling in the target and detector-window, an exponential function was folded in to the Gaussian to reproduce the skewness of the peaks. Because measurements were performed in transmission (particles left the target at the opposite side from where they entered) at forward angles and in reflection at the backward angles, the energy-straggling was different in each case.

Using a logarithmic scale for the number of counts, a change in slope of the low-energy tail could be seen, which marked the region over which inelastic scattering and transfer yields could be observed. Skewness parameters were obtained by least squares fits to the peaks, excluding this region.

Gaussian fits to the generalized elastic peaks with skewness parameters so obtained, excluded some of the inelastic scattering and most of the neutron transfer yields.

For the $^{139}La+^{19}F$ system this procedure could not be followed because of the presence of a long low energy-tail, which was probably due to non-uniformity in the target-thickness. For this system the yields were obtained by integration over the whole energy spectrum and will be referred to as quasi-elastics in the following. Angular distributions of generalized-elastic cross-sections will be shown in chapter 5. Error-bars were calculated from an assumed uncertainty in detector angle of $\pm 0.2^{\circ}$ and statistics. The uncertainty in angles, due to beam-spot movements, was estimated from the strip-target width (2 mm.) and the distance from target to detector of 300 mm. The errors (~2%) are mainly determined by angle uncertainty at forward angles and by statistics at larger angles.

Charged-particle transfer yields, obtained by integration within contour gates in the E-ΔE spectra, were converted to cross-sections using the normalisation constants, obtained from elastic scattering. Figure 4.6 shows angular distributions of one- and two-proton transfer for the system $^{159}Tb+^{19}F$ at different beam-energies. Distributions of 1p and 2p transfer-products peak around the same angle θ_T, which increases as the beam-energy decreases. At the higher energies the proton transfer cross-section drops sharply for angles larger than θ_T because of the onset of fusion in small impact collisions. This depletion of

the transfer channel by fusion reduces as the beam-energy approaches the Coulomb-barrier, which is demonstrated in fig. 4.6.

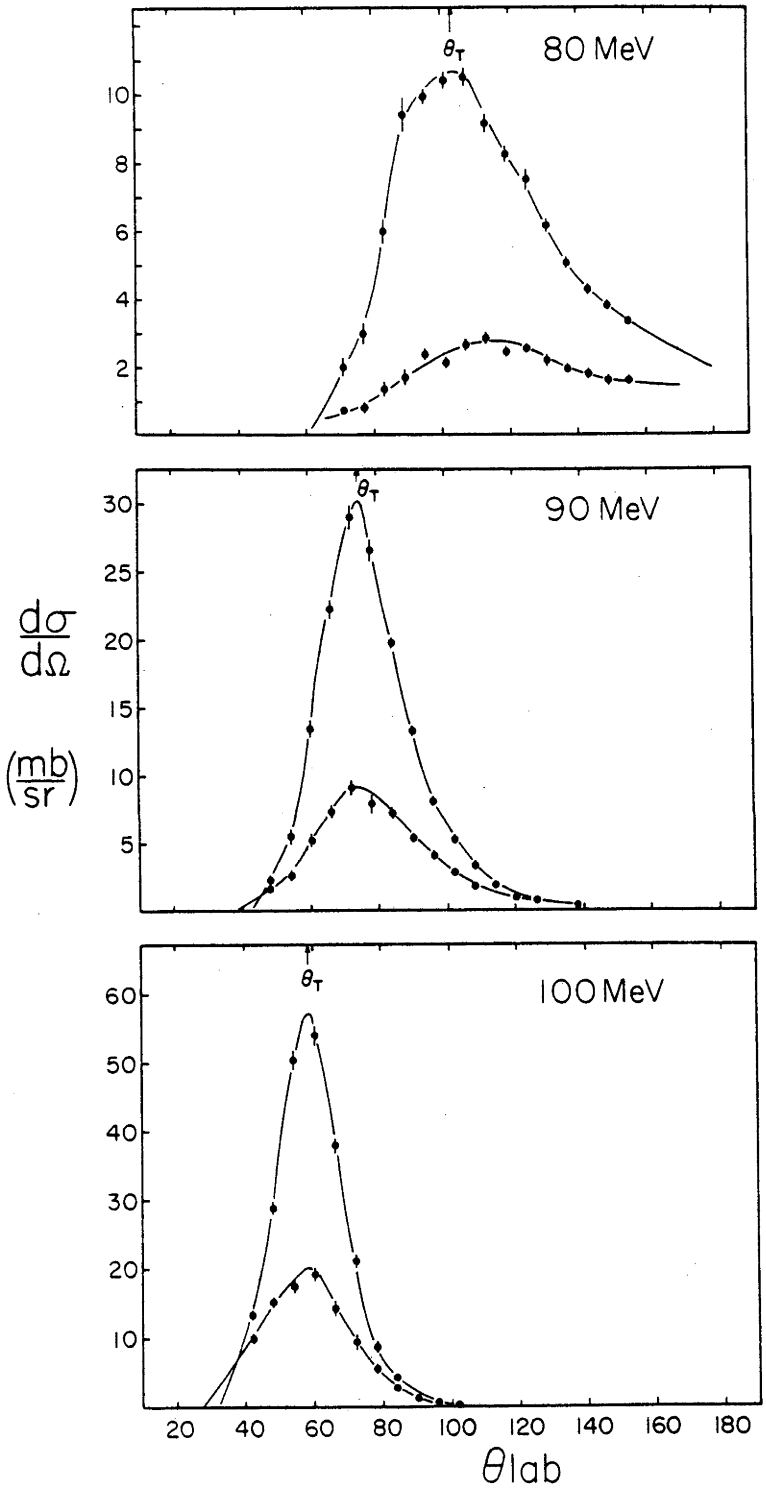

Fig. 4.6 Angular distributions of oxygen and nitrogen ejectiles from the reaction $^{159}Tb+^{19}F$ at different bombarding energies. The angles θ_T, at which the differential cross-section distributions obtain their maximum, are listed in table 4.3. The cross-sections for oxygen ejectiles are larger than those for nitrogen.

For angles smaller than θ_T the cross-section drops due to the larger separation between the nuclei (reduced overlap of nuclear matter).

From the angular distributions the total charged-particle transfer cross-sections were calculated using :

$$\sigma = 2\pi \int \frac{d\sigma}{d\Omega}(\theta) \sin\theta \, d\theta \qquad (4.1.1)$$

Total cross-sections are given in table 4.3 together with the angles θ_T at which the angular distributions peak. Errors in the cross-sections were determined from statistics only. Proton transfer for $^{150}Sm+^{18}O$ is about a factor 4.5 lower than for all other systems. This is mainly a kinematical effect. The ground-state Q-value for 1p transfer in $^{150}Sm+^{18}O$ is more negative than the preferred Q-value (-8 and -9 MeV) calculated from

$Q/E = Z_t^{-1} - Z_p^{-1}$ [But71] for respectively 80 MeV and 90 MeV beam-energies. For all other systems Q-preferred is more negative than Q ground-state.

Table 4.3 One- and two-proton stripping cross-sections for different systems and incident energies. The last column contains the laboratory angles at which the differential cross-sections are maximum.

Systems	E (MeV)	1p (mb)	2p (mb)	θ_T(lab) (degrees)
$^{159}Tb+$	80	56.5 ±1.5	18.8 ±0.9	104
^{19}F	90	96 ±2	39 ±2	73
	100	120 ±3	65 ±2.5	58
$^{169}Tm+$	80	40 ±2	9 ±1	125
^{19}F	90	87 ±3	33 ±2	81
	100	109 ±5	65 ±2.5	64
$^{181}Ta+$	90	74 ±2	28 ±1.5	95
^{19}F	100	106 ±5	40 ±4	70
	110	117 +3		57
$^{150}Sm+$	70	7.5 ±1		100
^{18}O	80	18 ±2		68
	90	29 ±3		51

4.1.2 ELASTIC AND INELASTIC SCATTERING

Figure 4.7 shows two dimensional E-ΔE and focal-plane position versus energy spectra obtained in the nuclear scattering measurements of ^{18}O from ^{150}Sm, performed with the Enge magnetic-spectrograph. The position-E spectrum for oxygen particles was generated with a software contour gate in the E-ΔE spectrum. It shows the oxygen-isotope groups for charge-states (8^+,7^+,6^+). The relative intensities are approximately (1: 0.4 : 0.03). Clearly distinguished groups of ^{19}O, ^{18}O, ^{17}O and ^{16}O isotopes can be seen for each charge state. The position spectra for ^{18}O were obtained by applying contour gates in both E-ΔE and position vs. E spectra. Figure 4.8 shows the result of this procedure for ^{18}O-ions in the 8^+ charge state measured at 70° laboratory-angle and 90 Mev beam energy. The ground state, first 2^+ and 4^+ excited states in ^{150}Sm are clearly resolved. Also the first excited 2^+ state of ^{18}O at 1.98 Mev can be seen. The two arrows around this state indicate the calculated Doppler - broadening due to gamma- ray emission from the fast moving ^{18}O projectile. All other events are from unresolved states in ^{150}Sm. Elastic and 2^+ excited state yields were extracted from the 8^+ charge-state spectra with Gaussian peak fitting. The statistical errors of the 7+ and 6+ charge-state spectra were too large to apply the same technique. The ratios of elastic to 2^+-state yields, found from the 8^+ charge-state position spectra were used to extract yields from the 7^+ and 6^+ charge-state spectra.

The samarium target, used in the experiment contained some isotopic impurities as given in table 3.3, chapter 3 (from manufacturer). The main impurity contribution is from the ^{149}Sm and ^{152}Sm isotopes. Their elastic and inelastic peaks are contained in the ^{150}Sm elastic peak. From Coulomb excitation probabilities, calculated with the Winther-de Boer program [Win65], the change in the $d\sigma_{el}/d\sigma_{Ruth}(\theta)$ distribution, due to impurities, was estimated. At the forward angles (30° to 70° for E_{beam}=80 MeV) the ratio of calculated elastic scattering yield from ^{150}Sm to the measured elastic yields changed by less than 1%. For larger angles the impurity effect is difficult to estimate because of the interference of Coulomb and nuclear excitation. The elastic scattering data were not corrected for impurity effects, instead the errors were increased by 1%. The inelastic 2^+ yields were less affected by the impurities because of the difference in excitation energies of the first excited states.

In table 4.4 the partial cross-sections are given for elastic scattering and excitation to the 2^+ and 4^+ excited states in ^{150}Sm. Elastic cross-sections are expressed as ratios to Rutherford cross-sections.

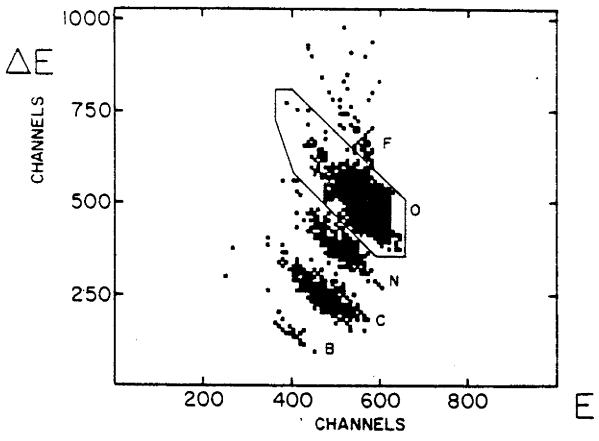

Fig. 4.7 Charge separation with the E-ΔE detection technique and oxygen-isotope separation with the focal plane position information for the reaction $^{150}Sm+^{18}O$ at 90 MeV. The three groups indicated with 8^+,7^+ and 6^+ are the different charge-states of the ions after traversing the target.

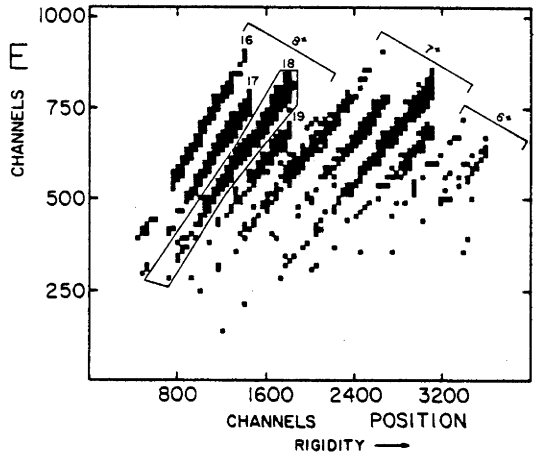

Fig. 4.8 Focal plane position spectrum of ^{18}O-ions, generated by sorting with software contour gates as indicated in fig. 4.7.

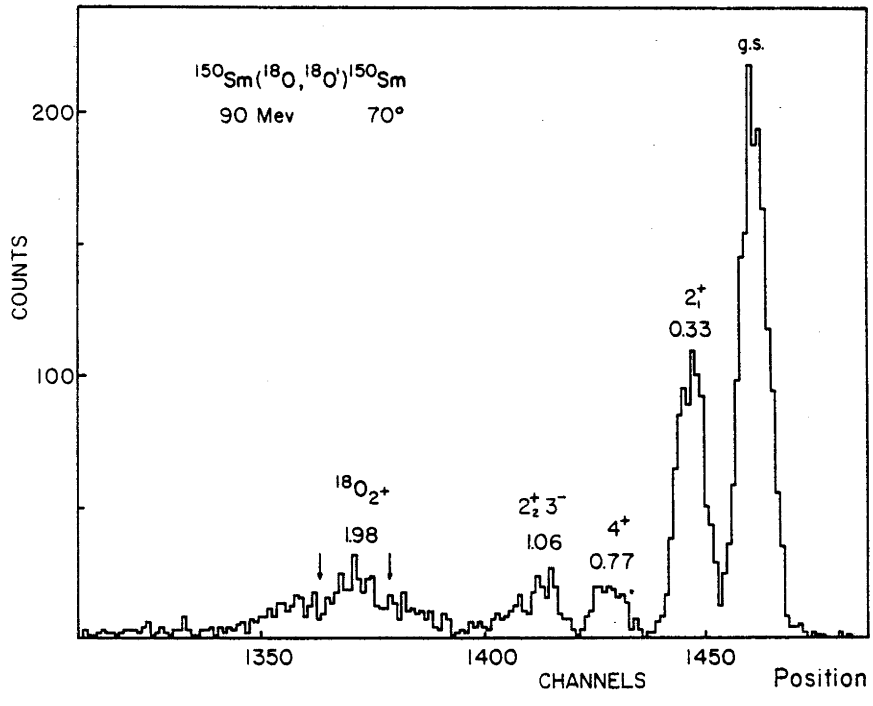

Table 4.4 $^{150}Sm(^{18}O,^{18}O')^{150}Sm$. Differential elastic scattering cross-sections, expressed as ratios to the Rutherford cross-sections, and differential cross-sections for the inelastic scattering to the 2^+ and 4^+ excited states in ^{150}Sm.

	θ_{lab} (degrees)	$\sigma_{el}/\sigma_{Ruth}$	± %	$d\sigma_{2^+}/d\Omega$ (mb/sr)	± %	$d\sigma_{4^+}/d\Omega$ (mb/sr)	± %
Elab=	30	0.989	±2.0	257.5	±4.0		
75 MeV.	50	0.895	2.0	157.7	2.5	10.5	±9.0
	65	0.832	2.5	122.2	2.5	8.5	9.0
	70	0.853	2.0	97.87	3.0	9.5	6.0
	75	0.806	2.5	73.70	3.0	9.1	6.0
	80	0.690	2.0	63.17	3.0	8.3	4.0
	85	0.527	3.0	45.11	3.5	7.5	7.0
	90	0.353	3.0	31.99	3.5	5.4	5.0
	100	0.124	3.5	11.44	4.0	3.2	5.0
	110	0.044	4.0	3.96	4.5		
Elab=	30	0.982	±2.0	237.7	±4.0		
80 MeV.	40	0.942	2.0	210.9	3.0		
	50	0.881	2.0	160.1	3.0	9.9	±7.0
	55	0.876	2.0	158.7	3.0	9.7	8.0
	60	0.898	2.0	123.1	3.0	9.4	6.5
	65	0.877	2.0	95.7	3.5	9.9	7.0
	70	0.679	2.0	79.6	4.0	9.6	5.0
	75	0.462	2.5	50.1	3.5	7.0	6.5
	80	0.246	2.5	28.1	4.0	6.1	5.0
	85	0.124	4.0	14.8	4.5	3.4	7.5
	90	0.057	4.5	7.02	5.5	1.7	8.5
	100	0.010	7.0	1.36	7.5		
Elab=	25	0.987	±2.0	312.9	±5.0		
90 MeV.	30	0.974	2.0	275.4	3.0		
	35	0.960	2.0	252.0	3.5		
	40	0.916	2.0	227.2	3.5		
	45	0.934	2.0	194.0	3.0	9.6	±7.0
	50	1.014	2.0	156.0	3.0		
	55	0.786	2.0	137.6	3.0	11.9	5.0
	60	0.421	2.0	51.5	3.0	7.4	5.0
	65	0.173	2.0	30.1	3.0	5.6	4.0
	70	0.0578	3.5	10.9	3.5	2.5	6.5
	75	0.0201	4.0	3.79	4.0	0.9	7.0
	80	0.0065	8.0	1.05	8.0		
Elab=	25	1.003	±2.0	332.5	±4.0		
100 MeV.	30	0.954	2.0	282.2	3.5		
	35	0.887	2.0	292.4	2.5	8.4	±13.0
	40	1.065	2.0	203.0	3.0		
	45	0.883	2.5	165.2	3.0	10.2	12.0
	50	0.424	3.0	82.6	3.5	9.2	11.0
	55	0.137	3.5	31.5	3.5	5.6	9.0
	60	0.0367	6.0	9.75	7.0		

4.2 EVAPORATION RESIDUES

IDENTIFICATION

A typical example of the identification of evaporation residues (ER) with the experimental technique described in sections (3.1.2) and (3.4.3) is illustrated in fig. 4.9. It shows the ER from ^{188}Pt formed in the fusion reaction $^{169}Tm + ^{19}F$ at 80 Mev beam energy, which is well above the fusion barrier. Only the time spectra associated with low-energy events (<10 MeV.), obtained with high amplification (section 3.4.3), are shown.

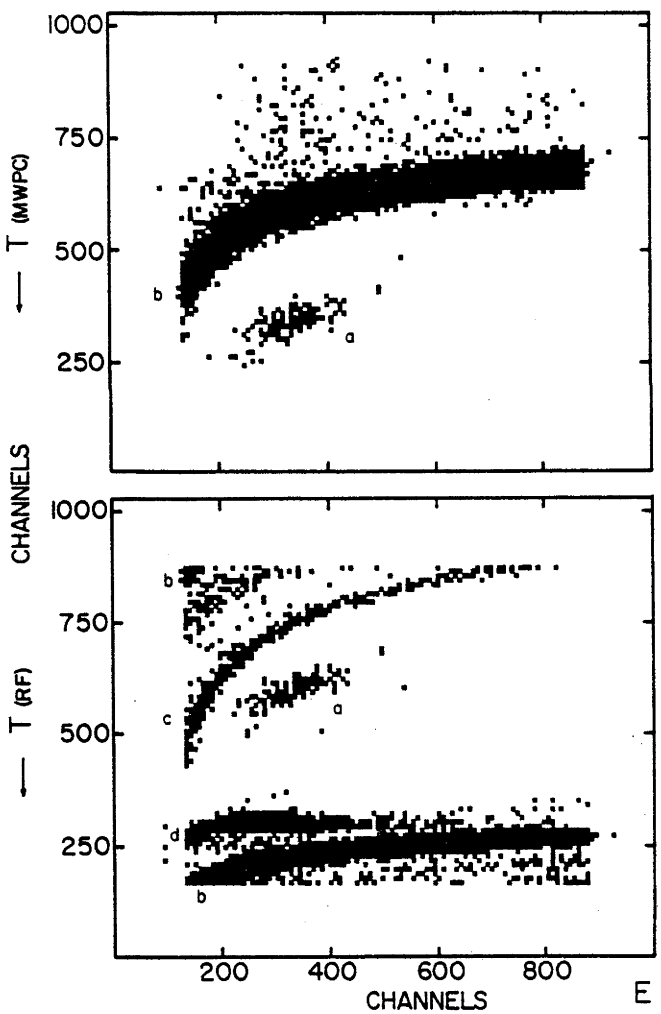

Fig. 4.9 Identification of the evaporation residues with the time of flight technique. Time differences between MWPC and E-counter and RF signal and E-counter are indicated with $T_{(MWPC)}$ and $T_{(RF)}$ respectively.

The elastic peak is off the energy-scale. The T_{RF-E} spectrum shows all events detected between two beam bursts. In both time versus energy spectra T_{MWPC-E} and T_{RF-E} the evaporation residues (indicated with a) are clearly separated from slit-scattered projectiles (b). Events in the tail (c) result from particles scattered from the beam-line collimators. The group of events (d) with flight-times shorter than the elastics result from protons and alpha-particles. They are not seen in T_{MWPC-E} because of their low energy-loss in the M.W.P.C. At lower bombarding energies identification is complicated because of the reduced E.R. kinetic energy and the higher ratio of slit-scattered projectiles to E.R. Figure 4.10 shows that clear E.R. identification from the T_{MWPC-E} spectrum alone is no longer possible.

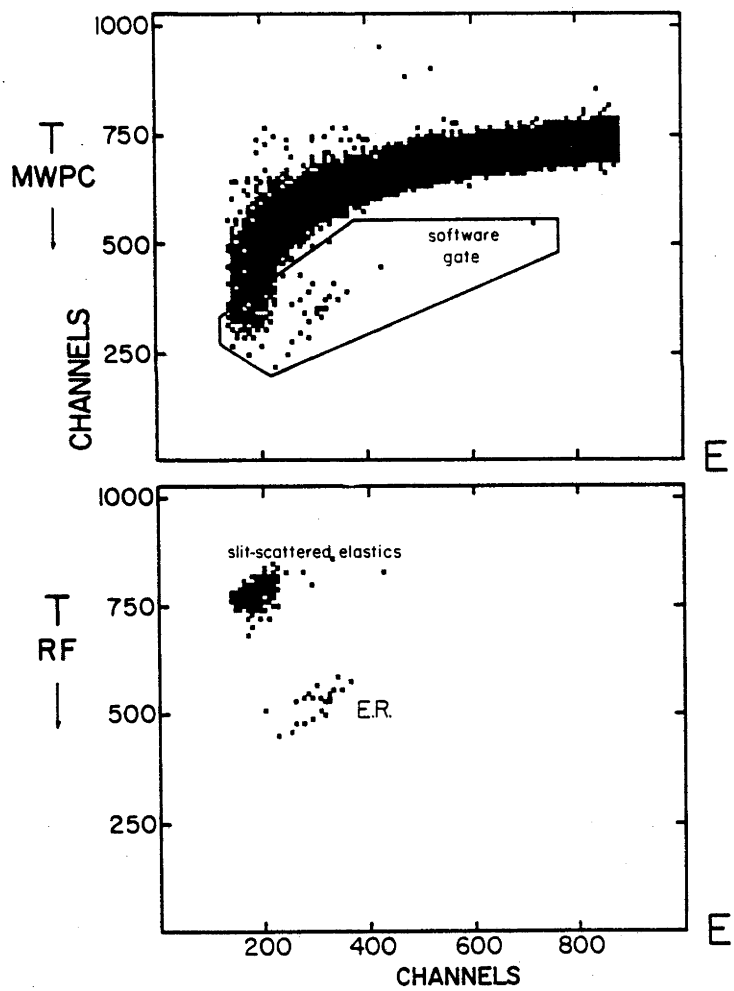

Fig. 4.10 Same as in fig. 4.9, but for low cross-section measurement. With a software contour gate in the upper spectrum clear identification of ER is obtained in the lower spectrum.

Also T_{RF-E} by itself does not provide a reliable identification mainly due to spurious counts resulting from slit-scattering along the beam line. However, combining time information from both spectra provides clear identification as can be seen in the lower spectrum of figure 4.10 This technique proved to be very successful in identifying E.R. where the cross-sections are very low.

CALIBRATION AND NORMALISATION

The Normalisation constant A and off-set angle $\Delta\theta$, defined in section (3.4.3), were calculated for every system and beam-energy from elastic (Rutherford) scattering, measured at angles larger than 6° on both sides of the beam-axis. The off-set angle $\Delta\theta$ was smaller than 0.15° in most experiments.

In the E.R. measurements with the tungsten-isotopes $\Delta\theta$ was less than 0.1° for $^{184,186}W+^{16}O$ but for the $^{182}W+^{16}O$ system $\Delta\theta = 0.4^\circ$ at all energies measured. During this particular experiment the measurements were performed by successive irradiation of the different targets under near identical conditions i.e. no change in beam or detector position. Therefore the only likely cause for the difference in $\Delta\theta$ is a mis-allignment in the target-strip of ^{182}W. Considering a distance from target to detector of 120 mm. the strip had to be displaced from center position by 0.8 mm. to explain the 0.4° difference. This is the most likely cause, since the strip-target width was 1 mm. All angular distributions were corrected for $\Delta\theta$. Also in the normalisation constant $A = N_{mon}/N_{det}$ $d\sigma/d\Omega_{Ruth}(\theta+\Delta\theta)$ the measured off-set angle has been taken into account.

RESULTS

Angular distributions of E.R. from the reactions : $^{19}F+^{159}Tb \rightarrow ^{178}W$; $^{19}F+^{169}Tm \rightarrow ^{188}Pt$; $^{18}O+^{150}Sm \rightarrow ^{168}Yb$; $^{16}O+^{182,184,186}W \rightarrow ^{198,200,202}Pb$ and $^{16}O+^{176,180}Hf \rightarrow ^{192,196}Hf$ are shown in figures 4.11; 4.12; 4.13 and 4.14. The cross-sections measured at positive and negative angles as defined in fig. 3.7 (chapter 3) are indicated as open and closed circles respectively. Error-bars were calculated from statistics.

For the smaller angles where the cross-section drops rapidly with increasing angle, the residues originate from neutron evaporation. At larger angles the slope of the distribution changes due to the evaporation of protons and alpha-particles, which give rise to greater deflection of E.R. because of their high energy.

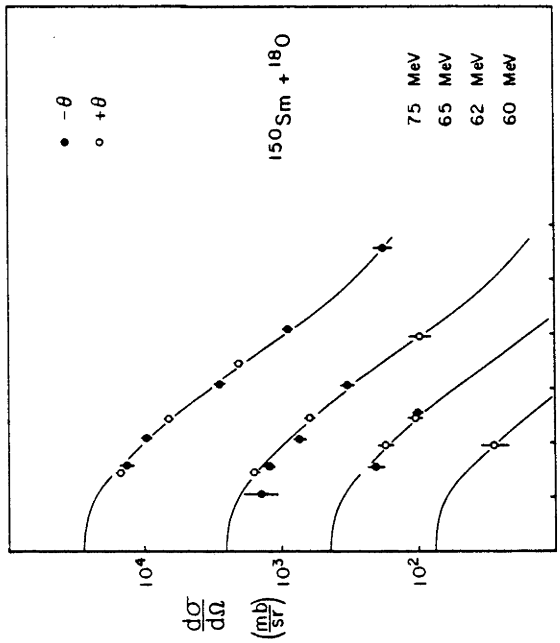

Fig. 4.12 As in fig. 4.11 for the reaction $^{150}Sm+^{18}O$.

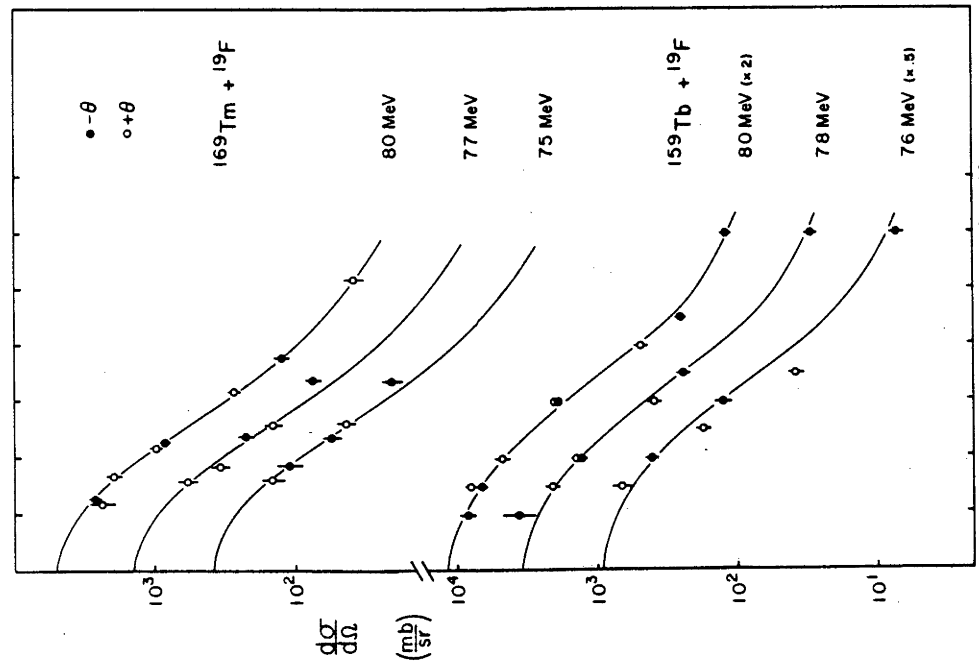

Fig. 4.11 Evaporation residue angular distributions obtained for the reaction $^{159}Tb+^{19}F$ and $^{169}Tm+^{19}F$. The smooth curves through the data points were used to calculate the total ER cross-sections. The curves were extrapolated to zero degrees with ZPACE calculations as explained in the text.

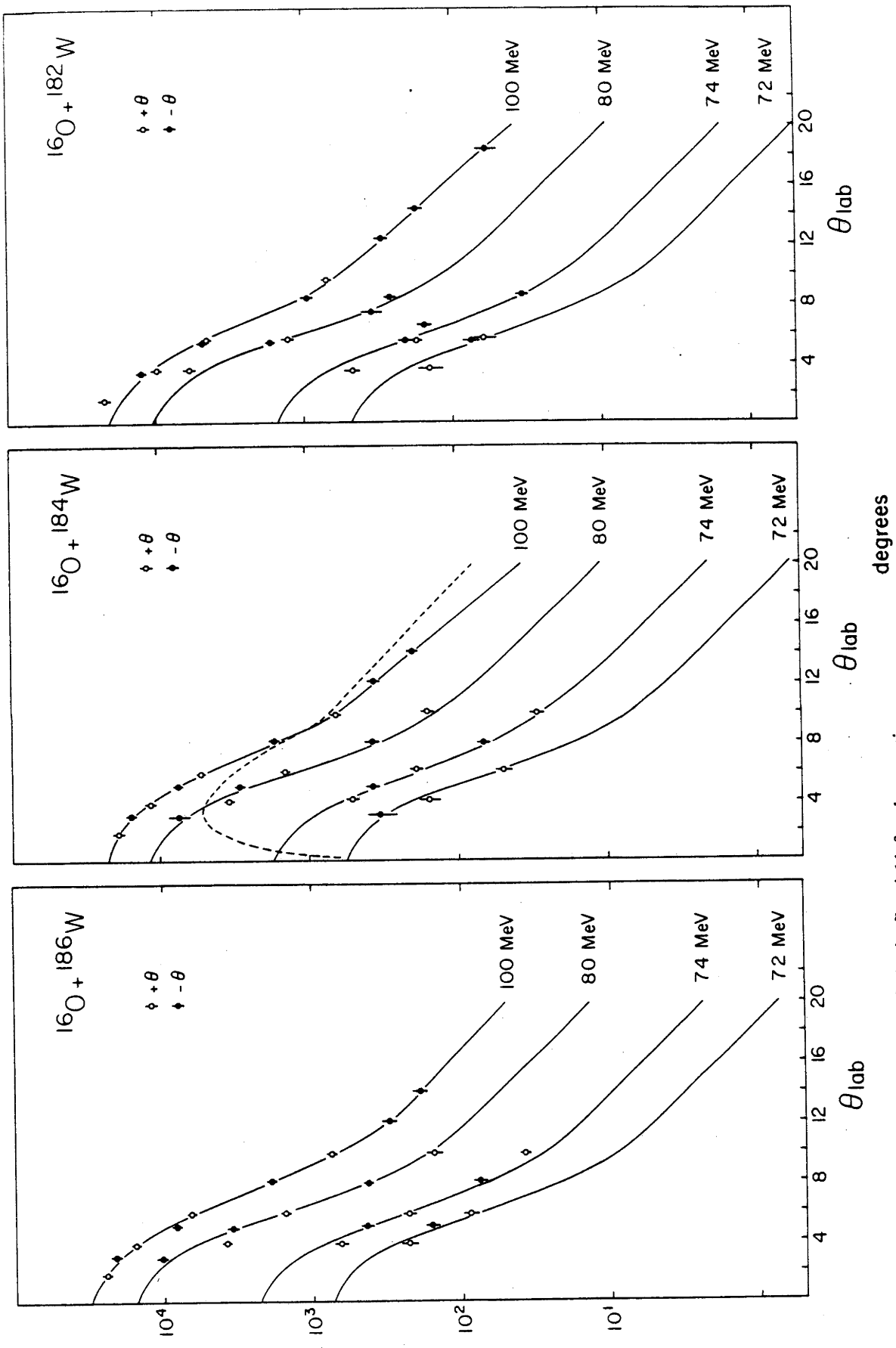

Fig. 4.13 As in fig. 4.11 for the reactions $^{182,184,186}W+^{16}O$.

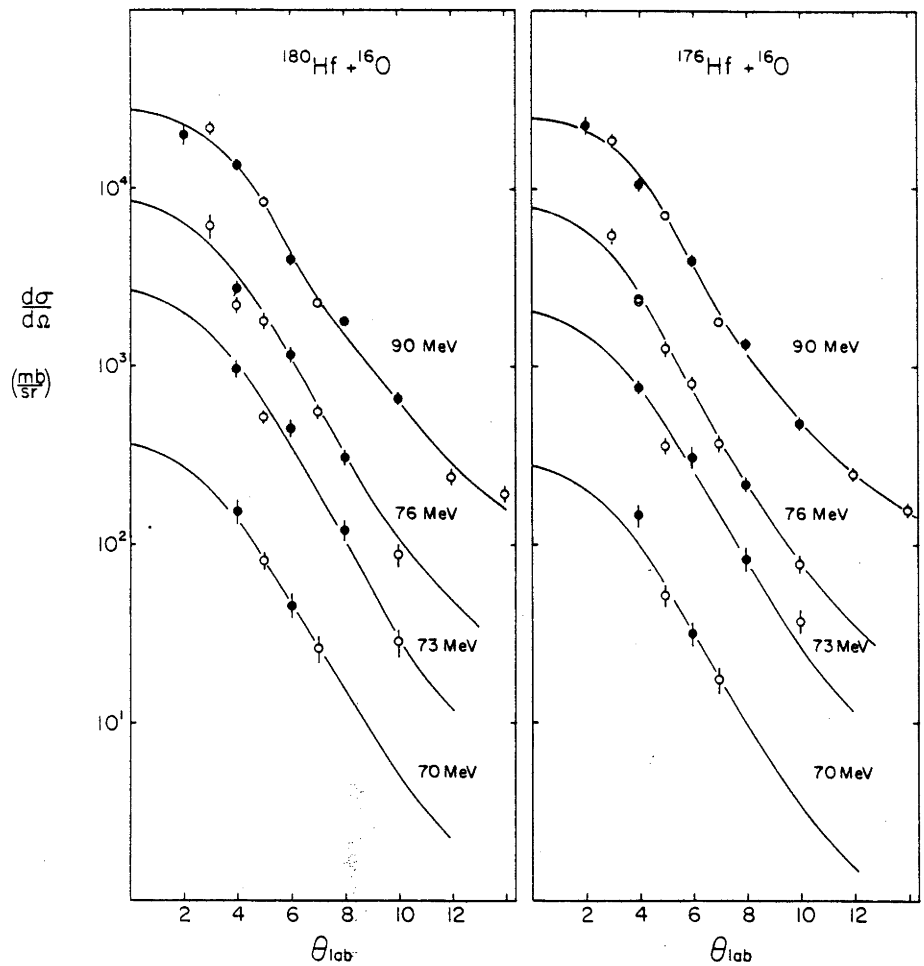

Fig. 4.14 As in fig. 4.11 for the reactions $^{176,180}Hf+^{16}O$.

For total cross-section determination smooth curves were drawn through the data-points of the distribution for which the most angles were measured. The curves were extended to zero degrees by means of a statistical model calculation. The Monte carlo code ZPACE [Gav80] was used to calculate the shape of the E.R. angular distribution, which was then scaled to match the experimental curve. At the lower bombarding energies fewer angles were measured, for which cases the measured shape of the nearest energy was used. The total E.R. cross-section was calculated from :

$$\sigma_{ER} = 2\pi \int \frac{d\sigma_{ER}}{d\Omega} \sin\theta \, d\theta$$

Because of the sin(θ) factor the determination of $d\sigma_{E.R.}/d\Omega$ near zero degrees is not

critical. It can be seen from figure 4.13b (dashed line) that most accurate measurements are required in the interval (2°-8°). The total E.R. cross-sections and their errors, calculated from statistics are given in table 4.5.

Table 4.5 Evaporation residues cross-sections for various systems and energies.

E_{lab} (MeV)	$^{150}Sm+^{18}O$ σ(mb)	E_{lab} (MeV)	$^{169}Tm+^{19}F$ σ(mb)	E_{lab} (MeV)	$^{159}Tb+^{19}F$ σ(mb)
75	440 ±28	80	59 ±8	79.7	125 ±18
65	40 ±6	77	16 ±2.5	77.7	69 ±6
62	7.3 ±1.2	75	4.3 ±0.9	75.7	40 ±4
60	1.2 ±0.3			73.7	17 ±2.5

E_{lab} (MeV)	$^{182}W+^{16}O$ σ(mb)	E_{lab} (MeV)	$^{184}W+^{16}O$ σ(mb)	E_{lab} (MeV)	$^{186}W+^{16}O$ σ(mb)
100	405 ±34	100	585 ±50	100	715 ±68
80	191 ±16	80	210 ±17	80	236 ±19
74	21 ±2.5	74	33 ±4	74	37 ±4.4
72	7.4 ±1.3	72	8.3 ±1.5	72	12.3 ±2.2

E_{lab} (MeV)	$^{176}Hf+^{16}O$ σ(mb)	E_{lab} (MeV)	$^{180}Hf+^{16}O$ σ(mb)
90	531 ±70	90	599 ±70
76	107 ±15	76	131 ±20
73	35.4 ±5	73	47.6 ±7
70	4.8 ±1	70	6.5 ±1.3

4.3 GAMMA-RAY MULTIPLICITIES

During the gamma-ray multiplicity measurements the following parameters were recorded :

In List-Mode : Germanium (Ge) linear ; Fold-signal ; (Ge-ΣNaI) TAC ; (Ge-3" NaI) TAC and the 3" NaI linear signal.

In Singles-Mode : Ge-singles ; 0,1,2 - Fold Ge energy-spectra.

The 1-Fold rate in the list-mode data was scaled down to reduce dead-time. Four different ADC's were used in the singles-mode data collection. To facilitate data analysis

the channel-shifts and gains of the singles-spectra were adjusted off-line to be the same as those for the list-mode spectra.

List-mode and singles-mode spectra could then be analysed in a consistent way by setting appropriate peak and background windows. However, this was not always easy for the singles and Fold-0 spectra, because of the presence of strong low-multiplicity peaks from activities and Coulomb excitation. Such low-multiplicities peaks are weak in the higher Fold-spectra. They can be identified from known Coulomb excitation and activity lines and from subtracting ΣFold-spectra from the singles spectra.

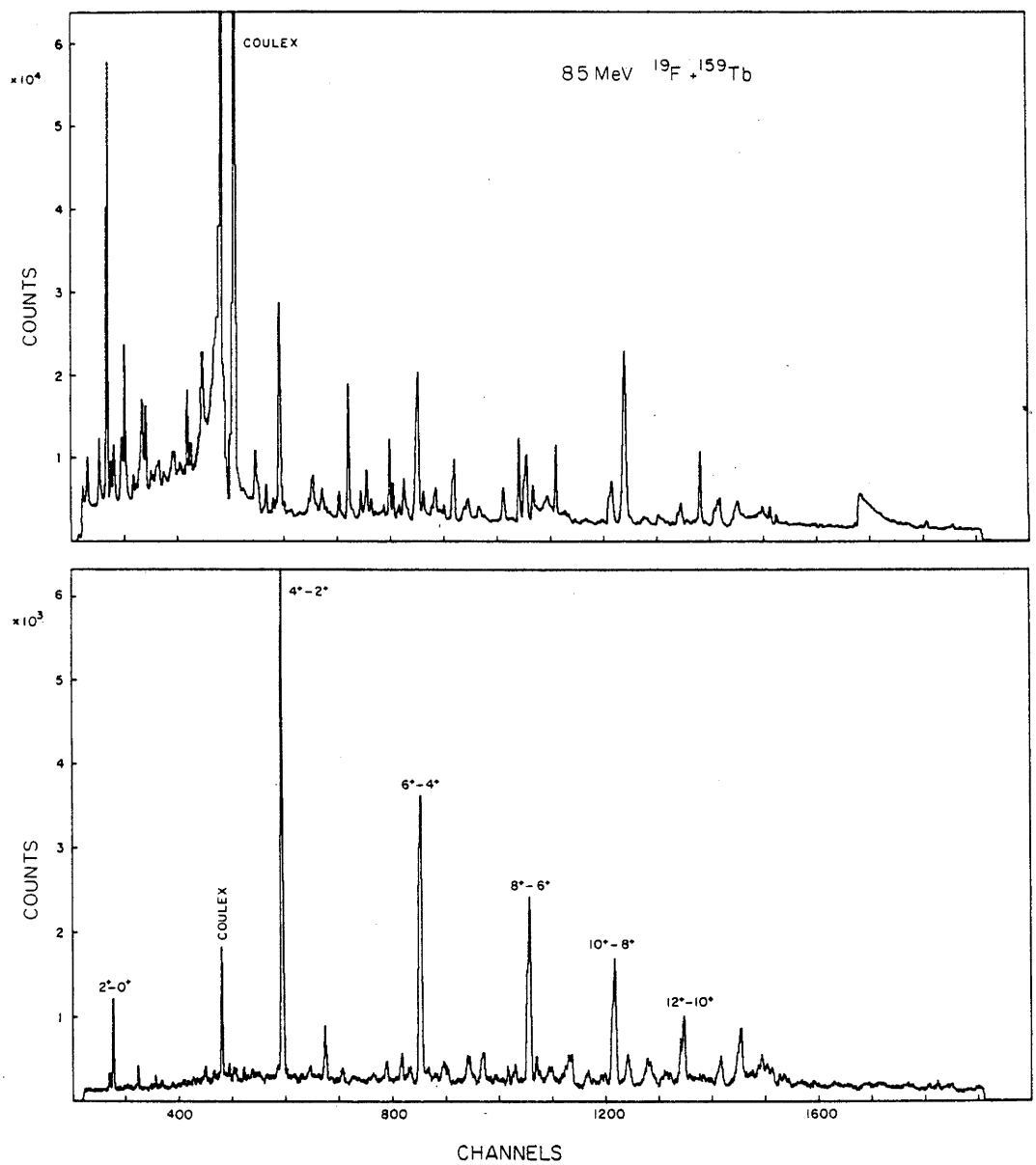

Fig. 4.15 Germanium-detector gamma-ray spectra from the reaction $^{159}Tb+^{19}F$ at 85 MeV. A singles spectrum (upper) and a Fold-2 spectrum (lower) are shown. The transitions indicated are of the 4n-channel. The yield of the 2^+- 0^+ (114 keV) transition is low because of electron conversion and a low detection efficiency.

The ΣFold-spectra were suitably normalised so as to (for example) remove the 4n-channel 8^+-6^+ ground state band transition. This removed fairly well all of the other 4n (and to a large extent the 5n) transitions, leaving the interfering transitions.

Figure 4.15 shows a singles and a Fold-2 gamma-ray spectrum for the reaction ^{159}Tb+^{19}F at 85 MeV. The transitions indicated in the Fold-2 spectrum are from the 4n-channel, which is dominant for this energy. Most lines in the singles-spectrum are from activities or Coulomb excitation, which have low multiplicity and therefore are very weak in the Fold-2 spectrum.

To get the Fold intensities for a line it is necessary to correct for dead-time. Since Folds 1-6 of the List-mode data all have the same dead-time, it was necessary only to get the relative dead-time of Fold-0 (or singles) to the List-mode data. The dead-times were determined from comparison of scalers and integrated spectra.

In fig. 4.16 a gamma-ray energy spectrum is shown from the 7.26 cm. NaI-detector.

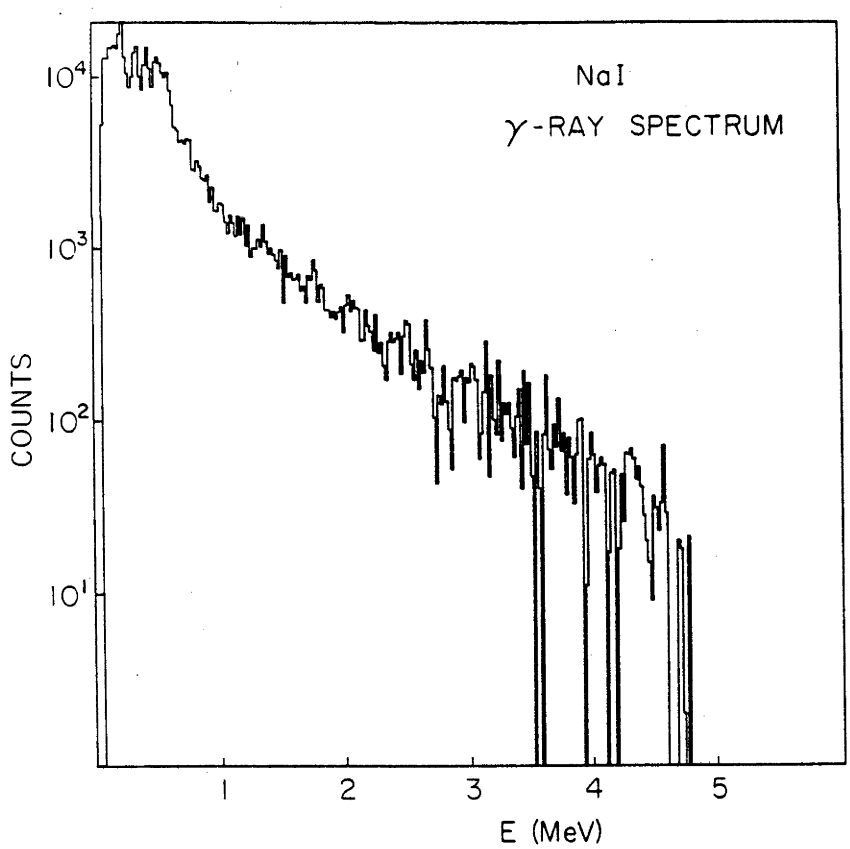

Fig. 4.16 NaI-detector gamma-ray spectrum on a logarithmic scale. It shows an exponential tail of statistical gamma-rays.

Some low-energy discrete lines are visible on top of a continuous spectrum of statistical E1 and Yrast-like E2 gamma-rays. The contribution from E1-transitions shows an exponential tail extending to high energies. In principle one can obtain the number of statistical gamma-rays from this spectrum by unfolding it using the detector response function [Sie78]. The E1-spectrum may then be separated by assuming a functional form for the E1 energy spectrum and fit this function to the observed exponential tail.

4.4 FISSION

Clear identification of fission fragments for relatively large cross-sections (> 10 mb.) was obtained with the E-ΔE technique as demonstrated in fig. 4.17.
It shows fission-fragments from ^{200}Pb, formed in the fusion-reaction ^{181}Ta+^{19}F at 100 MeV beam-energy.

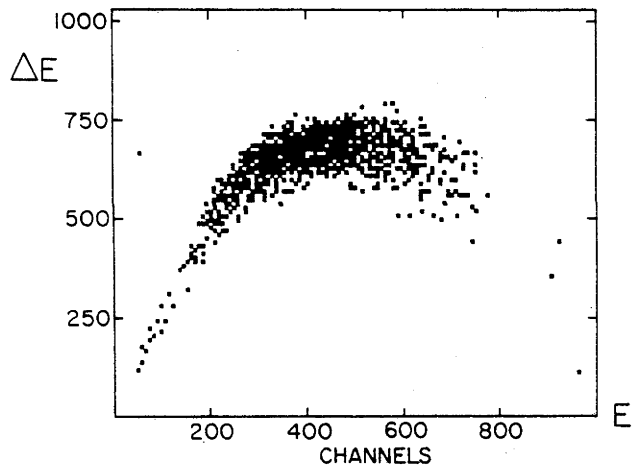

Fig. 4.17 Fission-fragments from the reaction ^{181}Ta+^{19}F, identified with the E-ΔE detection technique. Elastic scattering events are not visible because of their much smaller signals in the ΔE-detector.

At lower beam-energies identification was complicated by spurious counts, which had a more dramatic effect at low cross-sections. The fission fragments were therefore measured in a E-ΔE telescope, requiring coincidence with the complementary fragments, measured in a large solid angle detector as described in section 3.1.3 . The coincidence detection technique was succesful in measuring cross-sections for ^{18}O and ^{19}F induced fission to as low as 1 μb. With the energy information of both fission-fragments it was also possible to resolve the fission events resulting from a heavy element impurity in one of the targets. This is illustrated in fig. 4.18.

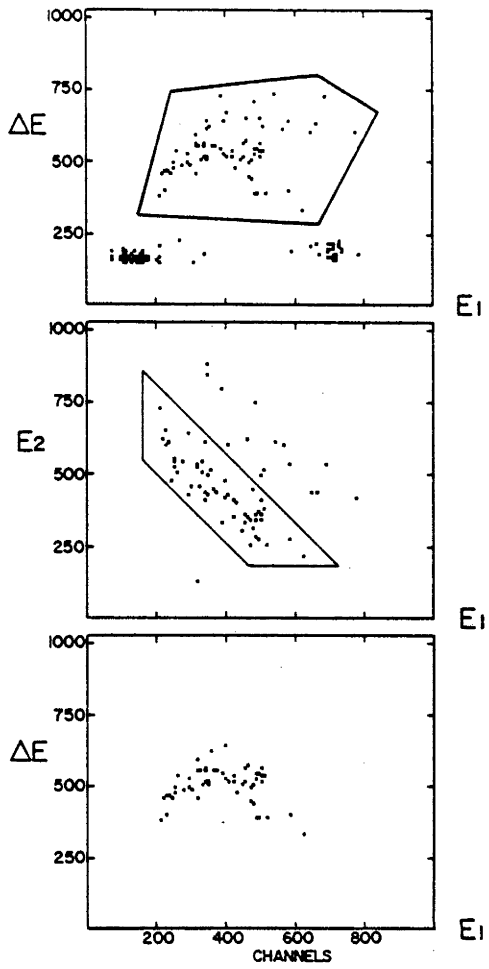

Fig.4.18 Separation of a heavy target-impurity with the coincidence detection technique. The middle E_2-E_1 spectrum was generated with the indicated contour gate in the upper spectrum. It shows two groups with different total energy. The lower spectrum results from sorting with both contour gates.

In the E2 versus E1 spectrum there appears to be two groups of fission events with different sum energies. From equation (3.1.5) it can be seen that the fission events with higher sum-energy originate from a heavier compound nucleus. Although the fusion-barrier for compound nucleus formation with the heavier nucleus is higher, the fission yields are considerable due to the higher fissility of the heavier system. Thus in measuring low cross-sections with a single detector, it is essential to ensure the target is reasonably free from heavy-element impurities.

In the fusion-fission experiments for $^{124}Sn+^{58}Ni$ reaction, identification was further complicated by the presence of coincident elastic-recoil events. The heavy ^{58}Ni-projectile brings more momentum into the compound system, resulting in a more forward peaked angular distribution of fission-fragments in the laboratory-frame. Consequently the complementary fragment detector had to be positioned at a more forward angle (70°), which implied also that projectiles coincident with recoiling nuclei were detected. The mass distribution of fission-fragments peaks at half the mass-value of the compound nucleus,

which in this case is A=91. Asymmetric mass-split may result in fragments with masses similar to projectile and target-nucleus and are therefore difficult to distinguish from elastic-recoil events. However, there is a difference in total kinetic energy. For the elastic-recoil scattering it is equal to the beam-energy (240 MeV.), whereas for the fission process the total kinetic energy is given by :

$$\frac{M_p}{M_p+M_t} E_{beam} + 0.1189\, Z^2 A^{-1/3} + 7.3 \text{ MeV}$$

which for the given system and energy is 211 MeV.

The E-ΔE spectrum in the top half of fig. 4.19 shows the elastic scattered particles and recoil nuclei, detected in the telescope-detector.

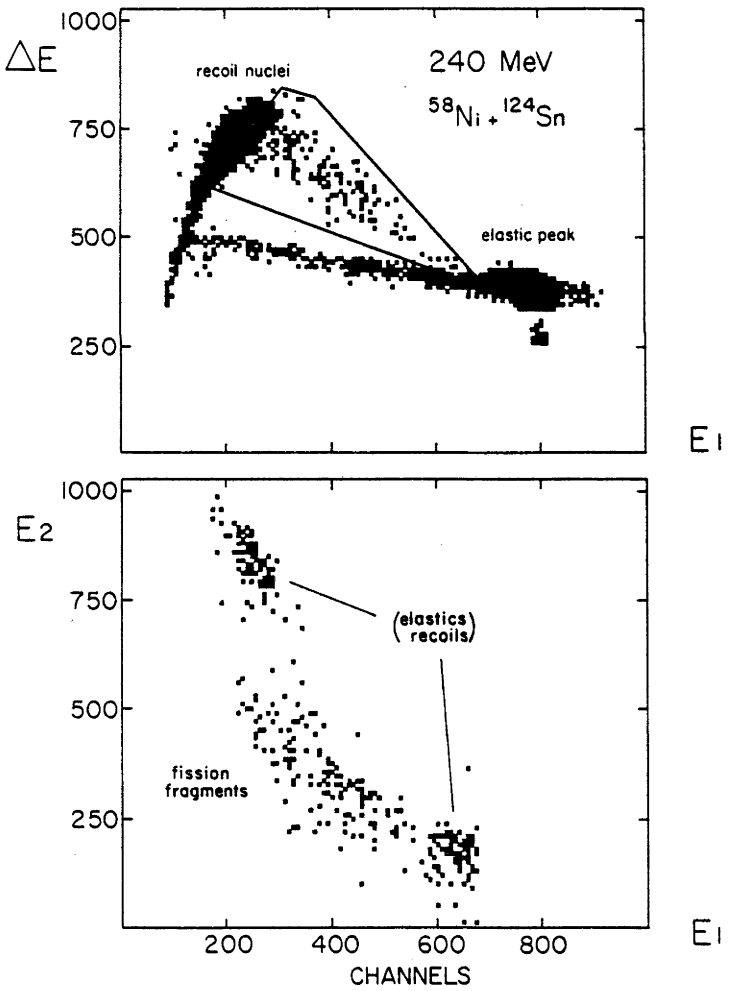

Fig. 4.19 Identification of fission-fragments from the reaction $^{124}Sn+^{58}Ni$ at 240 MeV. bombarding energy. The lower spectrum is obtained by sorting with the contour gate indicated in the upper spectrum.

Although coincidence with the large solid-angle detector has been required, the fission-fragments (within the triangle) are not completely resolved from the elastic scattered particles and recoil nuclei. However, projection of the events in the triangle onto the E2-E1 plane shows that the diagonal connecting elastic slit-scattered particles with recoil nuclei is different from the diagonal through the fission fragments.

CALIBRATION AND NORMALISATION

When applying the coincidence technique it is important to ensure that for every measured fragment in the telescope the corresponding fragment is detected in the large solid angle detector. The dependence of the fission-fragments coincidence rate on the angle of the complementary fragment detector (large solid angle) is shown in fig. 4.20 for fission of ^{200}Pb formed in the fusion reaction ^{181}Ta+^{19}F at 100 MeV beam-energy. The arrow indicates the angle as calculated from kinematics assuming equal mass-split. For different beam-energies the detector angle was corrected according to calculation.

Angles of the monitor-counters were calibrated with elastic scattering in the same way as described for the nine-angle detector-telescope.

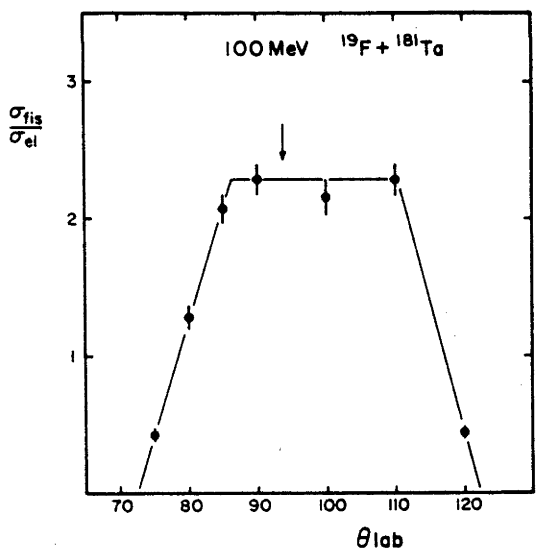

The monitor turn-table was rotated, while the detector-telescope was kept at the same angle. For the ^{19}F and ^{18}O induced fission measurements, the monitor detectors angles were found to be at $19.3 \pm 0.2^{\circ}$ (mon1) and $19.9 \pm 0.2^{\circ}$ (mon2). Using these

angle-values the ratios $\Delta\Omega_{m1}/\Delta\Omega_{det}$ and $\Delta\Omega_{m2}/\Delta\Omega_{det}$ were 2.491 10^{-3} and 2.487 10^{-3} respectively. For the $^{124}Sn + ^{58}Ni$ system similar agreement and accuracy was found.

RESULTS

Partial fission cross-sections in the laboratory-frame were calculated from :

$$\frac{d\sigma_{fis}}{d\Omega_{lab}} = \frac{N_{fis}}{N_{el}(m1+m2)\Omega_{det}} \left\{ \Omega_{m1} \frac{d\sigma_{Ruth}}{d\Omega}(\theta_{m1}) + \Omega_{m2} \frac{d\sigma_{Ruth}}{d\Omega}(\theta_{m2}) \right\} \qquad (4.4.2)$$

The total fission cross-section was calculated assuming a $1/\sin\theta_{cm}$ dependence of the fission-fragment angular distribution. The centre of mass partial cross-section was obtained from :

$$\frac{d\sigma_{fis}}{d\Omega_{cm}} = \frac{d\sigma_{fis}}{d\Omega_{lab}} \frac{d\cos(\theta_{lab})}{d\cos(\theta_{cm})} = \frac{\sin^2\theta_{lab}}{\sin^2\theta_{CM}} \cos(\theta_{CM}-\theta_{lab})$$

$$\theta_{CM} = \theta_{lab} + \phi$$

Angle ϕ was calculated from the fission-fragment and the compound nucleus velocity-vectors V_{ff}, V_{cn} as shown below :

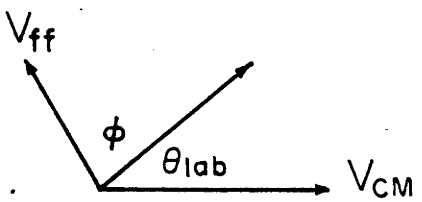

$$V_{ff} = 1.389 \sqrt{\frac{E_{kin}}{A}} \text{ (cm/ns)} ; \quad E_{kin} = 0.1189\, Z^2 A^{-1/3} + 7.3 \text{ (MeV)}$$

Assuming $\frac{d\sigma_{fis}}{d\Omega_{CM}} = \frac{K}{\sin\theta_{CM}}$ the angular integration results in

$$\sigma_{fis} = \pi^2 K$$

Table 4.6 shows the fission cross-sections for different systems and energies. Errors were calculated from statistics. The given energies are mid-target values, calculated from electronic stopping powers [Nor70].

Table 4.6 Fission cross-sections for various systems and bombarding energies.

Systems	E_{lab} (MeV)	σ_{fis} (mb)
^{139}La+	87.9	6.8 ±2.4 10^{-4}
^{19}F	91.9	2.6 ±2.6 10^{-3}
^{159}Tb+	77.9	9.8 ±0.6 10^{-3}
^{19}F	79.9	1.9 ±0.4 10^{-3}
	99.9	5.3 ±0.3
^{169}Tm+	74.9	2.4 ±0.8 10^{-3}
^{19}F	77.9	2.9 ±0.3 10^{-2}
	91.9	7.2 ±0.6
^{181}Ta+	74.8	4.9 ±1.4 10^{-3}
^{19}F	79.8	3.5 ±0.3 10^{-1}
	99.9	180 ±6
^{150}Sm+	79.9	2.4 ±0.5 10^{-3}
^{18}O	81.9	7.9 ±1.3 10^{-3}
	84.9	1.6 ±0.2 10^{-2}
^{124}Sn+	223	0.23 ±0.06
^{58}Ni	228	1.5 ±0.3
	233	6.5 ±0.9
	238	22 ±3.5
	248	79 ±8
^{176}Hf+	76	1 ±0.3
^{16}O	90	85 ±25
^{180}Hf+ ^{16}O	90	29 ±10

CHAPTER 5
DATA ANALYSIS AND DISCUSSION

The data analysis, discussed in this chapter will be mainly concentrated on the problem of determining the angular momentum distribution (L-distribution) of the compound nucleus (C.N.) formed in heavy-ion fusion reactions. The C.N. L-distribution cannot be measured directly. Presently available experimental methods, e.g. gamma-ray multiplicities and elastic scattering measurements, all require some physical model to extract the L-distribution from the data. Therefore the approach has been adopted to apply various experimental techniques and analysing methods to obtain information about the C.N. L-distribution in different ways. Consistency between the results of different methods may then lead to more reliable information about the distributions, while any differences may help to reveal the limitations of the methods employed.

First the generalized-elastic and elastic scattering data will be analysed to obtain nuclear interaction potentials from which reaction cross-section L-distributions are calculated. In section 5.2 the evaporation residues cross-sections, measured at beam-energies near and below the Coulomb-barrier, are used to extract partial fusion cross-section distributions with the help of several fusion models. A comparison between the results of different approaches is made. The analysis of the gamma-ray multiplicity data is given in section 5.3. The measured sub-barrier fusion cross-sections for the tungsten and hafnium isotopes are discussed in relation to hexadecapole deformation effects in section 5.4. In section 5.5 the various L-distributions are used as input for fission cross-section calculations, the results of which are compared with experimental fission cross-sections. A discussion and conclusion follows in section 5.6.

5.1 ELASTIC SCATTERING AND SPIN DISTRIBUTIONS

5.1.1 COUPLED-CHANNELS ANALYSIS

The partial reaction cross-section distribution $\sigma_R(L)$, which describes the incident partial waves absorbed from the elastic channel, may directly be obtained from optical model analysis of the elastic scattering angular distribution. The reaction cross-section L-distribution may be written as :

$$\sigma_R(L) = \pi\lambda^2(2L+1)(1-|S_L|^2) \qquad (5.1.1)$$

where λ is the reduced asymptotic wavelength and S_L is the partial elastic-scattering matrix. Strictly the standard optical model (O.M.) method may only be applied to pure

elastic scattering from a spherical target-nucleus. All projectile-target systems studied here are deformed and the generalized elastic scattering cross-sections are essentially the sum of elastic and inelastic scattering cross-sections. To deal with this problem we will first study the $^{150}Sm+^{18}O$ system, for which pure elastic and inelastic scattering cross-sections have been measured, and we will try to establish how the presence of inelastic scattering affects the partial cross-section distribution.

To this effect optical model calculations with the coupled channels computer code ECIS [Ray72] were performed, including couplings between the elastic channel and the 2^+ and 4^+ excited state channels of ^{150}Sm. In the optical model calculations real and imaginary nuclear potentials of the Woods-Saxon form were used :

$$U(r) = -V f_r(r) - iW f_i(r) \qquad (5.1.2a)$$

$$f_{r,i}(r) = \frac{1}{1 + \exp\left\{ \frac{r-R_{r,i}}{a_{r,i}} \right\}} \qquad (5.1.2b)$$

The radius of the deformed nucleus, expanded in spherical harmonic functions $Y_{L0}(\theta)$ may be written as :

$$R_{r,i}(\theta) = r_{r,i}(A_p^{1/3} + A_t^{1/3})(1 + \beta_2^N Y_{20}(\theta) + \beta_2^N Y_{40}(\theta)) \qquad (5.1.3)$$

where β_2,β_4 are the quadrupole and hexadecapole deformation parameters respectively, which are adjustable paarameters in the fits to the data.

The Coulomb potential used, was one of a deformed uniformly charged spheroid with radius :

$$R_C(\theta) = r_0 A_t^{1/3} (1 + \beta_2^C Y_{20}(\theta) + \beta_4^C Y_{40}(\theta)) \quad r_0=1.2 \text{ (fm)} \qquad (5.1.4)$$

The excited states in ^{150}Sm were treated as pure collective model rotational states for which the transition-strength form-factors were calculated from the derivative of the Coulomb and nuclear potentials multiplied with respectively the Coulomb and nuclear deformation-lengths $\beta^C R_t$, $\beta^N R_t$. Because of the long range Coulomb force, partial waves up to L_{max}=300 ($\hbar$) were considered in the calculations. Increasing L_{max} beyond this value

did not noticably change the results.

The parameter search was started with initial values from Stokstad et al. [Sto81], who performed coupled channels analyses for the systems $^{148,152}Sm+^{16}O$. The sensitivity to each parameter was investigated by changing its value and noting the effect. It was found that the calculated angular distribution, $d\sigma_{el}/d\sigma_{Ruth}(\theta)$,was particularly insensitive to changes in the depth of the imaginary potential. In reference [Gle75] this has been explained as a result of the deep penetration of the projectile into the nuclear medium, once the Coulomb-barrier has been overcome. The projectile traverses a long path-length in the medium and suffers strong attenuation from the elastic channel, almost independent of the depth of the imaginary potential. Angular distributions were most sensitive to changes in the radius and diffuseness of the potentials.

Simultaneous fits to the angular distributions of $d\sigma_{el}/d\sigma_{Ruth}(\theta)$, $d\sigma_{2^+}(\theta)/d\Omega$ and $d\sigma_{4^+}(\theta)/d\Omega$ for E_{beam}=75,80,90 and 100 MeV are shown in fig. 5.1. The potential and deformation parameters as well as the integrated cross-sections are listed in table 5.1. The nuclear potentials and deformation parameters are identical for all energies except for the imaginary potential depth W, which increased from 20 MeV to 30 MeV for E_{beam}= 90 and 100 MeV.

Table 5.1 Optical model Woods-Saxon potential parameters, deformation parameters β_2^C,β_4^C (of the charge distribution in the target-nucleus); deformation parameters β_2^N,β_4^N (of the nuclear potential) and reaction channel cross-sections obtained from the ECIS coupled channels calculations for $^{150}Sm+^{18}O$. r_r=r_i=1.34 (fm); a_r=0.57 (fm); a_i=0.36 (fm); β_2^C=0.18; β_4^C=0.05; β_2^N =0.12; β_4^N =0.033 for all energies.

	(MeV)		(mb)		
E_{lab}	V	W	σ_{2^+}	σ_{4^+}	σ_R
75	20	20	904	37	1498
80	20	20	834	32	1663
90	20	30	720	25	1980
100	20	30	628	20	2225

A destructive interference minimum in $d\sigma_{2^+}(\theta)/d\Omega$ near the angle for which $d\sigma_{el}/d\sigma_{Ruth}$ has a maximum, which has been observed for the scattering of ^{16}O from ^{58}Ni,^{88}Sr and ^{142}Nd [Chi73], is very weak in the $^{18}O+^{150}Sm$ data. The Coulomb-nuclear interference is apparently washed out by the transfer channels for this system.

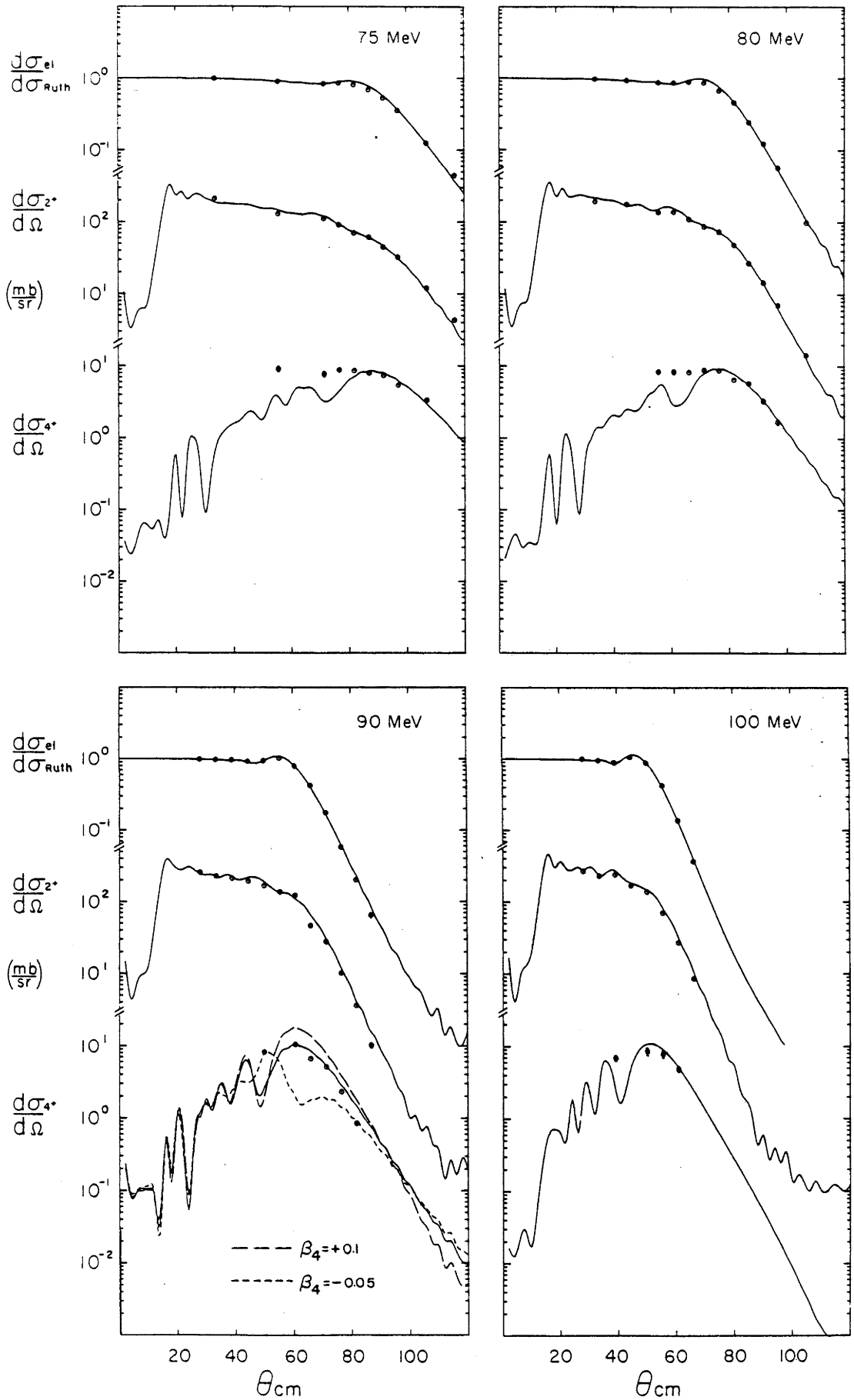

Fig. 5.1 Fits to elastic and inelastic scattering angular distributions with the ECIS coupled-channels program for the reaction $^{150}Sm+^{18}O$ at different bombarding energies.

The calculated $d\sigma_{4^+}(\theta)/d\Omega$ distributions show some disagreement with experimental values at smaller angles. Similar behavior was noticed by Stokstad et. al. for the scattering of 72 MeV. ^{16}O from ^{148}Sm. They explain this as due to contributions from excitation to the unresolved 3^- state of ^{148}Sm. The 3^- state in ^{150}Sm is at much higher energy, but there may be contributions from the second 0^+ state, which is only 30 keV. lower in energy than the 4^+ state.

From the scattering matrices provided by the ECIS program, partial cross-section distributions were calculated for the 2^+ and 4^+ channels with :

$$\sigma_C(L) = \pi\lambda\!\!\!^{-2}\,(2L+1)\,|S_L^{(C)}|^2 \qquad (5.1.5)$$

and for the reduced reaction cross-section with:

$$\sigma_R(L) = \pi\lambda\!\!\!^{-2}\,(2L+1)(1 - \sum_c |S_L^{(C)}|^2) \qquad (5.1.6)$$

where summation index c refers to the 0^+,2^+ and 4^+ channels.

Figure 5.2 shows the 2^+-channel and reduced reaction cross-section L-distributions for different bombarding energies. Most of the 2^+ excitation occurs in collisions with high relative angular momentum, which in classical parlance means at large impact parameter. The observed 2^+ excitation cross-section is therefore predominantly due to Coulomb excitation. The shoulder of the distribution for the 2^+-channel at lower L-values comes from nuclear excitation and is more pronounced at the higher bombarding energies. Its relatively small contribution may explain the weak interference minimum in $d\sigma_{2^+}(\theta)/d\Omega$, mentioned earlier. The 4^+-channel cross-section comes mainly from nuclear excitation, but also shows a long Coulomb excitation tail (fig. 5.4).

It may be concluded that in this case most of the inelastic scattering cross-section is due to the Coulomb potential. Furthermore the excitation energy is rather small compared to the incident particle energy (<1%). The particle trajectories therefore, are little affected by the excitation process.

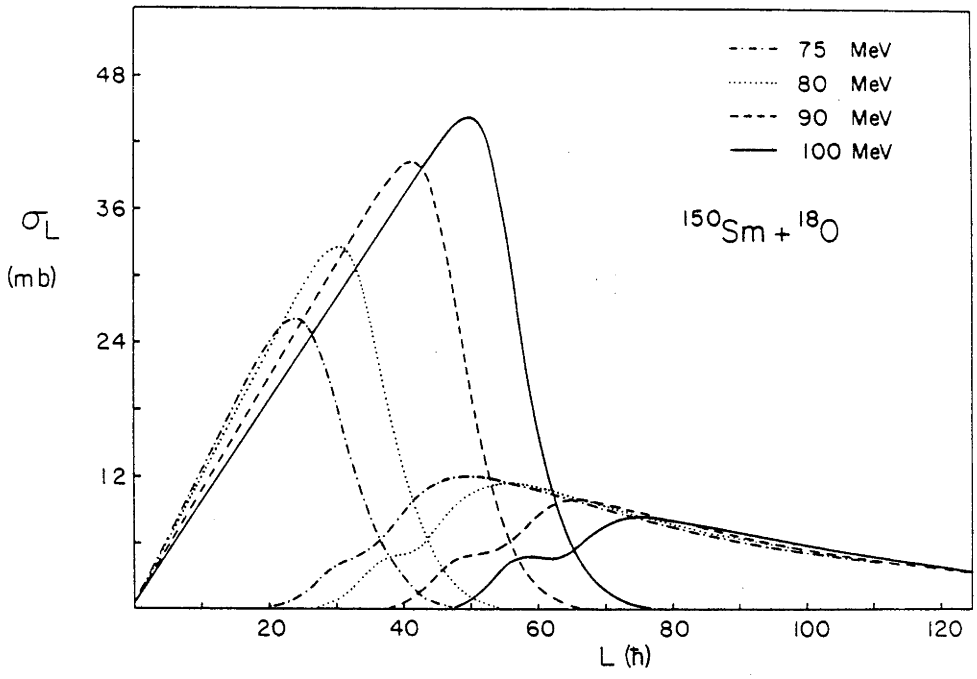

Fig. 5.2 Partial reduced reaction cross-section distributions and partial cross-section distributions for the 2^+ ^{150}Sm excited state channel as defined in the text.

Noting this we treated the inelastic and elastic scattering as the same and performed a standard optical model analysis to $d\sigma_{(el+2^+)}(\theta)/d\Omega$. For this purpose the least squares O.M. computer program "Sophie" [Rob83] was used with spherical nuclear potentials of the Woods-Saxon form :

$$U = -V\, f(r) - W\, f(r) \qquad (5.1.7)$$

with $f(r) = [1+\exp\{(r-R)/a\}]^{-1}$

and $R = r_n(A_p^{1/3} + A_t^{1/3})$

and a Coulomb potential of a sphere with uniform charge distribution :

$$V_C = \begin{cases} \dfrac{Z_p Z_t}{r} e^2 & r > R_C \\ \dfrac{Z_p Z_t}{2R_C} e^2 (3 - r^2/R_C^2) & r \le R_C \end{cases} \qquad (5.1.8)$$

with $R_C = r_0(A_p^{1/3} + A_t^{1/3})$ r_0=1.2 (fm)

Since in this approach the Coulomb excitation flux is added back into the elastic channel a smaller number of partial waves, L_{max} = 100 (ħ), was needed. In the nuclear potential parameter search the geometry of real and imaginary potentials are kept the same, which left four parameters to vary V,W,r_n,a. Fits to the experimental angular distributions are shown in figure 5.3 The potential parameters found, together with the reduced reaction cross-sections are given in table 5.2 (indicated with an asterix).

Fig. 5.4 shows a comparison between the partial cross-section distributions from both analysing methods for 90 MeV bombarding energy. The difference in reduced reaction cross-section is about 5% and is due to a difference in fitting procedure. The standard O.M. calculations were performed with an automatic least squares search routine whereas in the coupled-channels calculations the parameters were changed by hand till good agreement with the experimental data was obtained. Apart from the difference in total cross-sections the distributions look remarkably similar. Similar results were reported [Oes79] for the scattering of ^{32}S from ^{130}Te, however, they obtained identical total cross-sections with both methods.

Differences in shape between distributions are more clearly demonstrated in fig.5.5, where the difference between L-values (ΔL) from each distribution for the same transmission coefficient T_L=1-$|S_L|^2$ are shown as a function of T_L. Distributions with identical shapes show a constant value for ΔL for $T_L < 1$. The ΔL-value between the distributions from O.M. and C.C. calculations is nearly constant in the range $0.1 < T_L < 0.9$ for all bombarding energies. The sudden rise for $T_L < 0.1$ is probably due to Coulomb-excitation to the 4^+-state. Absorption from the elastic channel by Coulomb-excitation cannot be described correctly with the standard O.M. short-range imaginary potential.

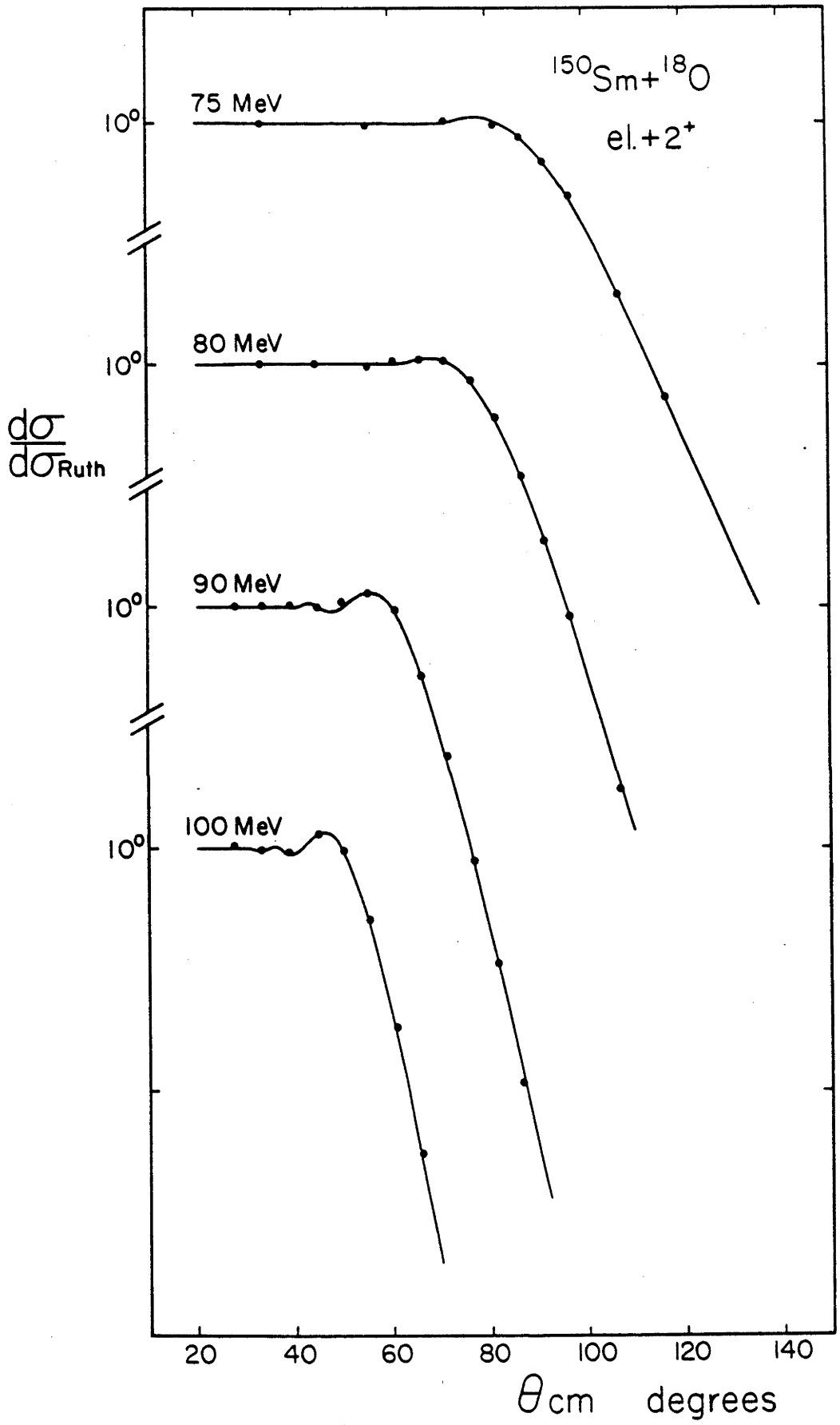

Fig. 5.3 Standard optical model fits to angular distributions of the sum of elastic and 2^+ ^{150}Sm excited state yields.

Table 5.2 Nuclear Woods-Saxon potential parameters obtained from standard O.M. fits to generalized elastic scattering angular distributions with computer-code "Sophie". The geometry of real and imaginary potentials are kept identical.

		(MeV)			(fm)		(mb)
Reactions		Elab	V	W	R	a	σ_R
^{150}Sm+		70	13.1	26.7	1.305	0.512	390
^{18}O	*	75	16.5	17.2	1.350	0.475	695
	*	80	11.7	11.4	1.350	0.543	958
		80	10.1	11.8	1.374	0.565	1081
	*	90	17.8	13.2	1.345	0.501	1329
		90	15.2	13.7	1.325	0.553	1334
	*	100	14.8	12.5	1.345	0.529	1676
^{139}La+	**	80	17.6	29.2	1.308	0.442	583
^{19}F	**	90	21.2	29.5	1.312	0.430	1003
	**	100	18.1	24.2	1.308	0.463	1342
^{159}Tb+		80	10.6	31.7	1.300	0.500	318
^{19}F		90	13.5	28.5	1.317	0.510	868
		100	18.3	19.3	1.331	0.490	1209
		110	20.1	18.6	1.329	0.485	1701
^{169}Tm+		80	4.1	39.2	1.301	0.500	163
^{19}F		90	12.2	30.6	1.302	0.500	642
		100	16.8	26.6	1.314	0.490	1081
^{181}Ta+		90	6.6	18.8	1.318	0.529	494
^{19}F		100	9.0	21.2	1.323	0.501	936
		110	14.3	22.4	1.325	0.490	1319

*) Fits to $d\sigma_{(el.+2^+)}(\theta)/d\sigma_{Ruth.}$

**) Fits to quasi-elastic scattering data including all inelastic scattering and neutron transfer cross-sections.

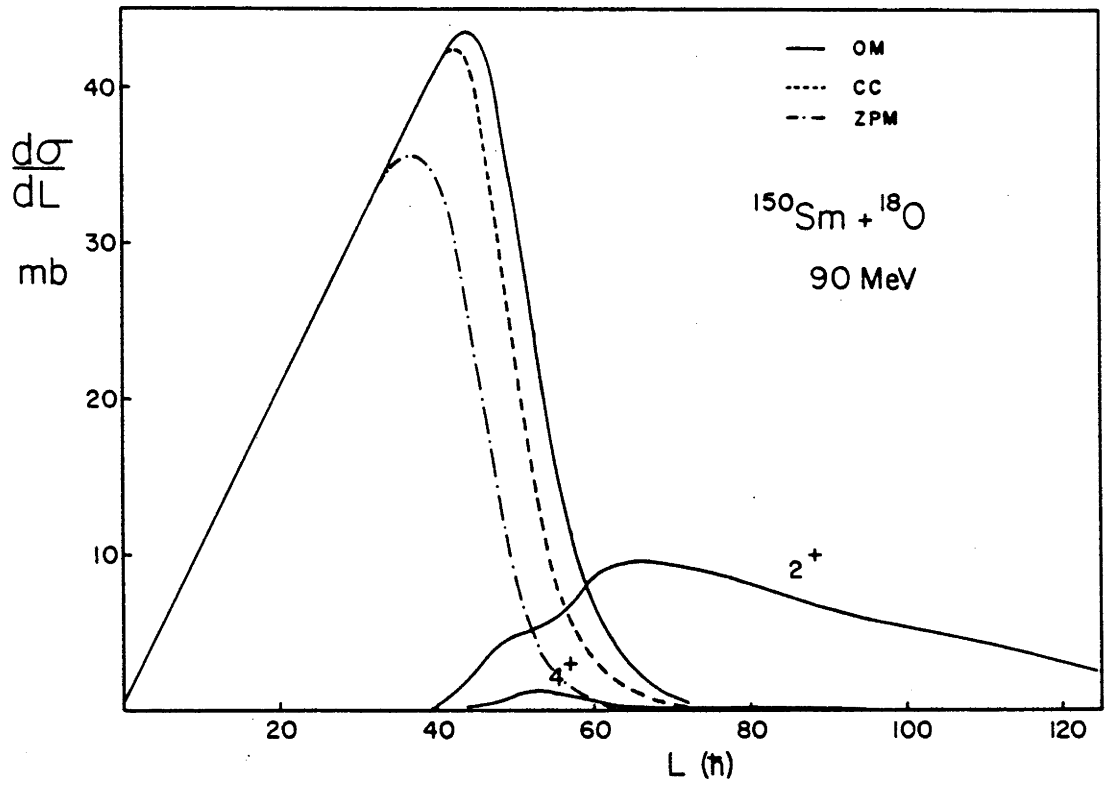

Fig. 5.4 Comparison of reduced reaction cross-section distributions from coupled-channels (CC) and standard optical model (OM) analysis for $^{150}Sm+^{18}O$ at 90 MeV. The dash-dot line shows the partial fusion cross-section distribution as predicted by the ZPM fusion model.

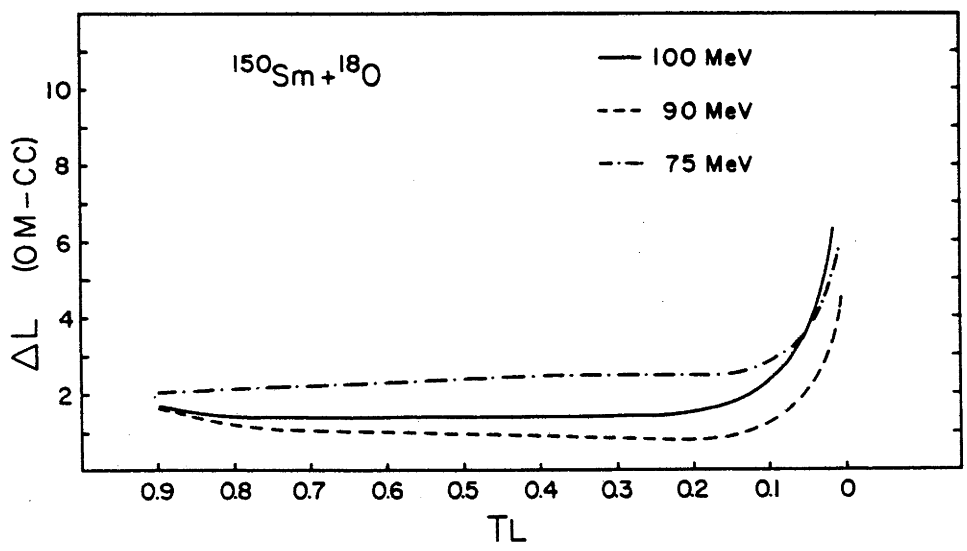

Fig. 5.5 Comparison of the diffuseness in the T_L distributions from standard optical model and coupled-channels analysis. For further explanation see text.

5.1.2 ANGULAR MOMENTUM-DISTRIBUTIONS FROM THE STANDARD OPTICAL MODEL ANALYSIS

Noting the similarity in shape of the L-distributions obtained with C.C. and standard O.M. analysis for $^{150}Sm+^{18}O$ the generalized elastic scattering angular distributions presented in the previous chapter were also analysed with the standard O.M. method. Least squares O.M. program "Sophie" was used with the Coulomb and nuclear potential form-factors given in (5.1.7 and 5.1.8). Generally good agreement between experimental and calculated angular distributions was obtained as can be seen in fig. 5.6. The potential parameters and the reaction cross-sections are given in table 5.2. For all systems the angular distributions $d\sigma_{el}/d\sigma_{Ruth}(\theta)$ show Fresnel-type diffraction patterns, which is characteristic for nuclear scattering in the presence of a strong repulsive Coulomb field. The ratio $d\sigma_{el}/d\sigma_{Ruth}$ is unity for small angles, then rises slightly (~ 10% at the highest energies) after which it drops to very low values without any oscillations. The lack of diffraction oscillations in the falling slope indicates that the scattering function S_L is smooth. A sharp cut-off parametrization of S_L results in Fraunhofer diffraction oscillations as was demonstrated by Blair [Bla57].

Strong interaction radii were calculated with the quarter point method [Zuc60], which uses the angle θ_c for which $d\sigma/d\sigma_{Ruth}(\theta_c) = 1/4$. This angle was substituted in equation (2.1.6) of chapter 2 to obtain the strong interaction radius R_c. The strong interaction radius was also calculated from the relation $L_c(L_c+1) = kR_c(kR_c - 2n)$ [Fri72] where L_c is the angular momentum for which $T_L = 1/2$ and n is the Sommerfeld parameter defined in chapter 2 eq. (2.1.2). Table 5.3 shows the results for both methods. For 80 MeV $^{169}Tm+^{19}F$ the quarter point method could not be used because $d\sigma_{el}/d\sigma_{Ruth}(\theta)$ did not get below 1/4.

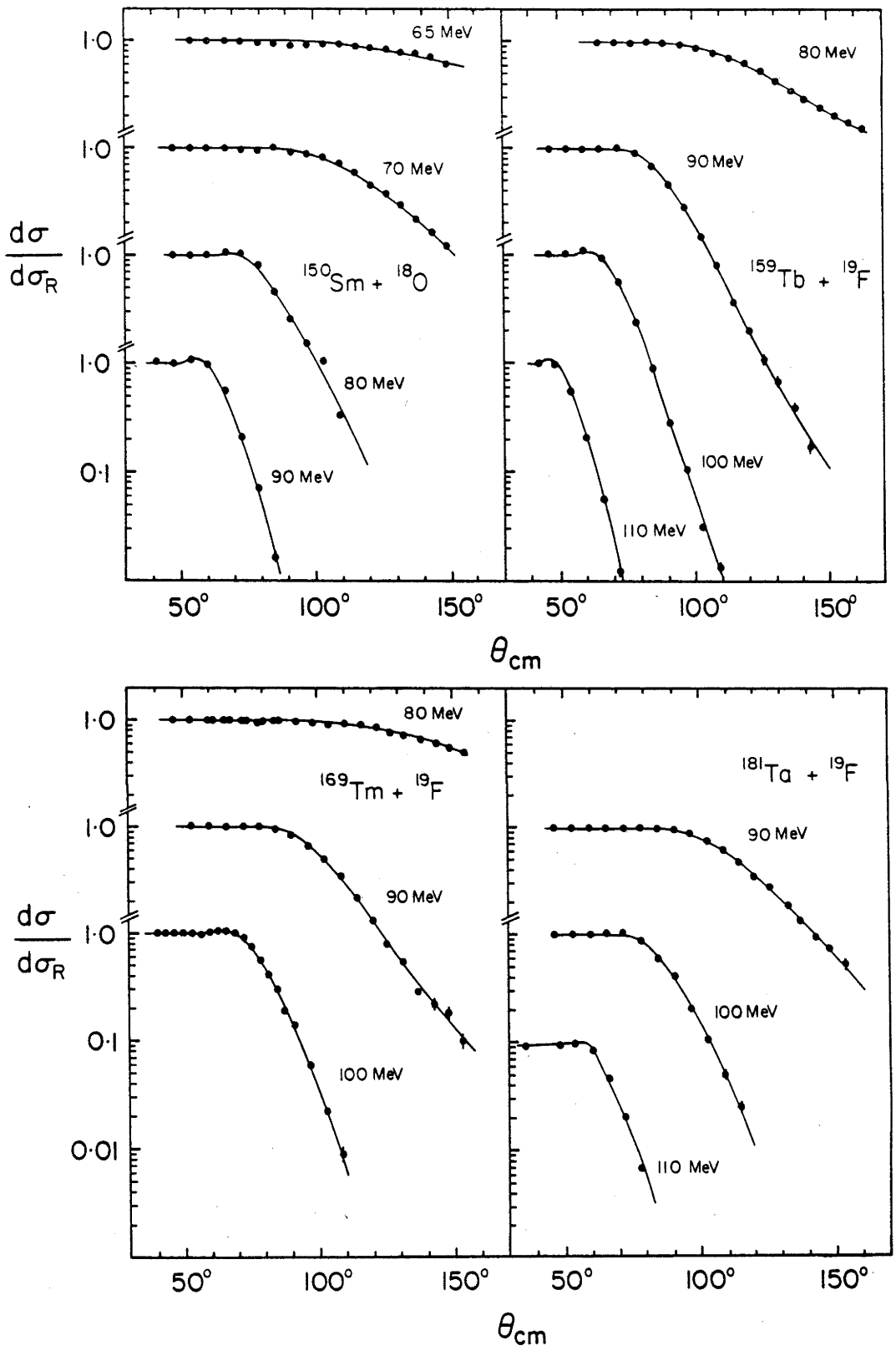

Fig. 5.6 Least squares fits to the generalized elastic scattering angular distributions with the standard optical model.

Table 5.3 Strong absorption radii calculated from the centre of mass angle for which $d\sigma/d\sigma_{Ruth} = 1/4$ (quarter point method (q.p.)) and from the angular momentum for which $T_L = 1/2$.

Systems	E (MeV)	R_c (fm) (q.p.)	R_c (fm) (T_L=1/2)	Systems	E (MeV)	R_c (fm) (q.p.)	R_c (fm) (T_L=1/2)
^{159}Tb+	80	12.0	12.4	^{169}Tm+	80		12.5
^{19}F	90	12.1	12.4	^{19}F	90	12.1	12.5
	100	12.1	12.3		100	12.2	12.4
^{150}Sm	70	11.8	12.2	^{181}Ta	90	12.2	12.6
^{18}O	80	12.3	12.5	^{19}F	100	12.2	12.6
	90	12.0	12.1		110	12.3	12.6

The strong interaction radius changes very little with energy and is very similar for the different systems.

Reaction cross-section L-distributions were calculated for all systems from (5.1.1) with S_L-matrices from the least-squares O.M. fits. The similarity in shape of the distributions for ^{150}Sm+^{18}O from C.C. (ECIS) calculations and standard O.M. analysis of generalized elastic scattering data, shown in fig. 5.5, was not a feature of the specific choice of optical model potentials. This was checked by fitting the generalized elastic scattering angular distributions with least squares calculations leaving all nuclear potential parameters free to vary. The resulting fits are essentially identical to the ones shown in fig. 5.6, whereas the potential parameters are very different. In fig. 5.7 the real and imaginary potentials, obtained with different parameter constraints, are shown for fits to 90 MeV ^{19}F scattering from ^{159}Tb. Although very different at small radii, the potentials are similar in the tail of the distribution. The radius at which the potentials become identical is near to the strong absorption radius R_c=12.1 (fm) from table 5.3. It shows the insensitivity of elastic scattering to the interior of the potential. Many more potentials could be found with identical tails, which describe the angular distributions of elastic scattering equally well.

The reaction cross-section L-distributions, calculated from both potentials, are also nearly identical. It has been shown [Fer70] for optical model potentials which describe elastic scattering of 42 MeV alpha particles by ^{42}Ca that both the real and imaginary values of S_L remain constant for a real well depth variation from 50 MeV to 220 MeV.

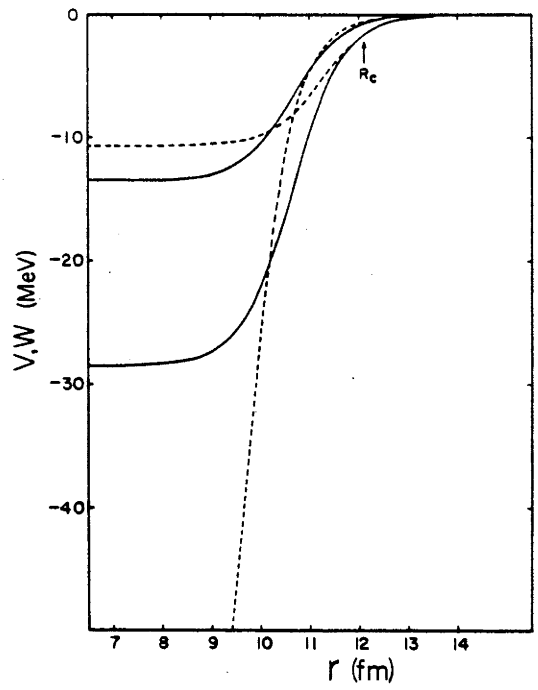

Fig. 5.7 Optical model nuclear potentials obtained from fitting the experimental data with different parameter constraints (see text).

Thus the reaction cross-section L-distribution does not depend on the choice of potential, as long as the elastic scattering angular distribution is correctly reproduced.

Heavy-ion elastic scattering data has been successfully analysed for a number of systems with the S_L-matrix and phase-shift function parametrised by a Fermi-distribution [McI60]. The reaction cross-section L-distribution, which is directly related to S_L, may therefore also be parametrised by means of a Fermi-function :

$$\sigma_R(L) = \pi\lambda\!\!\!^{-2}\,(2L+1)[1+\exp\{(L-L_0)/\delta\}]^{-1} \qquad (5.1.9)$$

where δ is the diffuseness parameter, which determines the falling slope of the distribution and L_0 is the grazing angular momentum, which determines the total integrated cross-section. In table 5.4 the δ-parameters are given, which substituted in (5.1.9) reproduced the $\sigma_R(L)$ distributions from the O.M. analysis. The diffuseness of the reaction cross-section L-distribution increases as the bombarding energy approaches the Coulomb barrier. It should be noted that for energies close to the Coulomb barrier the transmission coefficient $T_{L=0} < 1$ and the Fermi function cannot be used in this form. Multiplying the distribution with a constant T_0 may solve this problem.

Table 5.4 Diffuseness parameters δ from Fermi-function parametrisation of the transmission coefficients T_L obtained from elastic scattering O.M. analysis.

System		E(MeV)	δ(ħ)	System	E(MeV)	δ(ħ)
^{150}Sm+		65	5.4	^{159}Tb+	80	5.8
^{18}O		70	4.9	^{19}F	90	4.4
	*	75	3.5		100	3.5
	*	80	3.6	^{169}Tm+	80	6.0
		80	3.7	^{19}F	90	4.8
	*	90	3.2		100	3.9
		90	3.4			
	*	100	3.2	^{181}Ta+	90	5.4
^{139}La+	**	80	3.8	^{19}F	100	4.2
^{19}F	**	90	3.1		110	3.9
	**	100	3.1	***	109	3.8
				***	125	3.7

*) From O.M. analysis of $d\sigma_{(el.+2^+)}/d\Omega$

**) From quasi-elastic scattering data, including all inelastic scattering and neutron transfer cross-sections.

***) Quasi-elastic scattering data from [Hin82].

5.2 SPIN DISTRIBUTIONS FROM FUSION MODELS

It is a well established fact, that heavy-ion fusion cross-sections at bombarding energies near and below the classical fusion barrier, are substantially higher than predicted by O.M. or conventional fusion-model calculations. Over the last decade a number of fusion models have been developed to explain the sub-barrier fusion enhancement. Some of these models employ the semi-classical barrier penetration method and use global properties of the nuclei such as surface vibration [Esb81] or surface-deformation [Won73] [Sto81]. Introduction of these surface effects give rise to multiple fusion barriers. The averaging of barrier transmission coefficients T_L with appropriate weight functions leads to an increase in the fusion cross-section at sub-fusion barrier energies. Through the calculation of barrier penetration coefficients for each incoming partial wave, this method provides directly the partial fusion cross-section distribution.

Other fusion models are based on direct reaction theory such as the coupled channels method [Rho80],[Das83] and the "elastic fusion" model [Uda85]. In the coupled channels approach sub-barrier fusion enhancement is obtained from channel-coupling. The effect of channel coupling on the fusion barrier is explained in chapter 2 and in [Bro83]. In principle

this method may give the correct fusion cross-section distribution provided all relevant reaction channels are taken into account and described correctly. However, for most systems this is impracticable due to the many reaction-channels involved and the complexity of the problem.

In the following partial fusion cross-section distributions will be calculated using the zero-point motion model of Esbensen and the "elastic fusion" model of Udagawa et al.

5.2.1 ZERO-POINT MOTION FUSION-MODEL CALCULATIONS

The zero-point motion (Z.P.M.) fusion model, described in chapter 2, was used to calculate partial fusion cross-section distributions for different projectile-target systems. The calculations included the effects of quadrupole and octupole vibrations (deformations) in the target-nucleus as well as quadrupole deformations in the projectile. The nuclear potentials of the Bass-model [Bas77] were used. They reproduce experimental fusion cross-sections with reasonable accuracy (<10%) at energies well above the fusion-barrier for a large range of projectile-target systems .The effective potential for the relative radial motion of projectile and target nuclei may then be written as :

$$V_{eff}(r) = Z_p Z_t e^2 [r^{-1} + 3/5\, r^{-3}(s_{t2}R_t + s_{p2}R_p) + 3/7\, s_{t3}R^2_t r^{-4}] + \hbar^2 L(L+1)(2\mu r^2)^{-1} - V_n(r-s) \qquad (5.2.1)$$

$$V_n(r) = -\frac{R_p R_t}{R_p + R_t}[H_1 \exp(d/d_1) + H_2 \exp(d/d_2)]^{-1} \qquad (5.2.2)$$

$d = r - R_t - R_p - \Delta R$; $R_{p,t} = 1.16\, A_{p,t}^{1/3} - 1.39\, A_{p,t}^{-1/3}$

$H_1 = 0.0300$ MeV^{-1} fm ; $H_2 = 0.0061$ MeV^{-1} fm ; $d_1 = 3.33$ fm ;

$d_2 = 0.65$ fm.

The quantities s_{t2}, s_{p2}, s_{t3} are the variations of the surface-surface distance due to quadrupole and octupole Z.P.M. in the surfaces of the target-nucleus and projectile ($s = s_{t2}+s_{t3}+s_{p2}$).

Parameter ΔR was adjusted to match experimental fusion cross-sections at energies well

above the barrier, where the ZPM had no significant effect on the total fusion cross-section.

For each incident partial wave the average transmission coefficient $T_L^{(av)}$ for barrier penetration was calculated by averaging with respect to the s_{t2},s_{t3} and s_{p2} variations :

$$T_L^{(av)} = \langle T_L(E,L,s_{t2},s_{t3},s_{p2}) \rangle \qquad (5.2.3)$$

Transmission coefficients $T_L(E,L,s_{t2},s_{t3},s_{p2})$ were calculated using the W.K.B. approximation for quantum mechanical tunnelling :

$$T_L = [1 + \exp(x_L)]^{-1} \qquad (5.2.4a)$$

$$x_L = 2 \int_{r_1}^{r_2} dr \sqrt{\frac{2\mu}{\hbar^2} \{V_{eff}(r) - E\}} \qquad (E < V_L^{max}) \qquad (5.2.4b)$$

where $V_{eff}(r)$ is the effective potential given in (5.2.1) , μ is the reduced mass and r_1,r_2 are the classical turning points. Whenever $V_{eff}^{max} < E$ the transmission coefficient was calculated from the Hill-Wheeler parabolic barrier approximation [Hil53]

$$T_L = \frac{1}{1 + \exp\left\{ \frac{2\pi}{\hbar\omega_L} [V_{eff}^{max} - E] \right\}} \qquad (5.2.5)$$

with $$\omega_L = \frac{1}{\mu} \frac{\partial^2 V_{eff}}{\partial r^2} (r,L,s) \Big|_{r_B}$$

Different from the usual approximation made : $\omega_L = \omega_0$, ω_L was calculated for every

L-value by numerical differentiation. The value of ω_L changed typically (for $^{169}Tm+^{19}F$) from ω_0=4.0 to ω_{45}=4.4. The effect on T_L due to this change was, however, largely compensated by the reduction in r_B from $r_B(L=0)$=11.3 (fm) to $r_B(L=45)$=10.8 (fm). The $\omega_L=\omega_0$ and $r_B(L=0)=r_B(L)$ approximations result in about 5% higher fusion cross-sections.

To reduce computation time the same approximations were made as in [Esb81]. The effect of zero-point motion was converted into an effective angular momentum by replacing r by r+s in equation (5.2.1). This leads to :

$$V_{eff}(r) = \frac{Z_p Z_t}{r} e^2 + \frac{L_{eff}^2}{2\mu r^2} - \frac{V_0}{1 + \exp[(r-R_1-R_2-\Delta R)/a]} \qquad (5.2.6)$$

$$\text{with} \quad L_{eff}^2 = \hbar^2 L(L+1) \frac{r}{(r+s)^2} - 2\mu Z_p Z_t e^2 \left[\frac{r}{r+s} s + \frac{3}{5} \frac{r^2}{(r+s)^3} \{s_{p2}R_p + s_{t2}R_t\} \right.$$

$$\left. - \frac{3}{7} \frac{r}{(r+s)^4} s_{t3} R_t^2 \right] \qquad (5.2.7)$$

Furthermore, the radius r in (5.2.7) was approximated with the C.M. distance r_B at the barrier obtained from (5.2.6) with $L_{eff}^2=\hbar^2L(L+1)$. Radius r_B was calculated for every L-value. The transmission coefficients T_L were calculated for L_{eff}^2 from -500 to 10000 and stored in an array. Transmission coefficients called for by the averaging (integration) routine were obtained by calculating the appropriate L_{eff}^2 -value and subsequently referencing in the array. For non-integer L_{eff}^2 -values linear interpolation was applied.
These approximations resulted in a reduction of C.P.U. computer time from 1.5 hours to 10 minutes. The approximations made, did not noticably change the partial cross-section distributions nor the total fusion cross-sections.

The standard deviations of the Gaussian weight-functions, used in (5.2.3) were calculated from (2.4.13) ; (2.4.14) (chapter 2). These equations may directly be used for even mass-number nuclei, which have zero ground-state spin. For the odd-A nuclei, involved in this work, the rotational model was used to evaluate the intrinsic quadrupole moment Q_0, which is related to the B(E2)-value by :

$$B(E2;J_iK_i \mid J_fK_f) = \frac{5}{16\pi} e^2 Q_0^2 \langle J_iK_i\lambda \mid J_fK_f\rangle^2 \qquad (5.2.8)$$

where J_i,J_f are the initial and final spins and K_i,K_f the projections on the nuclear symmetry-axis. The quantity $<J_iK_i\lambda \mid J_fK_f>$ is the Clebsch-Gordon spin coupling factor.The BE2-value of the equivalent even mass nucleus was then extracted, using the same equation (5.2.8) with the Clebsch-Gordon equal to unity. It was assumed that $K_i=K_f=J_i$

The standard deviations were in some cases calculated from the deformation parameter β_2 with :

$$\sigma_2 = r_0 A^{1/3} \frac{\beta_2}{\sqrt{4\pi}} \qquad (5.2.9)$$

The B(Eλ) , β_2-values as well as the standard deviations are listed in table 5.5 .

Table 5.5 Parameters used in the ZPM calculations. The last column contains the ΔR values needed to get agreement between the calculated and measured fusion cross-sections at energies high above the fusion barrier.

Nucleus	Transition (E2)	B(E2) (W.u.) or ($e^2\beta^2$)	Q_0 (fm)	σ_2 (fm)	BE3 (W.u.)	σ_3 (fm)	ΔR (fm)
^{18}O	$2^+\rightarrow0^+$	3.3 W.u.[1]		0.33			
^{19}F	$3/2^+\rightarrow1/2^+$	(β_2=0.50[2])		0.45			
^{139}La				0.17[3]		0.24[3]	0.1
^{150}Sm	$2^+\rightarrow0^+$	55. W.u.[1]	3.67	0.34	31[5]	0.26	0.2
^{159}Tb	$5/2^+\rightarrow3/2^+$	2.8[4]	7.07	0.62	19[6]	0.19	0.0
^{169}Tm	$5/2^+\rightarrow1/2^+$	3.4[4]	7.62	0.62	6[7]	0.1	0.1
^{181}Ta	$9/2^+\rightarrow7/2^+$	2.0[2]	6.75	0.52	6[7]	0.1	0.1

1) [End79],[End81].
2) [Ajz83].
3) Deduced from even mass neighbour nuclei ^{138}Ba,^{140}Ce. [Ley72],[Ecc66].
4) [Lob70].
5) [Boh75] page 577. [Vej68].
6) Deduced from even mass neighbour nuclei ^{158}Gd,^{160}Dy. [McG81],[Oeh74].
7) [Elb69]

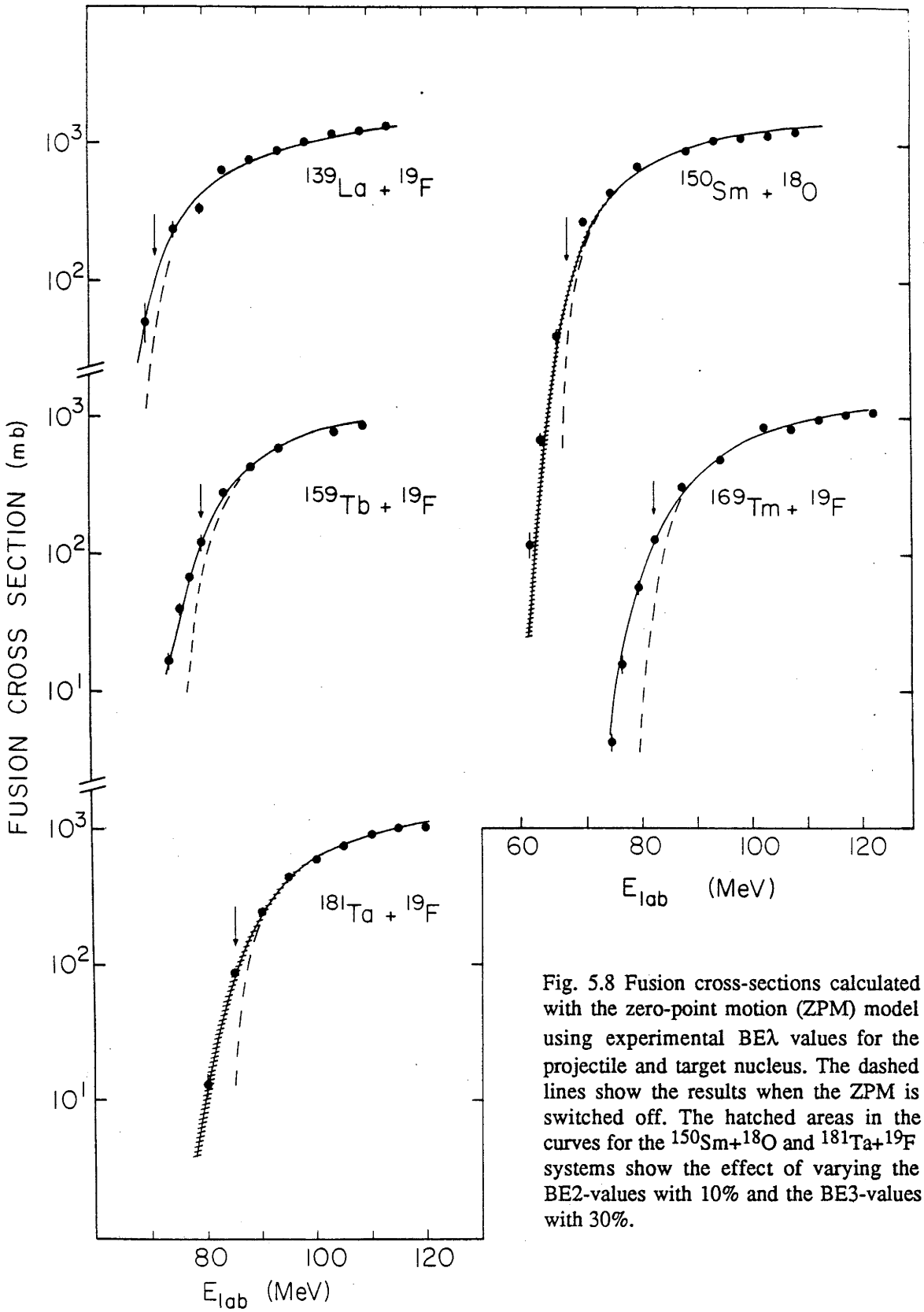

Fig. 5.8 Fusion cross-sections calculated with the zero-point motion (ZPM) model using experimental BEλ values for the projectile and target nucleus. The dashed lines show the results when the ZPM is switched off. The hatched areas in the curves for the $^{150}Sm+^{18}O$ and $^{181}Ta+^{19}F$ systems show the effect of varying the BE2-values with 10% and the BE3-values with 30%.

Averaging of $T_L(E,L,s_{t2},s_{t3},s_{p2})$ was performed over three standard deviations, which covered 99.7% of the integrated Gaussian distribution. Figure 5.8 shows the fusion excitation functions calculated with the Z.P.M. model (solid lines), together with experimental fusion cross-sections for several projectile-target systems. Experimental cross-sections at energies above the fusion-barrier were taken from [Cha86]. The dashed lines show the results when the Z.P.M. is turned off. Arrows in the figures indicate the classical fusion-barriers obtained with the Bass-model potential. The ΔR parameters, adjusted to match experimental cross-sections at higher energies, are given in table 5.5. For all systems the Z.P.M. gives considerable sub-barrier fusion cross-section enhancement and reproduces the experimental cross-sections quite well.

Since the model is rather successful in reproducing the experimental fusion cross-sections over a wide energy range, we will now examine the predicted partial fusion cross-section distributions. The effect of Z.P.M. on the spin distribution is demonstrated in fig. 5.9 for $^{150}Sm+^{18}O$ at 90 MeV energy. Distributions are shown for no vibrations, quadrupole vibrations in the target-nucleus only, quadrupole and octupole vibrations in the target-nucleus, and in addition quadrupole vibrations in the projectile as well.

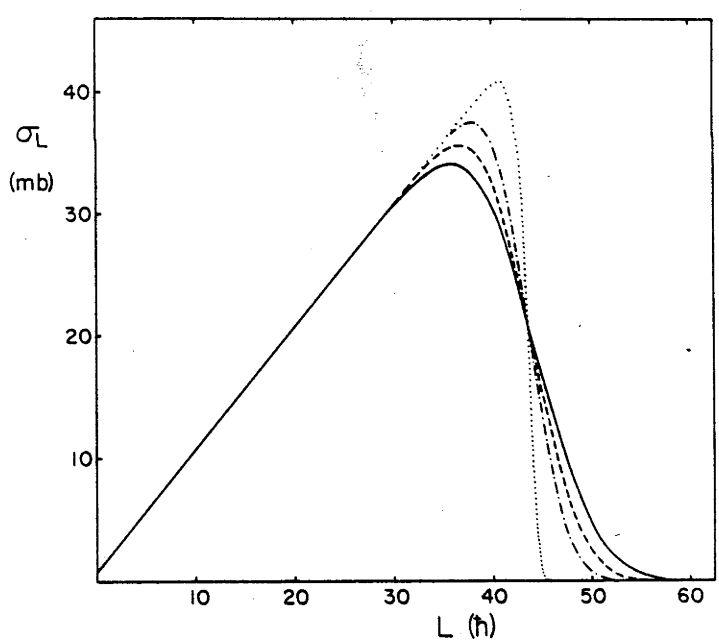

Fig. 5.9 The effect of zero-point motion on the partial fusion cross-section distribution. The different curves represent: ZPM swithched-off (dots); quadrupole vibrations in the target-nucleus only (dash-dot); quadrupole and octupole vibrations in the target nucleus (dashed); quadrupole vibrations in the projectile as well (solid line).

In fig. 5.4 the Z.P.M. distribution is shown for the $^{150}Sm+^{18}O$ at 90 MeV compared to the distribution from ECIS coupled-channels calculations and the result from

the standard optical model method. A detailed comparison of the $T_L^{(av)}$-distributions from the Z.P.M. calculations with

$$T_L = 1 - \sum_C |S_L^{(C)}|^2 \qquad (5.2.10)$$

from the ECIS model calculations (fig 5.10) shows a nearly constant value of ΔL over the range $0.1<T_L<0.9$ for all energies.

The shapes of the distributions obtained from elastic scattering and Z.P.M. fusion model calculations are almost identical for the $^{150}Sm+^{18}O$ system. To compare the diffusenesses of the distributions from O.M. analysis and ZPM calculations for all systems the Fermi-function parametrisation was used to calculate δ of equation (5.1.9).

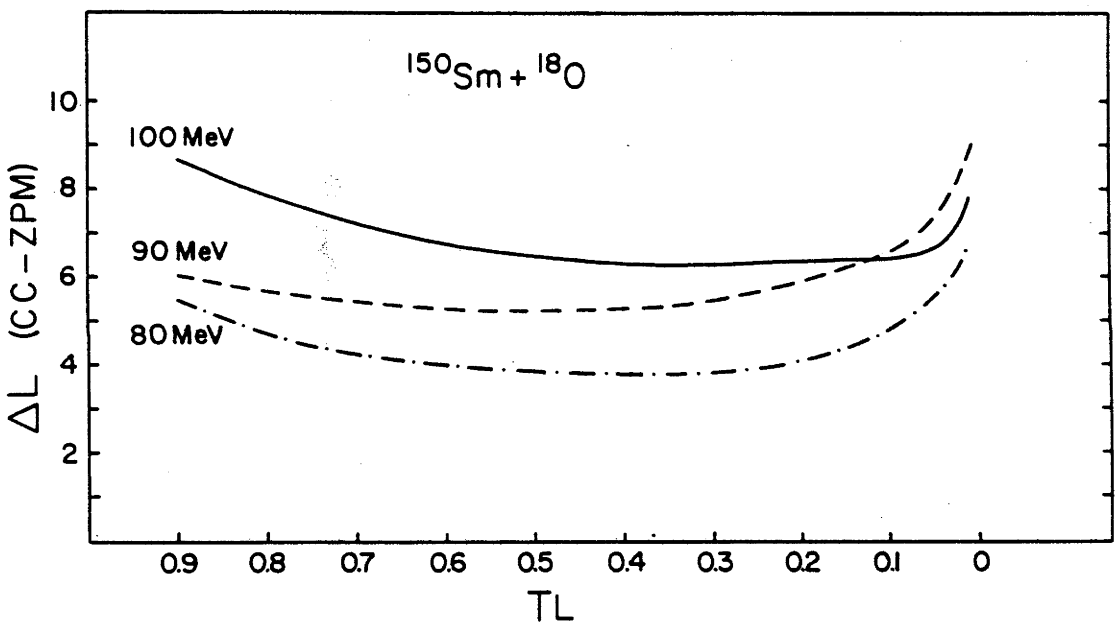

Fig. 5.10 Comparison of the diffuseness in the T_L-distribution predicted by the coupled-channels analysis and the ZPM fusion calculations for the reaction $^{150}Sm+^{18}O$ at different energies.

This was done by substituting $T_{L1}=0.2\ T_{L0}$ and $T_{L2}=0.8\ T_{L0}$ and the values L_0, L_1, L_2 in eq. (5.1.9) to solve δ. Figure 5.11 shows the δ-values obtained as a function of $(E_{CM} - V_b)/A_{CN}$, where Vb is the s-wave fusion barrier-height. A comparison between shapes from standard O.M. analysis of generalized elastic scattering data and from Z.P.M. calculations for the different systems at energies for which $(E_{CM}-V_B)/A_{CN}$ is approximately the same, are shown in fig. 5.12. The ΔL-values for $T_L=1/2$ were set equal

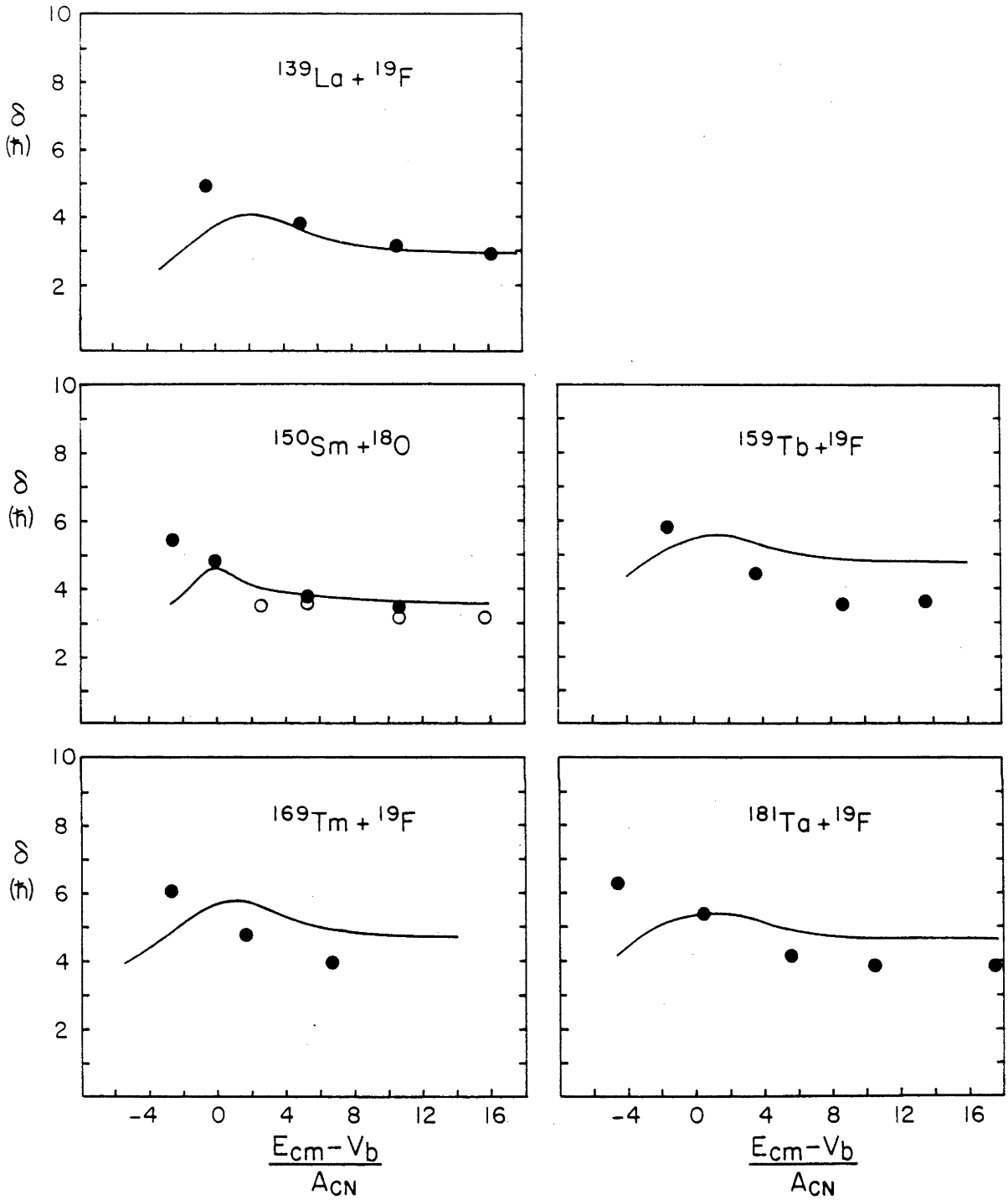

Fig. 5.11 Diffuseness parameter δ (defined in the text) as a function of $(E_{cm}-V_b)/A_{CN}$ for various systems.

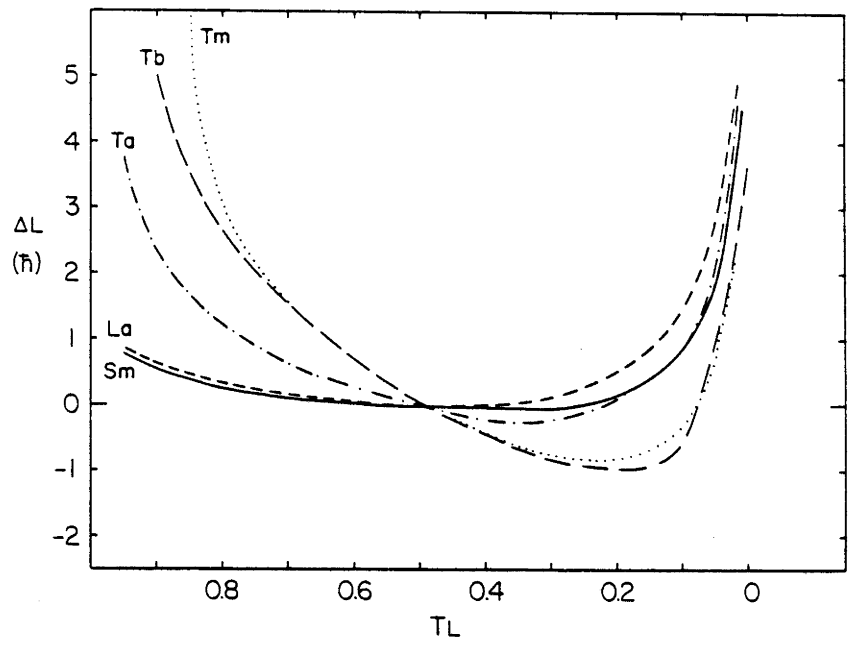

Fig. 5.12 Comparison of the diffuseness in the T_L-distribution predicted by the standard optical model and the ZPM fusion model calculations for various systems.

The ΔL-values for T_L=1/2 were set equal to zero. There is excellent agreement for $^{150}Sm+^{18}O$ and $^{139}La+^{19}F$, which are the systems with smallest deformations. For the other systems the deviations get progressively worse with increasing deformation.

The use of a Gaussian weight-function in the Z.P.M. calculations is based on a harmonic oscillator ground-state wave function. The ^{139}La and ^{150}Sm target-nuclei are least deformed thus come closest to a vibrational nucleus. If it is assumed that the distributions from elastic scattering data reflect the nuclear surface deformations or vibrations, then the ZPM-distributions of the least deformed systems should agree best with the OM-distributions. Differences between the L-distributions may also be associated with the role of direct reactions. The reaction cross-section distribution from elastic scattering O.M. analysis contains contributions from particle-transfer and inelastic scattering reactions as well as fusion. Most of the inelastic scattering cross-section was removed by subtracting σ_2+(L) and σ_4+(L) from σ_R(L) in the coupled channels analysis of $^{150}Sm+^{18}O$. In a less correct way the inelastic scattering was removed from the reaction cross-section for all other systems by treating elastic and inelastic scattering as the same. This may be approximately valid if most of the inelastic scattering is due to Coulomb excitation. However, it should be kept in mind that for strong nuclear excitation the particle orbits may change dramatically, in which case the correspondence between entrance channel angular momentum and exit channel scattering angle is less clear. The target-nuclei

of the systems studied here all have very low first excited states, which favours Coulomb over nuclear excitation. Particle transfer cross-sections are also included in the reaction cross-section from elastic scattering O.M. analysis.

Measured proton transfer and estimated direct reaction cross-sections for different systems and energies are listed in table 5.6. In the last two columns the percentage fractions relative to the the reduced reaction cross-section σ_{React} is given. Direct reaction cross-sections were estimated from : $\sigma_{D.R.} = \sigma_{React} - \sigma_{fus}$ where σ_{React} is the reduced reaction cross-section obtained from quasi-elastic scattering O.M. analysis. The direct reaction cross-section as a fraction of the total reaction cross-section increases as the energy decreases and is considerable for all systems. The proton transfer cross-section however is much smaller for $^{150}Sm+^{18}O$ and to a lesser extent for $^{139}La+^{19}F$ than for all other systems.

Table 5.6 One proton stripping and estimated direct reaction cross-sections as ratios to σ_{React} for different systems, indicating the relative importance of direct reaction processes in determining the fusion partial cross-section distribution. How $\sigma_{D.R.}$ has been estimated is explained in the text.

System	(MeV) Elab	(mb) $\sigma_{1pr.str.}$	(mb) σ_{React}	(mb) σ_{fus}	$\frac{\sigma_{1pr.str.}}{\sigma_{React}}$	$\frac{\sigma_{D.R.}}{\sigma_{React}}$
$^{150}Sm+$	70	7.5	390	281 ±20	2%	31%
^{18}O	80	19	924	700 ±40	2%	24%
	90	21	1333	94 ±55	1.6%	29%
$^{139}La+$	80	71	582	337 ±30	8%	42%
^{19}F	90	98	1002	778 ±45	10%	22%
$^{159}Tb+$	80	56.5	318	125 ±18	18%	61%
^{19}F	90	96	868	470 ±25	11%	46%
	100	120	1209	736 ±40	10%	39%
$^{169}Tm+$	80	40	163	59 ±8	25%	64%
^{19}F	90	87	642	371 ±25	14%	42%
	100	109	1081	626 ±35	10%	42%
$^{181}Ta+$	90	74	488	246 ±22	15%	50%
^{19}F	100	106	929	600 ±37	11%	35%
	110	117	1319	910 ±48	9%	31%

5.2.2 ELASTIC FUSION MODEL CALCULATIONS

Preferably all direct reaction processes should be incorporated in a coupled channels calculation. This, however, is too complicated for the systems studied here because of the large number of reaction channels and the complexity of the particle transfer processes, due to the many particle-states involved.

From semi-classical considerations of particle transfer in heavy-ion reactions, the partial wave distribution is expected to peak near the grazing angular momentum (L_c). The particle transfer spin distribution is however not always symmetrical. In particular when the bombarding energy approaches the Coulomb barrier the depletion of the transfer-channel due to the onset of fusion is much reduced, which has already been demonstrated in fig.4.6 of chapter 4. This results in a reduction of the low partial waves of the fusion spin-distribution. A proper description of the particle transfer process is therefore important to evaluate the correct fusion spin distribution. As mentioned earlier, including transfer channels in a coupled channels calculation is too complicated for deformed systems. A simpler method, which accounts for the direct reaction channels has been proposed by Udagawa et al. [Uda85]. In their so called "elastic fusion" model the fusion cross-section is calculated using the distorted wave function and absorptive nuclear potential from elastic scattering optical model analysis. The fusion transmission coefficients are given by :

$$T_L = \frac{8}{\hbar v} \int_0^{R_F} | \chi(r) |^2 W(r)\, dr \qquad (5.2.11)$$

where v, $\chi(r)$ and W(r) are the relative velocity, the distorted wave function and the imaginary part of the optical potential, respectively. The cut-off radius R_F, which divides the imaginary potential into fusion and direct reaction contributions is given by :

$$R_F = r_F (A_p^{1/3} + A_t^{1/3}) \qquad (5.2.12)$$

For substantial direct reaction contributions, the use of such a cut-off radius leads inevitably to fusion transmission coefficients significantly less than unity even for low angular momenta.

Optical model potentials from table 5.2 were used to fit the experimental fusion cross-sections. For each system the potential of one energy was used to reproduce the fusion cross-section for that energy by adjusting r_F. The same potential and r_F-value were then used for all other energies of the same system. Figure 5.13 shows the fits obtained.

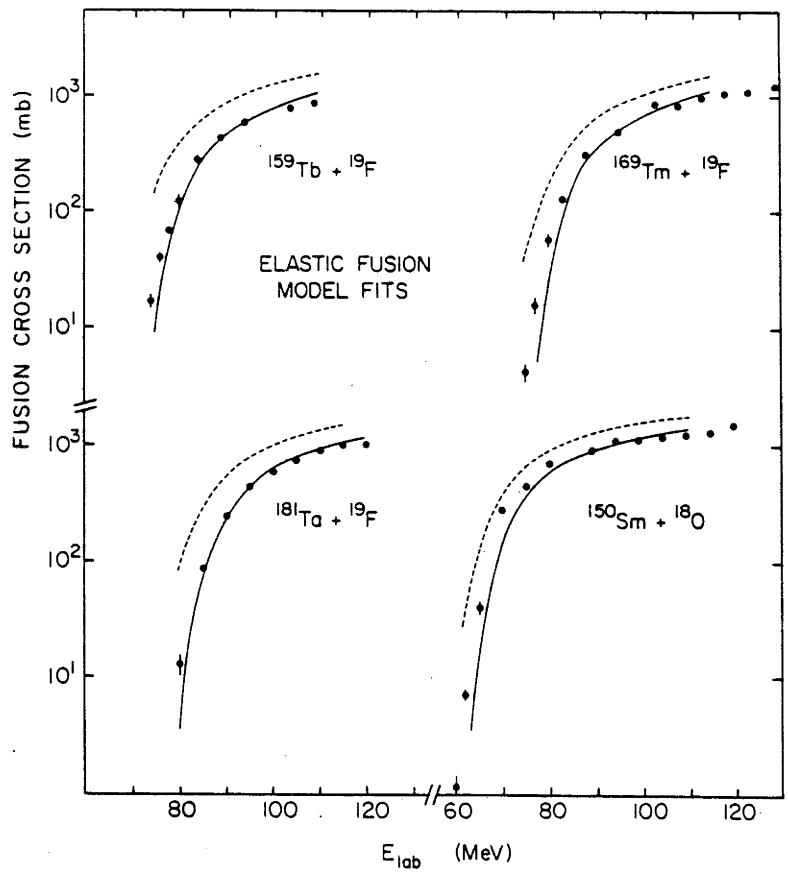

Fig. 5.13 Fits to the experimental fusion cross-sections with the elastic-fusion model. The dashed lines show the reaction cross-sections from elastic scattering.

For most systems it was not possible to get good agreement with a single value for r_F. Using a different potential parameter set (from a different energy) gave generally the same results.

It is possible that this failure to reproduce the experimental data is due to the fact that the optical potentials are obtained from generalized elastic scattering data. However, also for the pure elastic scattering data of $^{150}Sm+^{18}O$ it was not possible to get agreement. In chapter 2 it was shown that also for the system $^{152}Sm+^{16}O$ no good fit could be obtained with a single value for r_F. Udagawa et al. ascribed this to channel coupling effects.

For comparison of angular momentum distributions the r_F parameter was adjusted for each energy individually, to obtain the experimental fusion cross-sections. Figure 5.14 shows the fusion spin distributions for $^{159}Tb+^{19}F$ together with reduced reaction cross-section distributions using the Fermi function parametrisation. The essential difference between the distributions is the reduction in the low partial wave cross-sections,

even for energies well above the fusion-barrier. According to the "elastic fusion" model small impact parameter collisions at energies above the fusion barrier do not nescessarily lead to fusion.

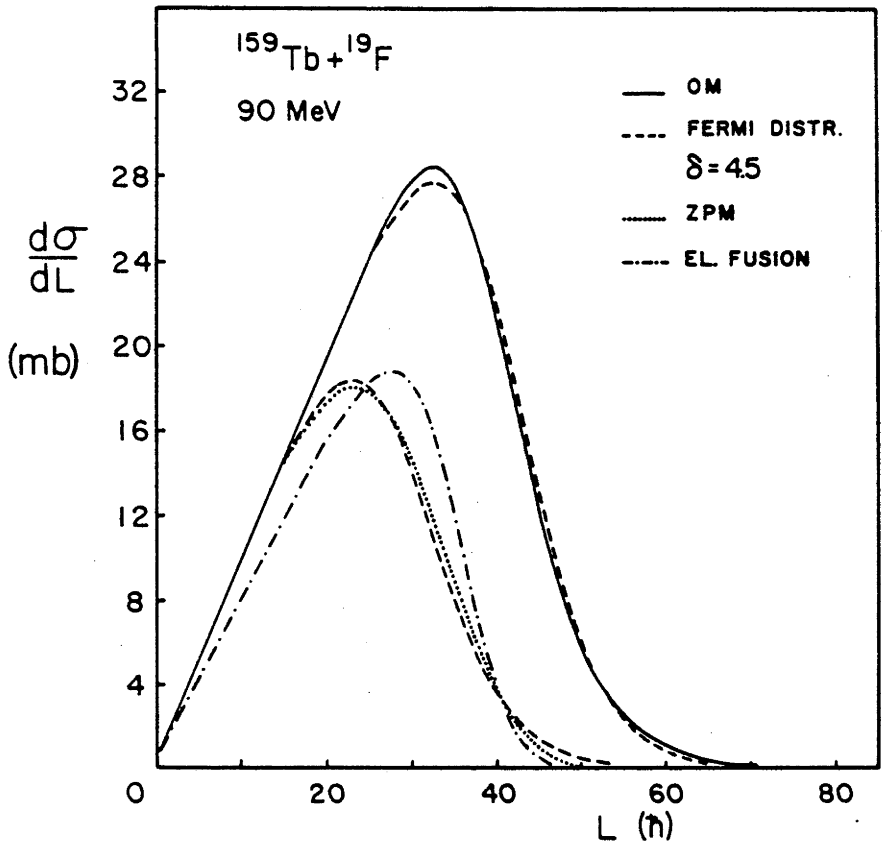

Fig. 5.14 Comparison of the angular momentum distributions obtained from the OM,ZPM and elastic fusion model calculations for the reaction $^{159}Tb+^{19}F$ at 90 MeV. The reaction cross-section of the OM calculations is reduced to the fusion cross-section with the Fermi-function parametrisation.

Udagawa et al. [Uda85] have shown that for the reactions $^{124}Sn+^{58}Ni \rightarrow ^{182}Pt$ and $^{118}Sn+^{64}Ni \rightarrow ^{182}Pt$, the experimental fusion cross-sections can be reproduced over an energy-range from well above to well below the fusion barrier with a single fusion radius parameter r_F for each reaction. In section 5.5 the fission cross-sections will be calculated for these systems with different CN angular momentum distributions. For this purpose the radii r_I and r_F of the optical model potential were slightly adjusted to correct for a minor error in [Uda85]. Figure 5.15 shows the fits to the experimental fusion cross-sections for the $^{124}Sn+^{58}Ni$ system with the optical model parameters and fusion radii listed in table 5.7 The spin-distribution predicted by the "elastic fusion" model is extremely wide as can be seen from fig. 5.16 in which the distributions are shown from "elastic fusion", Z.P.M.

and sharp cut-off models at E_{cm}=170MeV. The shape of the Z.P.M. distribution was calculated with deformation parameters $\beta_2(^{58}Ni) = 0{,}22$ and $\beta_2(^{124}Sn) = 0.11$.

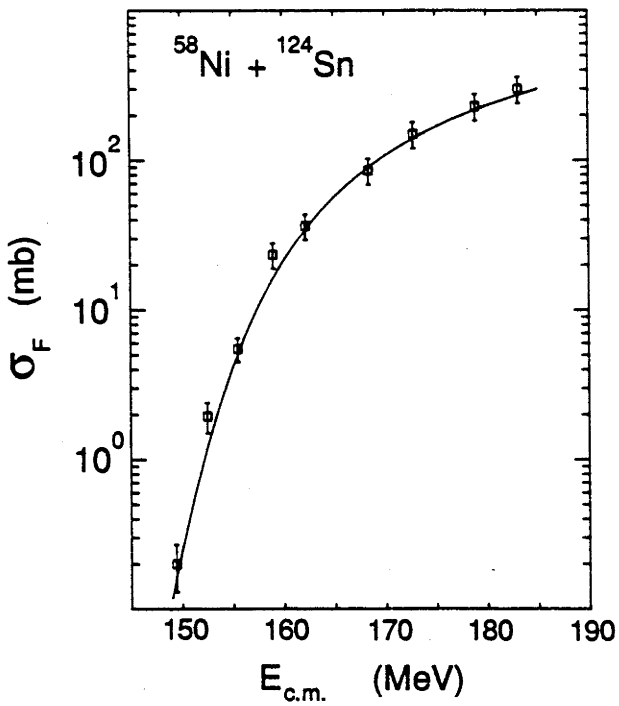

Fig. 5.15 Fit to the experimental fusion cross-sections with the elastic fusion model for the system $^{124}Sn+^{58}Ni$.

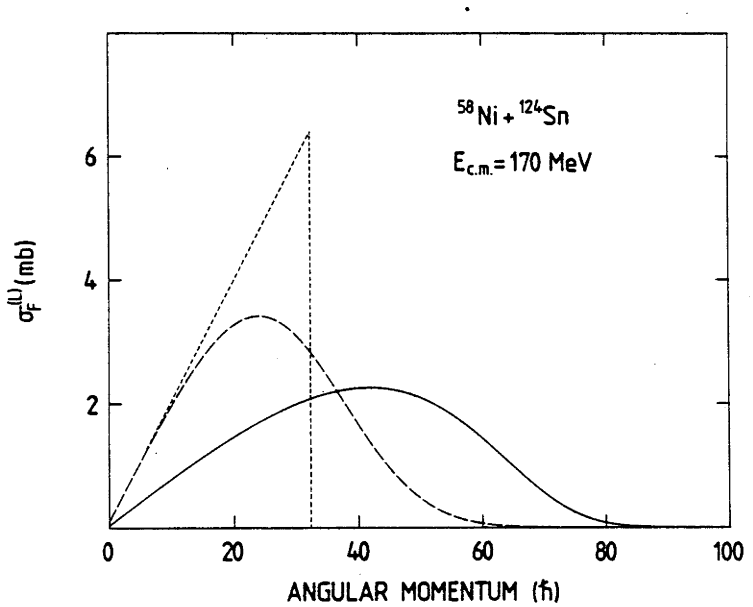

Fig. 5.16 Partial fusion cross-section distributions from the sharp cutt-off model (short-dashed) , ZPM model (dashed) and elastic fusion model (solid line) for the reaction $^{124}Sn+^{58}Ni$ at 170 MeV (CM).

Table 5.7 Optical model (Woods-Saxon) potential parameters used in the fusion cross-section calculations with the elastic fusion model.

Systems	V (MeV)	W (MeV)	r_R (fm)	r_I (fm)	r_C (fm)	a_R (fm)	a_I (fm)	r_F (fm)
$^{58}Ni+^{124}Sn$	58.1	62.9	1.26	1.37	1.26	0.294	0.294	1.435
$^{64}Ni+^{118}Sn$	58.1	62.9	1.26	1.38	1.26	0.294	0.294	1.453

Because the Z.P.M. model-calculations did not reproduce the experimental fusion excitation function, the T_L-distribution was parametrised with an error-function to make the total fusion cross-sections of both spin-distributions identical. An error function parametrisation as defined below reproduces the tail of the Z.P.M. spin-distribution better than a Fermi-function parametrisation. A ΔL-parameter of 16.5 reproduced the ZPM distribution well

$$\sigma_L = \pi\lambda\!\!\!^{-2}(2L+1)\ 1/2\ [1-\mathrm{erf}\{(L-L_0)/\Delta L\}] \qquad (5.2.13)$$

where the error function erf is given by :

$$\mathrm{erf}(x) = \frac{2}{\sqrt{\pi}} \int_0^x \exp(-t^2)\, dt \qquad (5.2.14)$$

Empirically it was found that parameter ΔL may be calculated from the diffuseness parameter δ of the Fermi-distribution ($\Delta L \approx 2.32\ \delta$).
The sharp cut-off distribution was also calculated with the error-function using a very small diffuseness parameter. Which distribution is most appropriate will be discussed in the next section, when these fusion spin-distributions will be used as input for a fission cross-section calculation.

5.3 GAMMA-RAY MULTIPLICITIES AND THE COMPOUND-NUCLEUS ANGULAR MOMENTUM DISTRIBUTION

The analysis of the gamma-ray multiplicity data for the reaction $^{159}Tb+^{19}F$ proceeded as follows. From the for dead-time corrected numbers F(old)-0, F-1, F-2, F-3, F-4, F-5, F-6 and S(ingles) the k-fold probabilities were calculated with : $P_k = F_k/S$.

Before these probalities were converted to the moments of the Fold-distribution a simple correction was made for the angular momentum distribution of the gamma-rays. It was assumed that the angular distribution of the gamma-rays :

$$W(\theta) = A_2 P_2(\cos\theta) + A_4 P_4(\cos\theta) \qquad (5.3.1)$$

varied between $0.25 < A_2 < 0.3$ and $-0.08 < A_4 < -0.05$. The limits for the Lengendre polynomal coefficients A2 and A4 were deduced from discrete line results from a number of (HI,xn) reactions producing $^{172,174,176}W$ [Dra78],[Wal76]. The correction was then to scale the measured solid angle, assuming 4 isotropic statistical gamma-rays. This is not a very accurate correction because if , say, one gamma is detected in one of the NaI detectors it will change the angular distribution of subsequent gamma-rays and so on if 2 or more are detected. To do this calculation correctly (including quantum mechanics) is both difficult and complex.(N.B. one should also take into account the angle of the Germanium detector)

The only justification for the procedure used is that if the initial angular momentum vector is long, then the detection of gamma-rays in the Ge and other NaI detectors will not affect the vector very much and thus not will not change the angular distribution very much either. Neglecting all these other effects, the angular distribution will simply increase (in our case) the probability of detection of the gamma-rays, which corresponds to an effective increase in solid angle.

Calculation of $<m_\gamma>$ and width σ

The moments of the distribution were calculated from the Fold-probabilities P_k by means of a computer program, which used the basic method of Hagemann et al. [Hag75]. Errors were computed for $<m_\gamma>$ and σ, working from the original independent experimental numbers and their errors and taking into account the error in the solid angle (Ω). The error in the skewness was very large and made the value for the skewness meaningless.

Two problems arise, which may affect the results somewhat : 1) uncertainty in F-0 as discussed in chapter 4 section 4.3, poor statistics in F-6 often gave zero. To overcome this to some degree the procedure adopted by Hillis et al. [Hil79] was used. Hillis et al. showed that a relationship could be established (for a given multiplicity m) between 4 successive fold probabilities P_k, P_{k+1}, P_{k+2}, P_{k+3}, the number of detectors and k. Thus it is possible to evaluate P_0 in terms of P_1, P_2 and P_3. This was tested with various shapes of fold distributions and found to be correct to about 1-2% if $<m_\gamma> > 12$. Thus the value of

P_0 calculated by this relationship was compared with that derived experimentally, if the calculated value departed from the experimental one by more than the experimental error, then the experimental value was replaced by the calculated one (after appropriate normalisation). This normally resulted in a significantly larger error for F-0, though a better value. This relationship was also used to estimate P-6, again with appropriate errors. The experimental value of F-6 was usually zero.

Data from the 7.26 cm NaI detector

The 7.26 cm diameter NaI detector was placed at large distance (small solid angle) to reduce the probability of two gamma-rays piling up and to separate the neutrons from the gamma-rays by time of flight. Thus one can measure $<m_\gamma>$ directly from the average gamma-ray detection efficiency $\bar{\varepsilon}$ and the ratio of coincidence to singles rates in the Ge-detector :

$$N_\gamma(\text{coinc.}) = N_\gamma(\text{singles,Ge})\ \Omega\ \bar{\varepsilon}\ (<m_\gamma> -1) \qquad (5.3.2)$$

One gamma-ray, which is detected in the Ge-detector has been subtracted. A correction was made for the angular distribution of gamma-rays. This, however, is very small since at 55° (the angle of the detector) $P_2=0$ and P_4 is very small.

Comparisons of $< m_\gamma >$ from the 7.26 cm NaI-detector and from the multiplicity filter are in reasonable accordance with the errors. In table 5.8 the average multiplicities and widths are given for different xn-channels and energies.

Table 5.8 Average values and widths of the multiplicity distributions for different evaporation residues from the reaction $^{159}Tb+^{19}F$ at different energies.

		80(MeV)	85(MeV)	90(MeV)	100(MeV)	115(MeV)
4n	<m>	11.3 ±0.5	14.1 ±0.6	18.2 ±0.8	22.2 ±1.1	
	σ	4.2 ±0.4	4.7 ±0.5	4.9 ±0.7	5.6 ±2.2	
5n	<m>			11.8 ±0.5	16.4 ±0.7	
	σ			4.4 ±0.4	5.1 ±0.7	
6n	<m>				11.7 ±0.6	20.1±0.9
	σ				3.4 ±1.4	5.9±0.9

Statistical model calculations

To compare the experimentally determined $\langle m_\gamma \rangle$ and σ with the same quantities derived from the ZPM angular momentum distribution the following procedure was used. The angular momentum distribution predicted by the ZPM fusion model was parametrised with a Fermi-function and used as input for a statistical model calculation with the Monte-Carlo code ZPACE. The output angular momentum distributions of the various xn-channels after neutron emission were then parametrised with a skewed Gaussian function :

$$P(L) = N_L \exp\left[-\frac{1}{2} \left\{ \frac{L-L_0}{\sigma_0 (1+\frac{L-L_0}{|L-L_0|}\beta)} \right\}^2 \right] \qquad (5.3.3)$$

The angular momentum L was then converted to m by :

$$m = \frac{L}{2} + 4 + \text{offset} \qquad (5.3.4)$$

It was assumed that on average 4 statistical gamma-rays were emitted and that on average they removed zero angular momentum. The remaining gamma-rays are considered to be from stretched E2 transitions. The offset allows for : 1) average number of detected neutrons. 2) the gamma-rays missed in experiment either by low efficiency or by internal conversion. This varies with the reaction. The offset-values from the neutron and gamma-ray components are listed in table 5.9

Table 5.9 Offset-values used in conversion of multiplicity to angular momentum with equation (5.3.4)

offset	4n	5n	6n
gammas	-0.9	-2.0	-0.8
neutrons	+0.8	+1.0	+1.2
total	-0.1	-1.0	+0.4

Figure 5.18 shows the comparison between experimental $\langle m_\gamma \rangle$,σ and the same parameters calculated with ZPACE for CN angular momentum distributions from the ZPM model and from the sharp cut-off model. The results with the ZPM-distributions are in best agreement with the data, especially for the 4n-channel, which is most sensitive to the high angular momentum components of the CN L-distribution.

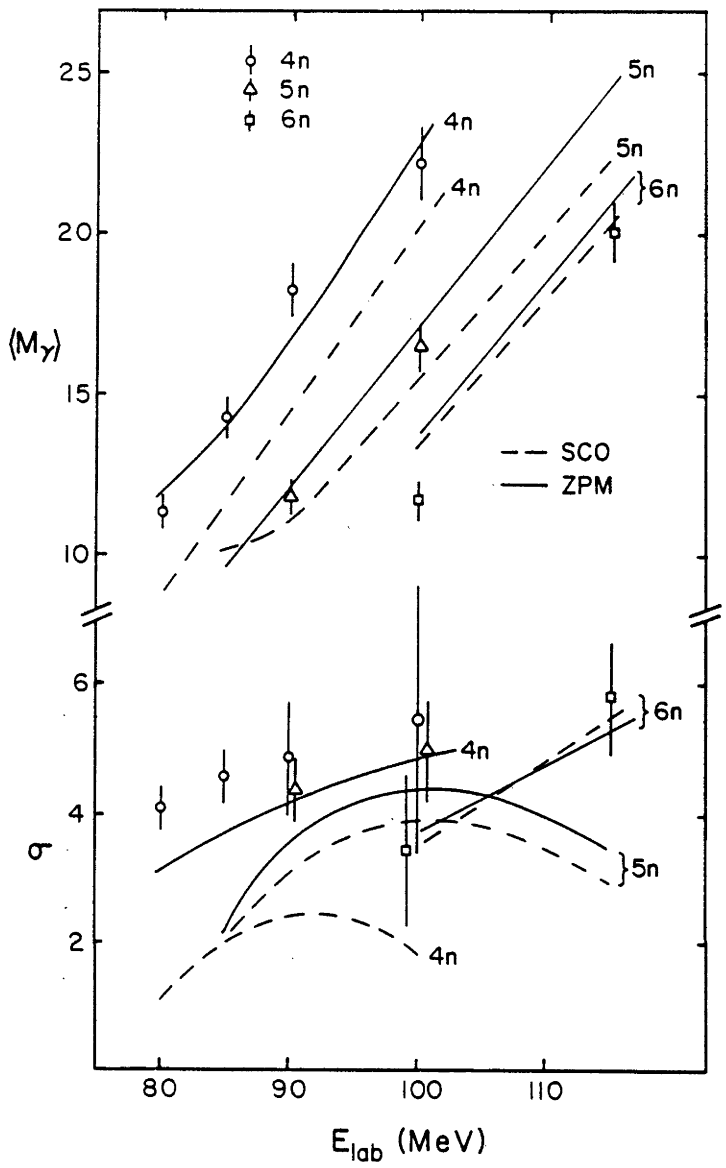

Fig. 5.17 Experimental <m_γ> and σ values of the partial xn cross-section distributions, compared with ZPACE calculations using compound nucleus angular momentum distributions from the sharp cut-off and the ZPM fusion model (parametrised with a Fermi-function).

5.4 HEXADECAPOLE DEFORMATION AND SUB-BARRIER FUSION ENHANCEMENT

Although a coupled channels treatment of the fusion process involving all reaction channels is out of reach for most projectile-target systems, such calculations are very instructive in understanding the significance of different reaction channels in the fusion process. It has been suggested that the large negative hexadecapole deformation,

associated with nuclei with Z~74, would be particularly effective in enhancing fusion [Rho83]. Figure 5.18 shows the experimental fusion cross-sections for the reactions $^{182}W,^{184}W,^{186}W+^{16}O$, as a function of centre of mass energy. Also shown are predictions of standard O.M. (solid line) and coupled channels calculations [Rho84b]. In the standard O.M. calculations, the reaction cross-section for the highest energy was made identical to the experimental fusion cross-section, by adjusting the radius of the imaginary potential. This potential was used for all other energies. The coupled channels calculations included quadrupole and hexadecapole deformations of the target-nucleus. The quadrupole deformation gives most enhancement. Including the hexadecapole deformation brings the calculated curve nearer to the experimental points. However the cross-sections for the three isotopes are very similar.

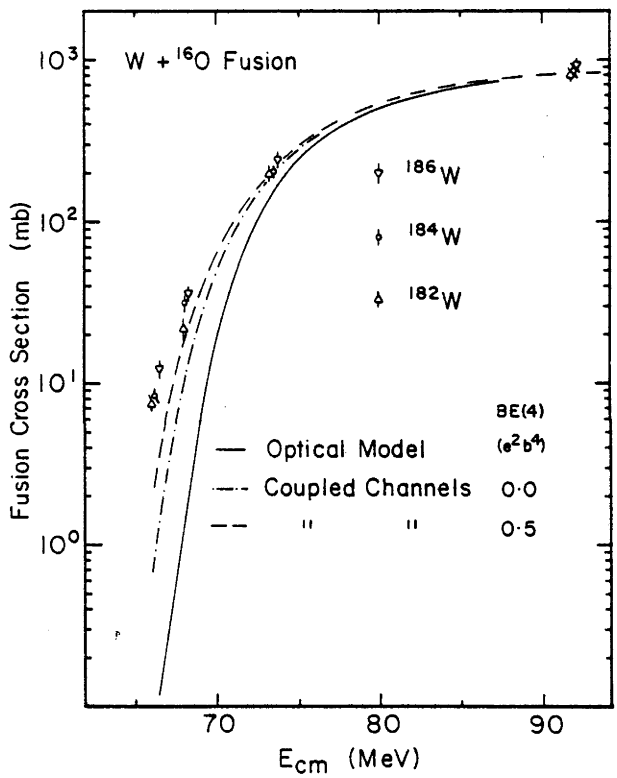

Fig. 5.18 Experimental fusion cross-sections for the reactions $^{182,184,186}W+^{16}O$ and coupled-channels calculations showing the effect of the quadrupole and hexadecapole deformations on the sub-barrier fusion cross-sections.

Table 5.10 gives the β_2 and β_4 deformations parameters, which were calculated [Göt72] with the Strutinsky renormalisation method [Str67],[Str68]. It shows that similar hexadecapole deformations are predicted by theory for the three tungsten isotopes. Figure 5.19 demonstrates that the similarity between fusion cross-sections for different isotopes is not an artefact of the way total fusion cross-sections were extracted from the E.R. angular distributions. It shows the measured partial E.R. cross-sections

for each isotope at different angles on the same scale.

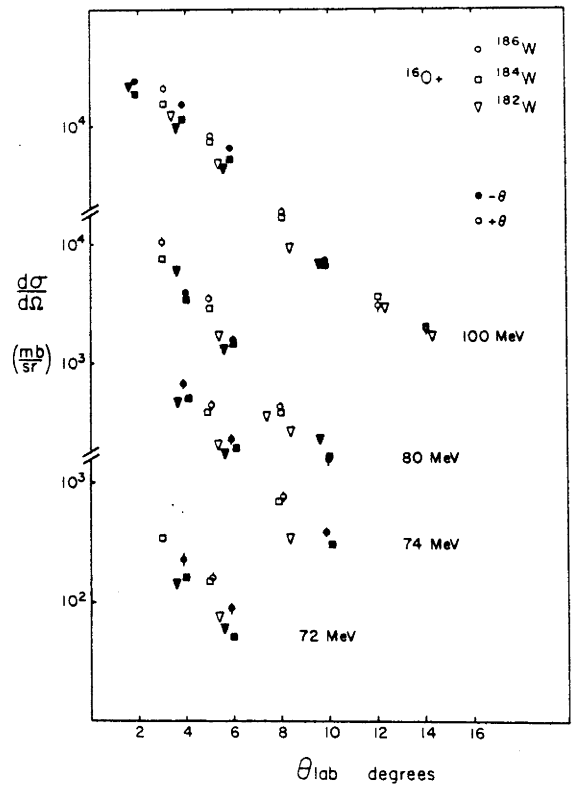

Fig. 5.19 Evaporation residue angular distributions for the reactions $^{182,184,186}W+^{16}O$.

The slight differences between cross-sections of the isotopes is well be accounted for by the difference in centre of mass energy as can be seen in fig. 5.18.

However, the Hf-isotopes are predicted to have different hexadecapole deformations (table 5.10) Figure 5.20 shows the experimental fusion excitation functions for $^{176}Hf,^{180}Hf+^{16}O$.

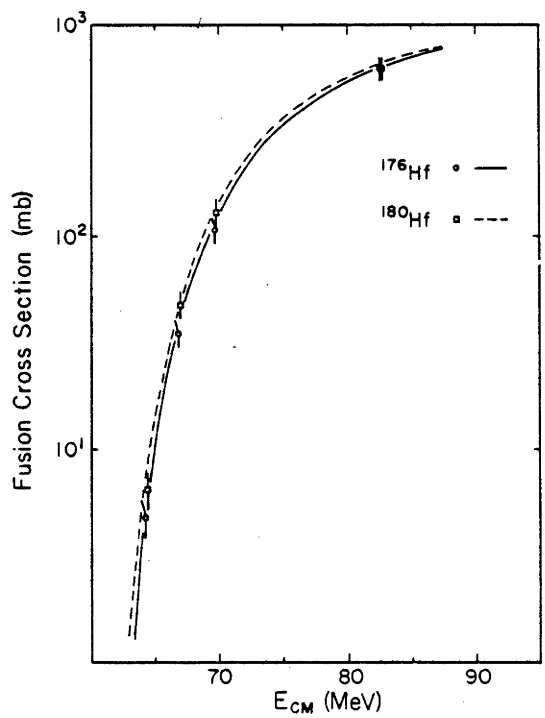

Fig. 5.20 Experimental fusion cross-sections for the reactions $^{176,180}Hf+^{16}O$. The solid and dashed lines show calculated cross-sections with the barrier penetration method. (expanation in text).

Again there is no significant difference in the fusion cross-sections between the isotopes at energies below the fusion barrier. The curves show fusion cross-section calculations with the barrier penetration method, allowing for barrier fluctuations, which are uniformly distributed [Vaz81]: The same potential and amount of barrier fluctuations were used for both systems. The difference between the calculated curves, which is in accordence with the data, is entirely due to the difference in nuclear radii.

The lack of differentiation in the observed sub-barrier fusion cross-sections for the tungsten and hafnium isotopes, suggests that either the hexadecapole moment plays a minor role in the sub-barrier fusion enhancement, or that the hexadecapole deformations are similar for different isotopes.

Table 5.10 Deformation parameters for the tungsten and hafnium isotopes, calculated with the Strutinsky renormalisation method [Got72].

Nucleus	β_2	β_4
^{182}W	0.24	-0.08
^{184}W	0.23	-0.09
^{186}W	0.23	-0.09
^{176}Hf	0.28	-0.04
^{180}Hf	0.25	-0.08

5.5 FISSION CROSS-SECTION CALCULATIONS

Fission cross-sections were calculated with the statistical model code Alert-1 of Blann and Komoto [Bla82]. This model describes the competition between fission and particle evaporation at various stages of the compound nucleus decay. The following parameters are of importance in the calculations :

1) The excitation energy. The excitation energy of the compound system, was taken relative to the liquid-drop ground-state of the compound nucleus using the prescription :

$$E^* = E_{c.m.} + E_p^{exp} + E_t^{exp} - M_{CN}^{LD} - 3\delta \qquad (5.5.1)$$

where $E_{c.m.}$ is the centre of mass energy, E_p^{exp} and E_t^{exp} are the experimental ground state masses of the projectile and target respectively, M_{CN}^{LD} is the liquid drop mass of the compound nucleus and δ is the pairing energy, taken as

$11/A_{CN}^{1/2}$. The last term was included to reproduce approximately the Yrast line of real nuclei at spins where their moments of inertia approach those of the liquid drop.

2) The compound nucleus angular momentum distribution.

3) The level density parameter a. This parameter, which is defined in chapter 2 eq. (2.8.13), is usually chosen between A/12.5 and A/7.5; where A is the nuclear mass number.

4) The ratio a_f/a_ν. This ratio of the level density at the saddle-point shape to the level density for the equilibrium shape is usually chosen close to unity.

5) The fission barrier. In the calculations rotating liquid drop model fission barrier with corrections for the finite range and the diffuseness of the nuclear potential were used (Sierk barriers).

6) Particle transmission coefficients and binding energies. Barrier penetration coefficients were obtained from global optical model potentials for neutrons, protons and alpha-particles. The binding energies were determined from the liquid-drop model.

Fission cross-sections were calculated for the compound nuclei ^{158}Dy, ^{168}Yb,^{178}W,^{182,188}Pt and ^{200}Pb with angular momentum distributions, discussed in the previous sections.

5.5.1 FISSION CROSS-SECTION DEPENDENCE ON THE COMPOUND NUCLEUS SPIN-DISTRIBUTION.

The same approach was followed as in [Cha86], where angular momentum dependent fission barriers of Sierk were used and values of a_ν and a_f/a_ν were fixed at A/10 and 1.00 respectively. In the calculations of [Cha86] the compound nucleus angular momentum distribution was parametrised with a Fermi-function. For each system the diffuseness parameter was constant and obtained from ZPM model calculations. The L_{max} parameter of the Fermi-function was adjusted for each energy to reproduce the fusion cross-sections, obtained from a least squares fit to the experimental data. In this way excellent agreement between calculated and experimental cross-sections was obtained for the heavier systems ^{178}W,^{188}Pt and ^{200}Pb as can be seen in fig. 5.21.

Here the freedom in parameters will be further restricted by directly using the partial fusion cross-section distributions, predicted by the ZPM fusion model without parametrisation. The results are shown in fig. 5.22.

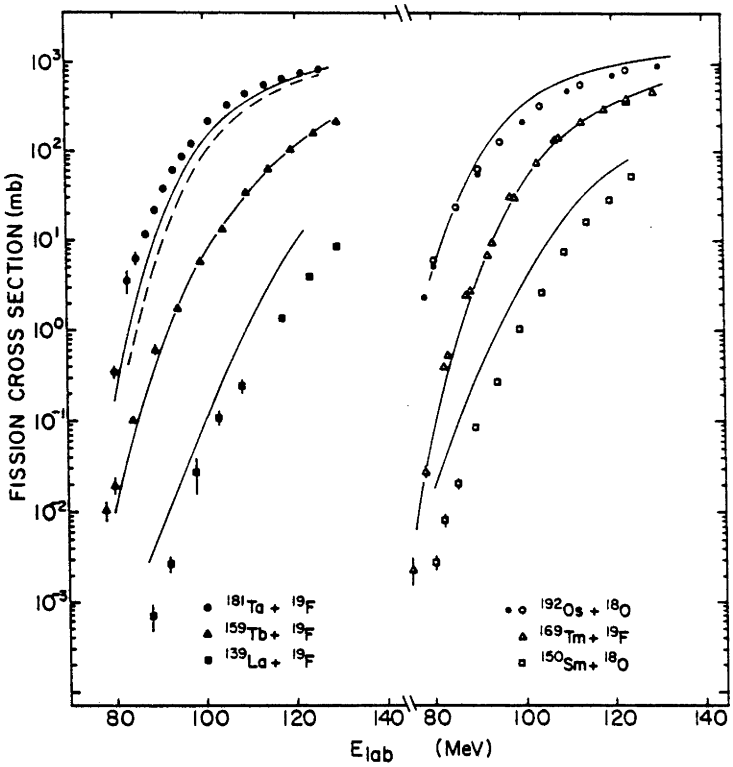

Fig. 5.21 Experimental fission cross-sections and results from statistical model calculations as explained in the text. The dashed line for the $^{181}Ta+^{19}F$ system is calculated with RLDM fission barriers. (from[Cha86]).

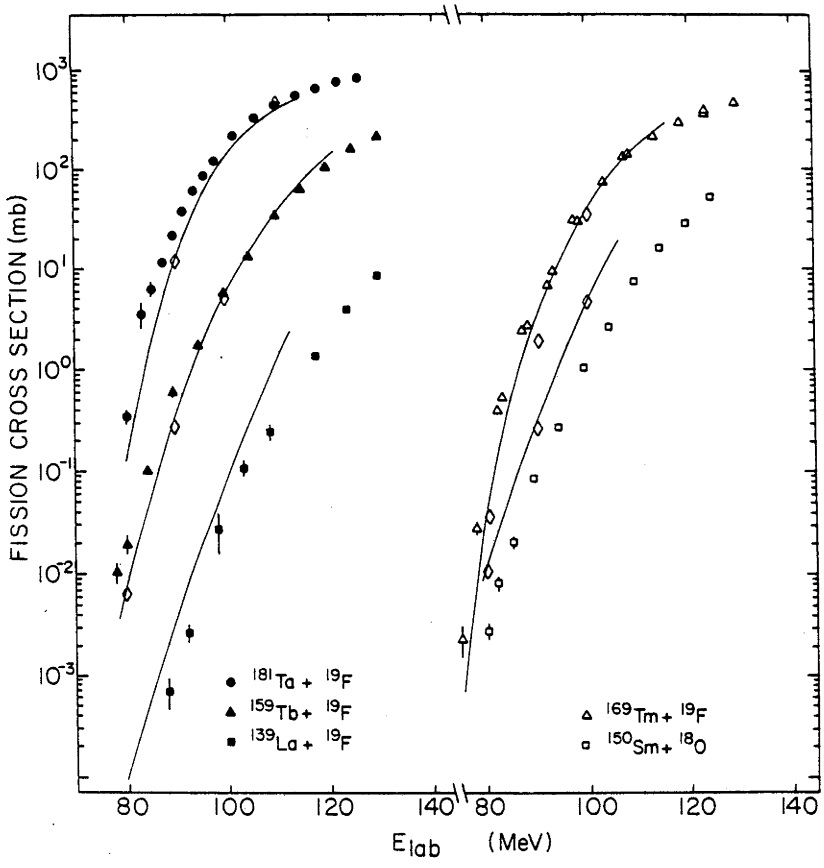

Fig. 5.22 Fission cross-section calculations with compound nucleus angular momentum distributions from the ZPM fusion model (solid lines) and the elastic fusion model (open diamonds).

Considering the fact that the calculations are essentially parameter free, the BE2,BE3 and deformations used in the ZPM model calculations were taken from the data tables, the agreement between experimental and calculated fission cross-section is reasonably good for the heavier systems. However, the results from using the Fermi-function parametrisation are better, which is most pronounced for the $^{159}Tb+^{19}F$ system. The discrepancies may be attributed to different fusion cross-sections used or to differences in shape of the ZPM distributions and its Fermi-function parametrisation. For the $^{159}Tb+^{19}F$ system the total fusion cross-sections from the ZPM model at lower energies were slightly higher than the cross-section from the least squares fit. Since the fission cross-sections calculated with the ZPM distributions are lower than those using the Fermi distributions despite the higher fusion cross-sections, the differences in fission cross-section must be due to angular momentum shape-effects. In fig. 5.14 and in [Cha86] it was noted that the Fermi-function parametrisation produces a longer tail than the ZPM-distribution. Since the fission-barrier height reduces with increasing angular momentum, the longer tail of the Fermi-function gives rise to higher fission cross-sections, especially at the lower energies. The fact that the differences in Fermi-function and ZPM anaysis are most pronounced in the $^{159}Tb+^{19}F$ system, which has the lowest fissility of the heavier systems, also indicates that the differences arise from angular momentum effects.

The excellent fits, obtained in [Cha86] for the heavier systems at lower energies are probably fortuitous.

In [Gil85] it has been shown that the compound nucleus angular momentum distribution becomes broader as the bombarding energy approaches the fusion barrier. This trend is also observed in the distributions from the ZPM model down to about 3 MeV above the fusion barrier (fig. 5.11), after which the distributions become narrower for energies below the barrier. Considering the underprediction of the fission cross-sections with these distributions, especially for energies below the fusion barrier, other effects than nuclear surface oscillations must be considered. Rhoades-Brown et al. pointed out that at energies near and below the barrier the fusion angular momentum distributions are significantly affected by the particle transfer processes (see fig. 2.12 chapter 2). The effect of fusion, proceeding through transfer channels, is not considered in the ZPM model, which may be the reason for the underpredicted fission cross-sections.

Direct reactions, including particle transfer processes, are taken into account in the elastic fusion model. Although it was not possible to reproduce the fusion excitation functions with a single value for parameter r_F with the optical model potentials from table 5.2, it is interesting to see how the different shapes of the spin-distribution

predicted by this model affect the calculated fission cross-sections.

For this purpose the fusion radius parameter r_F was adjusted at each energy to reproduce the fusion cross-section as obtained with the ZPM calculations. It should be noted that the shape of the spin-distribution is affected by changes in r_F. Fission cross-sections were calculated for energies for which optical model potentials were available. The results are shown in fig. 5.22 as open diamonds. The fission cross-sections are even more underpredicted than with the ZPM model distributions.

Because of the fact that the optical model potentials were derived from generalized elastic scattering data (with the exception of $^{150}Sm+^{18}O$), no strict conclusion can be made about which fusion model predicts the most appropriate angular momentum distribution. Furthermore, the differences between the spin-distributions are not significant enough to be able to choose between the models on the basis of calculated fission cross-sections alone.

For the systems $^{124}Sn+^{58}Ni$ and $^{118}Sn+^{64}Ni$ however, the predicted angular momentum distributions are vastly different as was shown in fig. 5.16. Fission cross-section calculations were performed for these systems with the angular momentum distributions from the sharp cut-off, ZPM and elastic fusion models. To make a comparison possible the distributions from the sharp cut-off and ZPM models were parametrised with the error-function defined in equation (4.3.12), and their fusion cross-sections made equal to the fusion cross-sections of the elastic fusion model as is explained in section 5.2. For the sharp cut-off distribution a value of $\Delta L << 1$ was used.

The fission cross-section calculations were performed with parameters $a_f/a_\nu = 1.00$ and $a_\nu = A/10$. No Sierk fission barriers were available for the ^{182}Pt nucleus. Instead the barriers were obtained by scaling the available barriers for ^{188}Pt as :

$$E_f(L) = E^{RFR}_{188}(L)\,\frac{E^{RLD}_{182}(L)}{E^{RLD}_{188}(L)} \qquad (5.5.2)$$

where RLD and RFR stand for rotating liquid drop model and rotating finite range model respectively.

The results of the calculations are shown in fig. 5.23. The upper curves (x10) are the fusion cross-section calculations with the elastic fusion model. The lower three curves are fission cross-sections calculated with elastic fusion (solid lines), ZPM (long dashed lines) and sharp cut-off (short dashed lines) distributions. Open circles and squares indicate experimental data from Argonne [Hen84] and the filled circles in panel (a) are the

fission cross-sections from chapter 4.

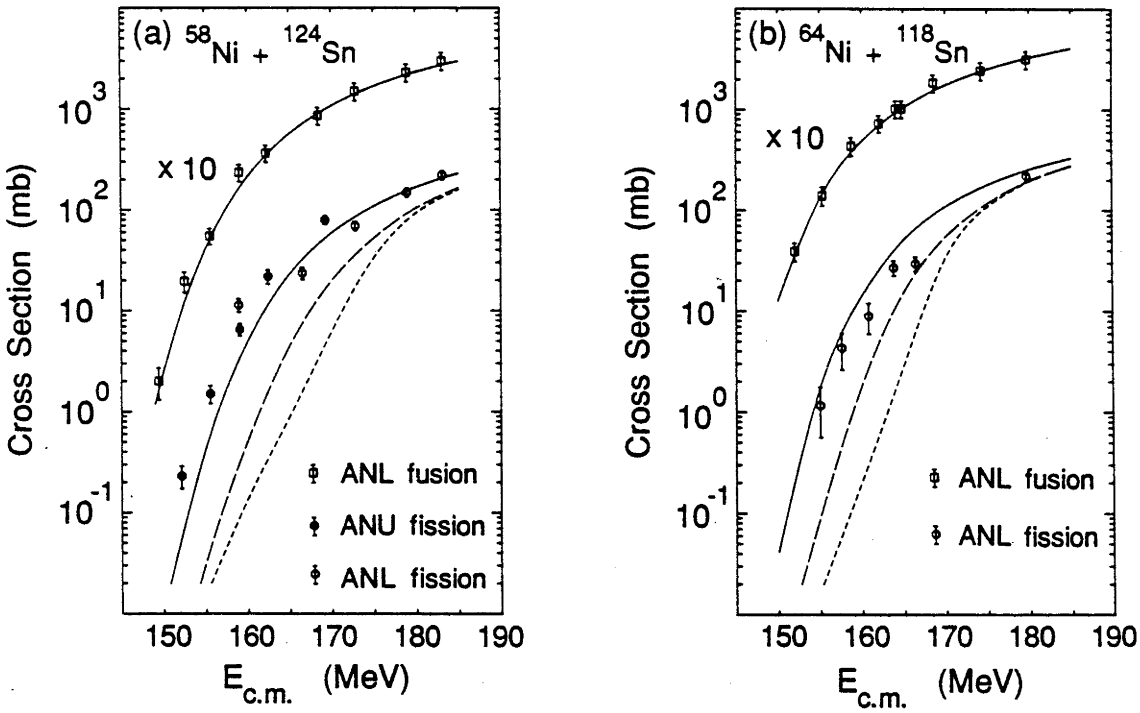

Fig 5.23 Fusion and fission cross-sections for the $^{124}Sn+^{58}Ni$ and $^{118}Sn+^{64}Ni$ systems. The fusion cross-sectons are multiplied by a factor of 10. The Argonne (ANL) fusion and fission data [Hen84] are denoted by the open squares and open circles, respectively. The ANU data are denoted by solid circles. The dotted, long-dashed and lower solid curves are ALERT1 predictions of fission cross-sections resulting from the CN angular momentum distributions of the sharp cut-off, ZPM and elastic fusion models,respectively.

For the $^{124}Sn+^{58}Ni$ system the elastic fusion predicts satisfactory fission cross-sections for the entire energy-range displayed. On the other hand, both the ZPM and sharp cut-off models considerably underestimate the experimental yields, especially at low energies.

For the $^{118}Sn+^{64}Ni$ system, the elastic fusion model gives the best agreement at the lower energies although the observed fission yields generally lie between the curves of the ZPM and elastic fusion models. The sharp cut-off model is unable to account for the data of either system.

The effect of uncertainties in the statistical model parameters was examined. The total fusion cross-section was varied by 20%, which is the quoted error of the data, and the level density parameters were varied over the ranges $A/11< a_\nu < A/7.5$ and $1.00< a_f/a_\nu <1.02$. The resultant changes in the fission cross-sections were not significant enough to alter the above conclusions.

5.6 DISCUSSION

The analysis of elastic scattering data with the optical model provides the partial reaction cross-section distribution. Because a substantial fraction of the reaction cross-section comes from direct reactions (see table 5.6), especially for energies near the Coulomb barrier) the shape of the partial reaction cross-section distribution may be different from the CN angular momentum distribution.

In fig. 5.7 it was shown that elastic scattering only probes the tail of the nuclear potentials and therefore does not provide information about the region of the nuclear potential where fusion is expected to take place. However, any surface oscillations or vibrations are also reflected in the tail of the potential, which should have its effect on the elastic scattering. Although the standard optical model uses a static spherical potential to describe elastic scattering it may account for surface effects in an average way by adjusting the diffuseness and radii of the real and absorptive potentials. The partial reaction cross-section for each L-wave is calculated from the overlap integral of the distorted wave-function and the absorptive nuclear potential. If the absorptive potential contains information about surface oscillations or deformations so will the partial reaction cross-section distribution.

In fig. 5.11 the diffuseness parameters δ from the optical model analysis and from the ZPM fusion model calculations were compared. For all systems the diffuseness of the partial reaction cross-section distribution increased as the bombarding energy approaches the fusion barrier. This is in agreement with the findings of Gil et al. [Gil85], who noted a similar increase in the average angular momentum of the CN angular momentum distribution, deduced from gamma-ray multiplicity measurements (fig. 2.18 chapter 2). To energies as low as 3.5 MeV below the fusion barrier their experimentally determined <L> could rather well be described by the Wong fusion model. (3.5 MeV. below the barrier is about -2.1 on the scale of fig. 5.11). Our calculations with the ZPM model, however, show a decrease in the diffuseness δ for energies below the fusion barrier. The sub-barrier penetration coefficients are very much dependent on the shape of the barrier.

In the Wong model, as described in chapter 2, the barrier penetration coefficients are calculated with the Hill-Wheeler parabolic barrier approximation, where the radius $R_b(L)$ and width ω_L at the barrier are substituted by $R_b(0)$ and ω_0 respectively. This is approximately valid for energies above the barrier. For sub-barrier energies, however, the barrier derived from a Woods-Saxon nuclear potential and a point-charge Coulomb potential is much wider than a parabola with the ω_L-value, calculated from the shape at

the top of the barrier and gets even wider for larger angular momenta due to the centrifugal potential.

In our ZPM model calculations the sub-barrier penetration coefficients were calculated with the WKB-approximation, which describes the quantum mechanical tunneling through the barrier between the classical turning points. This procedure accounts for the change in shape of the barrier with angular momentum, because for every L-value the barrier-height, position and the classical turning points are recalculated. The decrease in δ of the ZPM calculations for the lower energies in fig. 5.11 should therefore be more realistic than the calculated increase in <L> with the Wong model in [Gil85].

Nevertheless, the experimental data of gamma-ray multiplicity measurements and elastic scattering both show a definite increase in the diffuseness of the angular momentum distributions for energies near the fusion barrier. This, however, is more likely due to direct reaction effects. The fraction of the total reaction cross-section, due to direct reactions increases with decreasing energy as can be seen in table 5.6. The partial reaction cross-section distributions, deduced from elastic scattering, are therefore largly determined by the partial direct reaction cross-section distributions for energies below the barrier.

The increase in the measured <L> may be due to fusion processes proceeding through the direct reaction channels. At higher energies fusion may also take place via direct reactions but at these energies their contributions are small compared to the total fusion cross-section.

Figure 5.11 also shows that the δ-values, deduced from both the optical model analysis and the ZPM calculations are constant for energies well above the fusion barrier. For the systems with the larger deformations the ZPM model predicts a constant δ-value about 1 ($\hbar$) to 1.5 ($\hbar$) higher than the optical model method. The systems with the smallest deformations $^{150}Sm+^{18}O$ and $^{139}La+^{19}F$ show excellent agreement. Apparently the partial reaction cross-section distributions for these systems are well described with a the picture of a vibrating nucleus.

For all systems the diffuseness parameter δ is substantially different from zero. Also for energies well above the fusion barrier the distributions do not resemble a sharp cut-off form. More evidence for this statement comes from the gamma-ray multiplicity measurements for the system $^{159}Tb+^{19}F$. Statistical model calculations of compound nuclear decay with a sharp cut-off CN angular momentum distribution showed that the average angular momentum <L> and the width of the partial cross-section distribution of the lowest xn-channel disagree with the experimentally deduced values.

Decay with low neutron multiplicities originates from compound nuclei with high

angular momenta, for which the rotational energy is high and thus less energy is available for neutron emission. The fact that the sharp cut-off distribution underpredicts the experimental data of the lowest xn-channel and the ZPM-distribution gives results in agreement with them for energies way above the fusion barrier indicates that the CN angular momentum distribution must be diffuse. There is an uncertainty about the correctness of the shape of the Yrast-line, used in the calculations, but not enough to account for the large discrepancy between experimental results and calculated values when the sharp cut-off distribution is used.

The fission cross-sections calculated with statistical model code Alert-1, using CN angular momentum distributions from the ZPM model generally did not agree with the experimental values when the Sierk fission barriers and the parameter values $a_f/a_\nu=1.00$ and $a_\nu=A/10$ were used. In fig. 5.22 it can be observed that for the lightest systems $^{150}Sm+^{18}O$ and $^{139}La+^{19}F$ the experimental cross-sections are overestimated over the whole energy-range. For the heavier systems the agreement is better, but at the lower energies the calculations underestimate the experimental values and the slope of the calculated curve is steeper.

Let us first consider the heavier systems only and assume that the fission barriers and the parameter values for a_f/a_ν and a_ν, used in the calculations are correct. The ZPM model calculations reproduced the experimental fusion cross-sections well. This leaves the shape of the ZPM-distribution as the source of the observed disagreement. At high energies the fission cross-section is not very sensitive to the diffuseness of the CN L-distribution, because the fission probability is almost unity for high angular momenta. For the lower energies,however, the diffuseness does influence the fission cross-section.

The increasing difference between calculated and experimental fission cross-sections with decreasing energy is possibly due to the decrease in the diffuseness parameter δ (fig. 5.11), which starts at about 3 MeV above the fusion barrier. An increase in the δ-value with decreasing energy, as indicated by the optical model analysis of this work and the gamma-ray multiplicity measurements of Gil et al. may well account for the differences.

This increase in δ,as discussed earlier, is probably due to the influence of particle rearrangement reactions prior to fusion. However, the fission cross-sections calculated with the CN L-distributions from the elastic fusion model, which accounts for direct reactions, generally give the same results and in some cases underpredict the experimental values even more (fig. 5.22, open diamonds). It is however possible that this model does not describe the role of the direct reactions properly for these systems.

The above argument is based on the assumption that the parameter values, used in the fission calculations are correct. There may be some doubts about the validity of using the Sierk barriers, although they are the best calculated fission barriers presently available. Also there is uncertainty in the values of a_f/a_ν and a_ν. The a_f/a_ν parameter is somewhat restricted by the results of pre-fission neutron multiplicity measurements of Hinde et al. [Hin86]. Values of a_f/a_ν consistent with this data are in the range a_f/a_ν=0.99+0.02. The value of the level density parameter a_ν, however, is less restricted and is usually varied between $A/12.5 < a_\nu < A/7.5$. The experimental fission data for the heavier systems of fig. 5.22 cannot be reproduced with reasonable values of a_f/a_ν and a_ν if the ZPM or elastic fusion model L-distributions are used. Increasing a_f/a_ν affects the fission cross-sections for all energies, which would destroy the agreement at higher energies. An increase of a_ν from A/10 to A/12.5 increases the fission cross-sections for the ^{200}Pb,^{188}Pt and ^{178}W systems at 80 MeV by 15%,25% and 70%, respectively. However to fit the experimental data at this energy an enhancement of about 150% is needed for all three systems.The elastic fusion model did, however, reproduce the experimental fusion and fission cross-sections well for the system ^{124}Sn+^{58}Ni (fig. 5.23).

Recently there have been several publications on the measurement of CN L-distributions with "Crystal Balls" [Nol85],[Ruc86],[Fis86]. Nolan et al. measured gamma-ray multiplicity distributions for the reaction ^{80}Se+^{80}Se with the Tessa2 detector array [Twi83], which consists of fifty bismuth-germanate (BGO) detectors, subtending a solid angle of nearly 4π sr. They found rather high multiplicities even for energies below the fusion barrier. For a reduction in fusion cross-section with two orders of magnitude the average multiplicity only changed with a factor of two. The diffuseness of the CN L-distribution has to increase considerably to account for this.

Ruckelshausen et al. measured gamma-ray multiplicity distributions from the CN ^{156}Er with the Heidelberg-Darmstadt Crystal Ball [Met83], which consists of 162 NaI detectors. Figure 5.24 shows evaporation residue angular momentum distributions for ^{156}Er, formed in the reactions ^{92}Zr+^{64}Ni [(a) and (b)] and ^{144}Sm+^{12}C [(c) and (d)]. The arrows indicate the limiting angular momentum determined from the measured evaporation residue cross-sections within the sharp-cutoff approximation. One of the conclusions was, that in contrast to predictions from barrier fluctuation calculations, the

diffuseness of the CN L-distribution is small. However, there is considerable uncertainty about the conversion from multiplicity distribution to angular momentum distribution.

In contrast to this Vandenbosch et al. [Van86] found that for sub-barrier energies anomalously broad spin-distributions where required to explain the anisotropies in the fission-fragment angular distributions for several systems. These conflicting results show that the problem of determining the shape of the compound nucleus angular momentum distribution is still an open question.

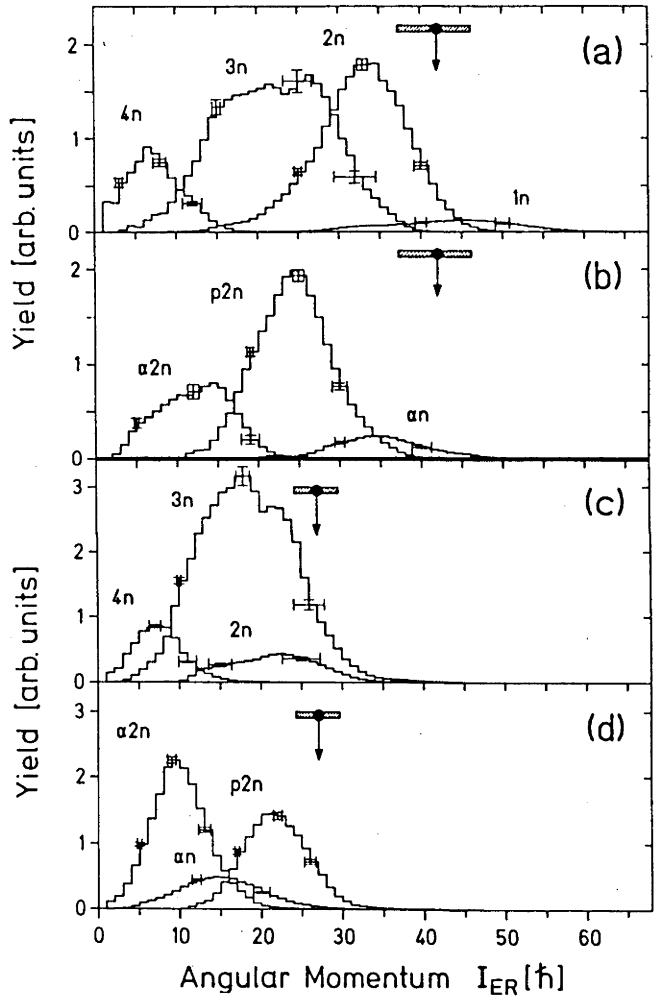

Fig.5.24. Evaporation-residue angular momentum distributions for ^{156}Er formed in (a),(b) ^{64}Ni+^{92}Zr and (c),(d) ^{12}C+^{144}Sm. The arrows indicate the limiting compound-nuclear angular momenta derived from measured evaporation-residue cross-sections assuming a sharp cut-off angular momentum distribution.

CONCLUSION

It has been shown that the reaction cross-section angular momentum distributions, deduced from elastic scattering data, are diffuse and that the diffuseness parameter δ from a Fermi-function parametrisation is constant for energies well above the fusion barrier. The constant value of δ is considerably different from zero for all systems studied. For energies near and below the fusion barrier the diffuseness increases dramatically.

The results from gamma-ray multiplicity measurements for the system $^{159}Tb+^{19}F$ also indicate that the diffuseness of the CN angular momentum distributions at energies well above the fusion barrier is considerably different from zero.

Fusion cross-sections calculated with the zero-point motion model, using experimental BEλ-values of the projectile and target-nucleus, reproduced the experimental fusion cross-sections for energies above and below the fusion barrier very well. Partial fusion cross-section distributions, calculated with this model, also show constant δ-values for energies well above the fusion barrier, which are nearly identical to the values from the reaction cross-section distributions for the lighter systems : $^{150}Sm+^{18}O$ and $^{139}La+^{19}F$, but are about 1.5 (ħ) higher for the systems ^{181}Ta, ^{169}Tm, $^{159}Tb+^{19}F$. For lower energies the diffuseness of the ZPM distributions increases but reaches a maximum near the fusion barrier and drops for sub-barrier energies.

The similarity in trend at the higher energies suggests that in this energy range the the diffuseness of the partial reaction cross-section distribution is mainly determined by nuclear surface effects. The continuing increase in the δ-value for decreasing energy, observed in the partial reaction cross-section distributions, which is in contrast with the ZPM predictions, is probably due to the contributions of particle transfer processes to the reaction cross-section.

Fission cross-section calculations for the systems ^{181}Ta, ^{169}Tm and $^{159}Tb+^{19}F$ with the ZPM model CN L-distributions did not reproduce the experimental data in detail. To get agreement between experimental and calculated fission cross-sections the diffuseness of the CN L-distribution has to increase for energies near and below the fusion barrier. The increase in diffuseness could come from the influence of particle transfer processes prior to fusion. Fission calculations with CN L-distributions from the elastic fusion model, which takes direct reaction effects on the fusion cross-section into account, did not improve the agreement between experiment and theory. It is possible that this model does not describe the direct reactions correctly. A coupled-channels

treatment, including couplings to particle transfer channels, would be more appropriate but is too complicated for the systems under study.

No substantial differences in sub-barrier fusion cross-sections were found for the different isotopes in the reactions $^{186,184,180}W+^{16}O$ and in the reactions $^{180,176}Hf+^{16}O$. The hexadecapole deformations, which are expected to effect the sub-barrier fusion cross-sections, are either essentially the same for the different isotopes or their effect on the fusion cross-section is washed-out by other processes.

REFERENCES

[Aus69] N. Austern, Direct Nuclear Reaction Theories, Wiley-Interscience John Wiley & Sons N.Y.

[Ajz83] F. Ajzenberg-Selove, *Nucl. Phys.* **A392** no 1 (1983) 105.

[Bas73] R. Bass , *Phys. Lett.* **47B** (1973) 139.

[Bas74] R. Bass , *Nucl. Phys.* **A231** (1974) 45.

[Bas77] R. Bass , *Phys. Rev. Lett.* **39** (1977) 265.

[Bec78] M. Beckerman and M. Blann, *Phys. Rev.* **C17** no 5 (1978) 1615.

[Bla57] J.S. Blair, *Phys. Rev.* **108** (1957) 827.

[Bla82] M. Blann and T. Komoto, University of California Radiation Laboratory Report UCID 19390, 1982.

[Blo67] R. Bloch, B.Elbek, P.O. Tjøm, *Nucl. Phys.* **A91** (1967) 576.

[Boc70] Nuclear Reactions Induced by Heavy Ions editors : R. Bock and W. Hering (North-Holland, Amsterdam 1970).

[Boh75] A. Bohr, B. Mottelson, Nuclear structure, vol. 2 (Benjamin, N.Y.1975).

[Bre77] A. Breskin and N. Zwang, *Nucl. instr. & Methods* **144** (1977) 609.

[Bro74] D.A. Bromley, *Nucl. inst. & Meth.* **122** (1974) 1.

[Bro76] R.A. Broglia , C.H. Dasso and A. Winther, *Phys. Lett.* **61B** (1976) 113.

[Bro83] R.A. Broglia , *Nucl. Phys.* **A409** (1983) 163c

[Bro85] Treatise on Heavy-ion Science, vol. 7, 304, ed. by D.A. Bromley Plenum Press N.Y.

[Bun49] O. Bunemann, T.E. Cranshaw and J.A. Harvey, *Can. J. Res.*, **A27** (1949) 191.

[But71] P.J.A. Buttle and L.J.B. Goldfarb, *Nucl. Phys.* **A176** (1971)299.

[Coh74] S. Cohen, F. Plasil and W.J. Swiatecki, *Ann. Phys.* **82** (1974) 557.

[Cra48] T.E. Cranshaw and J.A. Harvey, *J. Res.* , **A26** (1948) 243.

[Cha84] R.J. Charity, thesis (1984) Australian National University.

[Cha86] R.J. Charity, J.R. Leigh, J.J.M. Bokhorst, A. Chatterjee, G.S.Foote, D.J. Hinde, J.O. Newton, S. Ogaza & D. Ward, *Nucl. Phys.* **A459** (1986) 441.

[Chr73] P.R. Christensen, I. Chernov.,E.E. Gross, R. Stokstad and F.Videbaek, *Nucl. Phys.* **A207** (1973) 433.

REFERENCES

[Cof85] J.P. Coffin, P. Engelstein Treatise of Heavy-Ions Science, vol.7, ed. D. Allan Bromley Plenum Press N.Y.

[Das83a] C.H. Dasso, S. Landowne and A.Winther, *Nucl. Phys.* **A405** (1983) 381.

[Das83b] C.H. Dasso, S. Landowne and A. Winther, *Nucl. Phys.* **A407** (1983) 221.

[Das85] C.H. Dasso, S. Landowne and A. Winther, *Nucl. Phys.* **A432** (1985) 495.

[Das85] C.H. Dasso, J.D. Garrett and S. Landowne, *Phys. Lett.* **161B** no 1,2,3 (1985) 36.

[Dra78] G.D. Dracoulis, P.M. Walker and A. Johnston, *J. Phys. G : Nucl. Phys.* **vol 4,** no 5 (1978) 713.

[Dub71] Proceedings of the International Conference on Heavy Ion Physics, Dubna 1971.

[Ecc66] D. Eccleshall, M.J.L. Yates, J.J. Simpson, *Nucl. Phys.* **78** (1966) 481.

[Elb69] B. Elbek, Proceedings International Conference on properties of nuclear states. page 81, Les Presses de L'Universite de Montreal.

[End79] P.M. Endt, *Atomic Data and Nuclear Data Tables* **23** (1979) 3.

[End81] P.M. Endt, *Atomic Data and Nuclear Data Tables* **26** (1981) 47.

[Eng74] J.B.A. England, Techniques in Nuclear Structure Physics, vol.1 (Macmillan 1974).

[Esb81] H. Esbensen, *Nucl. Phys.* **A352** (1981)147.

[Esb83] H. Esbensen, Jian-Qun Wu and G.F. Bertsch, *Nucl. Phys.* **A411** (1983) 275.

[Fer70] B. Fernandez and J.Blair, *Phys. Rev.* , **C1**, no2 (1970) 523.

[Fis86] R.D. Fischer, A. Ruckelshausen, G. Koch, W. Kühn, V. Metag, R. Mühlhans, R. Novotny, H. Ströher, H. Gröger, D. Habs, H. W. Heyng, R. Repnow, D. Schwalm, W. Reisdorf and R.S. Simon, *Phys. Lett. B* vol. **171** no1 (1986) 33.

[Flo73] H. Flocard, P. Quentin and D. Vautherin, *Phys. Lett.* **46B** no 3 (1973) 304.

[Fra63] W.E. Frahn and R.H. Venter, *Ann. Phys.* (N.Y.) **24** (1963) 243.

[Fri72] A.M. Friedman, R.H. Siemssen and J.G. Cuninghame, *Phys. Rev.* **C6** no 6 (1972) 2219.

REFERENCES

[Gav80] A. Gavron, *Phys. Rev.* **C21** (1980) 230.

[Gil85] S. Gil, R. Vandenbosch, A.J. Lazarini, D. K. Lock and A. Ray, *Phys. Rev.* **C31** no 5 (1985) 1752.

[Gle75] N.K. Glendenning, *Review of Modern Physics* **vol 47** no 3 (1975) 659.

[Göt72] U. Götz, H. C. Pauli, K. Alder, K. Junker, *Nucl. Phys.* **A192** (1972) 1.

[Gro67] J.R. Grover and J. Gilat, *Phys. Rev.* **157** (1967) 802.

[Haa85] B. Haas, G. Duchene, F.A. Beck, T. Byrski, C. Gehringer, J.C. Merdinger, A. Nourredine, V. Rauch, J.P. Vivien, J. Barrette, S. Tobbeche, E. Bozek, J. Styczen, J. Keinonen, J. Dudek, W. Nazarewicz, *Phys. Rev. Lett.* **vol. 54**, no 5 (1985) 398.

[Hag75] G.B. Hagemann, R. Broda, B. Herskind,M. Ishimura, S. Ogaza and H. Ryde, *Nucl. Phys.* **A245** (1975) 166.

[Hem75] G. Hempel, F. Hopkins and G. Schatz, *Nucl. instr. & Methods* **131** (1975) 445.

[Hen84] W. Henning, Fusion Reactions Below the Coulomb Barrier, edited by S.G. Steadman, *Lecture Notes in Physics*, **vol. 219** (Springer-Verlag, Berlin,1984) p. 150.

[Her74] R.G. Herb, *Nucl. instr. & Methods* **122** (1974) 267.

[Hil53] D.L. Hill and J.A. Wheeler, *Phys. Rev.* **89** (1953) 1102.

[Hil79] D.L. Hillis, J.D. Garrett, O. Christensen, B. Fernandez, G.B. Hagemann, B. Herskind, B.B. Back and F. Folkmann, *Nucl. Phys.* **A325** (1979) 216.

[Hin82] D.J. Hinde, Thesis Australian National University 1982.

[Hin86] D.J. Hinde, R.J. Charity, G.S. Foote, J.R. Leigh, J.O. Newton, S. Ogaza and A. Chatterjee, *Nucl. Phys.* **A452** (1986) 550.

[Kra79] H.J. Krappe, J.R. Nix and A.J. Sierk, *Pys. Rev.* **C20** (1979) 992.

[Küh83] W. Kühn, P. Chowdhury, R.V.F. Janssens, T.L. Khoo, F. Haas, J. Kasagi and R.M. Ronningen, *Phys. Rev. Lett.* **vol 51**, no 20 (1983) 1858.

[Lan66] D.W. Lang, *Nucl. Phys.* **77** (1966) 545.

[Lan85] S. Landowne, Lecture notes in Physics 219, Fusion Reactions Below the Coulomb Barrier, Proceedings, Cambridge, MA 1985, Ed. by S.G. Steadman, Springer-Verlag Berlin.

[Lec59] K.J. Le Couteur and W.D. Lang, *Nucl. Phys.* **13** (1959) 32.

REFERENCES

[Lee75] I.Y. Lee, J.X. Saladin, J. Holden, J. O'Brien, C. Baktash, C. Bemis Jr., P.H. Stelson, F.K. McGowan, W.T. Milner, J.L.C. Ford Jr., R.L. Robinson and W Tuttle, *Phys. Rev.* **C12** no 5 (1975) 1483.

[Lei81] J.R. Leigh, D.J. Hinde and W. Galster, *Nucl. Instr. & Meths.* **186** (1981) 541.

[Ley72] J.R. Legg Thesis, Yale University (1972).

[Lob70] K.E.G. Lobner, M. Vetter and V. Honig, *Nuclear data tables* **A7** (1970) 495.

[McG81] F.K. McGowan, W.T. Milner, *Phys. Rev.* **C23** (1981) 1926.

[McI60] J.A. McIntyre, K.H. Wang and L.G. Becker, *Phys. Rev.* **117** (1960) 1337.

[Mes70] A. Messiah, Quantum Mechanics vol. 1, North Holland Publishing Company Amsterdam.

[Met83] V. Metag et al. Lecture Notes in Physics, vol 178 (Springer, Berlin) (1983)163.

[Mot49] N.F. Mott, H.S.W. Massey : The Theory of Atomic Collisions, 2nd ed. chap. 2 and 3 Oxford : Clarendon Press 1949.

[Mur86] T. Murakami, R. Vandenbosch, C.C. Sahm, D.D. Leach, A. Ray and M.J. Murphy, to be published in *Phys. Rev. C.*

[Mus82] M.G. Mustafa, P.A. Baisden and H. Chandra, *Phys. Rev.* **C25** (1982) 2524.

[Mye67] W.D. Myers, Lawrence Berkeley Laboratory Report LBL-3428 (1974).

[Mye74] W.D. Myers and W.J. Swiatecki, *Arkiv. Fysik* **36** (1967) 343.

[Nol85] P.J. Nolan, D.J.G. Love, A. Kirwan, D.J. Unwin, A.H. Nelson, P.J. Twin, J.D. Garrett, Phys. *Rev. Lett.* vol. **54**, no 20 (1985) 2211.

[Oeh74] R.N. Oehlberg, L.L. Riedinger, A.E. Rainis, A.G. Schmidt, E. Funk, J.W. Mihelich, *Nucl. Phys.* **A219** (1974) 543.

[Oes79] H.J. Oeschler, H.J. Harney, D.L. Hillis and K.S. Sim, *Nucl. Phys.* **A325** (1979) 463.

[Oph74a] T.R. Ophel, J.S. Harrison, J.O. Newton, R.H. Spear, E.W. Titterton and D.C. Weisser, *Nucl. Insrt. & Meth.* **122** (1974) 227.

[Oph74b] T.R. Ophel, Vacuum Notes 1 & 2, ANU internal report ANU-P/597.

[Oph78] T.R. Ophel and A. Johnston, *Nucl. Instr. & Meth.* **157** (1978) 461.

[Oph82] T.R. Ophel, W.Galster, D.J. Hinde and J.R. Leigh, *Nucl. Instr.*

REFERENCES

&Meth. **193** (1982) 507.

[Pen83] R. Pengo, D. Everrs, K.E.G. Löbner, U. Quade, K. Rudolph, S.J. Skorka and I. Weidl, *Nucl. Phys.* **A411** (1983) 255.

[Pie85] S.C. Pieper, M.J. Rhoades-Brown and S. Landowne, *Phys. Lett.* **B162** (1985) 43.

[Ray72] J. Raynal, Computing as a language of physics (IAEA, Vienna 1972).

[Rhe75] K.E. Rehm, H.J. Korner, M. Richter, H.P. Rother, J.P. Schiffer and H. Spieler, *Phys. Rev.*, **C12**, no 6 (1975) 1945.

[Rho80] M. J. Rhoades-Brown, M. J. Macfarlane and S. C. Pieper, *Phys. Rev.* **C21** (1980)2417; *Phys. Rev.* **C21** (1980) 2436.

[Rho83] M.J. Rhoades-Brown and V.E. Oberacker, *Phys. Rev. Lett.* **vol. 50** no 19 (1983) 1435.

[Rho84a] M.J. Rhoades-Brown and M.Prakash, *Phys. Rev. Lett.* **53** (1984) 333.

[Rho84b] Private communications.

[Ric74] P. Rice-Evans, Spark Streamer, Proportional and Drift Chamber, Richelieu Press, London (1974).

[Rob83] Private communications.

[Ron78] R.M. Ronningen, T.H. Kruse, R. Suchannek, W. Savin and J.H. Hamilton, *Phys. Rev.Lett.* **40** no 6 (1978) 364.

[Ruc86] A. Ruckelshausen, R.D. Fischer, W. Kühn, V. Metag, R. Muhlhans, R. Novotny, T. L. Khoo, R.V.F. Janssens, H. Gröger, D. Habs, H. W. Heyng, R. Repnow, D. Schwalm, G. Duchène, R. M. Freeman, B. Haas, F. Haas, S. Hlavac and R.S. Simon, *Phys. Rev. Lett.* **vol. 56,** no 22 (1986) 2356.

[Sat83] G.R. Satchler, Direct Nuclear Reactions, Clarendon Press, Oxford University press 1983 N.Y.

[Seg77] Experimental Nuclear Physics, vol. 1, p.21, ed. E. Segre, John Wiley & Sons, Inc.

[Sob86] L.G. Sobotka, D.G. Sarantites, H. Puchta, F.A. Dilmanian, M. Jääskeläinen, M.L.Halbert, J.H. Barker, J.R. Beene, R.L. Ferguson, D. C. Hensley and G.R. Young, *Phys. Rev.* C34 no3 (1986) 917.

[Spr65] A. Springer and B.G. Harvey, *Phys. Lett.* **14** (1965) 116.

[Sta53] H.H. Staub, Experimental Nuclear Physics vol.1, editor E. Segre, John Wiley & Sons, Inc. New York, London.

REFERENCES

[Ste72] F.S. Stephens and R.S. Simon, *Nucl. Phys.* **A183** (1972) 257.

[Ste76] H. Stelzer, *Nucl. instr. & Methods* **133** (1976) 409.

[Sto81] R.G. Stokstad and E.E. Gross, *Phys. Rev.* **C23**, no 1 (1981) 281.

[Twi83] P.J. Twin, P.J. Nolan, R. Aryaeinejad, D.J.G. Love, A.H. Nelson, A. Kirwan, *Nucl. Phys.* **A409** (1983) 343c.

[Uda85] T. Udagawa, B.T. Kim and T. Tamura, *Phys. Rev.* **C32** (1985)124.

[Van83] R. Vandenbosch, B.B. Back, S. Gil, A. Lazzarini and A. Ray, *Phys. Rev.* **C28** no 3 (1983) 1161.

[Van86] R. Vandenbosch, T. Murakami, C.C. Sahm, D.D. Leach, A. Ray and M.J. Murphy, *Phys. Rev. Lett.* (1986) 1234.

[Vaz81] L.C. Vaz and J.M. Alexander, *Phys. Rep.* **69** no5 (1981) 373.

[Vej68] E. Veje, B. Elbek, B. Herskind and M.C. Olesen, *Nucl. Phys.* **A109** (1968) 489.

[Vio85] V.E. Viola, K. Kwiatkowski and M. Walker, *Phys. Rev.* **C31**, no 4 (1985)1550.

[Vul86] E. Vulgaris, L. Grodzins, S.G. Steadman, and R.Ledoux, *Phys. Rev.* **C33** no 6 (1986) 2017.

[Wal76] P.M. Walker, G.D. Dracoulis, A. Johnston, J.R. Leigh, M.G. Slowcombe, I.F. Wright, *J. Phys. G* : **Nucl. Phys. 2** (1976) L 197.

[Wer78] S.Y. v. d. Werf, *Nucl. Instr.& Meth.* **153** (1978) 221.

[Win65] A. Winther and J. de Boer, California Institute of Technology Technical Report, 18/11 (1965).

[Won73] C.Y. Wong, *Phys. Rev. Lett.* **31** (1973) 265.

[Zeb74] A.M. Zebelman, L. Kowalski, J. Miller, K. Beg, Y. Eyal, G. Jaffe, A. Kandil and D. Logan, *Phys. Rev.* **C10** (1974) 200.

[Zuc60] A. Zucker, Ann. Rev. Nucl. Sci. no 10 (1960) 27.